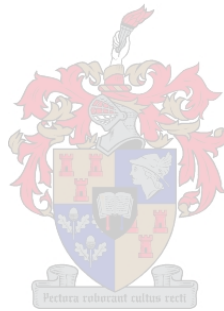


**MODELLING THE THERMAL, ELECTRICAL AND FLOW
PROFILES IN A 6-IN-LINE MATTE MELTING FURNACE.**

by

CORNELIUS ALBERT SNYDERS

Thesis submitted in partial fulfillment
of the requirements for the Degree
of



MASTER OF SCIENCE IN ENGINEERING
(MINERAL PROCESSING)

in the Department of Process Engineering
at Stellenbosch University

Supervised by
Prof Jacques Eksteen
Prof Steven Bradshaw

December 2008

DECLARATION

By submitting this thesis electronically, I declare that the entirety of the work contained therein is my own, original work, that I am the owner of the copyright thereof (unless to the extent explicitly otherwise stated) and that I have not previously in its entirety or in part submitted it for obtaining any qualification.

Date: December 2008

ABSTRACT

The furnace at Polokwane is designed to treat high chromium containing concentrates which requires higher smelting temperatures to prevent or limit the undesirable precipitation of chromium spinels. The furnace has therefore been designed to allow for deep electrode immersion with copper coolers around the furnace to permit the operation with the resulting higher heat fluxes.

Deep electrode immersion has been noted to result in dangerously high matte temperatures. Matte temperatures however can be influenced by a number of furnace factors which emphasize the need to understand the energy distribution inside the furnace. Computational fluid dynamics (CFD) has therefore been identified to analyze the flow and heat profiles inside the furnace. The commercial CFD software code Fluent is used for the simulations.

Attention has been given only to a slice of the six-in-line submerged arc furnace containing two electrodes or one pair while focusing on the current density profiles, slag and matte flow profiles and temperature distribution throughout the bath to ensure the model reflects reality. Boundary conditions were chosen and calculated from actual plant data and material specifications were derived from previous studies on slag and matte.

Three dimensional results for the current, voltage and energy distributions have been developed. These results compare very well with the profiles developed by Sheng, Irons and Tisdale in their CFD modelling of a six-in-line furnace. It was found the current flow mainly takes place through the matte, even with an electrode depth of only 20% immersion in the slag, but the voltage drop and energy distribution still only take place in the slag.

Temperature profiles through-out the entire modelling domain were established. The vertical temperature profile similar to Sheng *et al.* 1998b was obtained which shows a specifically good comparison to the measured temperature data from the Falconbridge operated six-in-line furnace. The temperature in the matte and the slag was found to be uniform, especially in the vertical direction.

It has been found that similar results with Sheng *et al.* (1998b) are obtained for the slag and matte velocity vectors. Different results are, however, obtained with different boundary conditions for the slag/matte interface and matte region; these results are still under investigation to obtain an explanation for this behaviour.

The impact of the bubble formation on the slag flow was investigated and found to be a significant contributor to the flow. With the bubble formation, it is shown that possible

'dead zones' in the flow with a distinctive V-shape can develop at the sidewalls of the furnace with the V pointing towards the centre of the electrode. This behaviour can have a significant impact on the point of feed to the furnace and indirectly affect the feed rate as well as the settling of the slag and matte. These results are not validated though.

Different electrode immersions were modelled with a constant electrical current input to the different models and it was found that the electrode immersion depth greatly affects the stirring of the slag in the immediate vicinity of the electrode, but temperature (which determines the natural buoyancy) has a bigger influence on the stirring of the slag towards the middle and sidewall of the slag bath.

The sensitivity of the model to a different electrode tip shape with current flow concentrated at the tip of the electrode was also modelled and it was found that the electrode shape and electrical current boundary conditions are very important factors which greatly affect the voltage, current density and temperature profiles through the matte and the slag. A detailed investigation to determine the electrode tip shape at different immersions, as well as the boundary conditions of the current density on the tip of the electrode is necessary as it was proven that the model is quite sensitive to these conditions.

Several recommendations arose from this modelling work carried out in this investigation. Time constraints, however, did not allow for the additional work to be carried out and although valuable results were obtained, it is deemed to be a necessity if a more in-depth understanding of furnace behaviour is to be obtained. Future work will include the validation of the results, understanding the liquid matte model, investigating the MHD effects and modelling different furnace operating conditions.

ABSTRAK

Die smelter by Polokwane is ontwerp om hoër temperature in die bad toe te laat om konsentrate met n hoë chroom inhoud te kan smelt. Hoër temperature sal die presipiasie van chroom spinelle in die oond beperk. Die elektrodes moet dus dieper in die slak kan penetreer en koper koelers is rondom die oond geïnstalleer om die hoër hitte las weg te gelei.

Gevaarlike hoë bad temperature word egter waargeneem saam met dieper elektrode penetrasie maar hierdie hoë temperature kan ook die resultaat wees van verskeie ander faktore. Dit beklemtoon die behoefte om die energie verspreiding in die oond beter te kan verstaan. Numeriese vloeidinamika [E: "Computational Fluid Dynamics" of CFD] is dus geïdentifiseer om die vloei en hitte profiele in die oond te analiseer. Die kommersieel beskikbare pakket 'Fluent' is gebruik.

Aandag is slegs aan n seksie van die 6-in-lyn boog oond gegee en bevat twee elektrode helftes. Daar is gefokus op die stroomdigthede, vloei profiele en die temperatuur verspreiding deur die bad sodat dit n goeie weerspieeling is van die realiteit. Grens kondisies is gekies en bereken vanaf aanleg data en materiaal spesifikasies is saamgestel vanaf vorige studies wat op mat en slak gedoen is.

Drie dimensionele resultate vir die stroom en energie verspreiding is ontwikkel. Hierdie resultaat vergelyk goed met die profiele wat bereken is deur Sheng, Irons en Tisdale in n soortgelyke CFD model van n 6-in-lyn oond. Dit is bevind dat die stroomvloei hoofsaaklik deur die mat fase plaasvind, selfs met vlak elektrode dieptes (20%) maar dat die hitte nogsteeds in die slak genereer word.

Temperatuur profiele deur die model is bereken. Die vertikale temperatuur profiel is soortgelyk aan die van Sheng *et al.* (1998b) en vergelyk goed met gemete data van die Falconbridge 6-in-lyn oond. Die temperatuur deur die slak en mat onderskeidelik is hoofsaaklik uniform.

Resultate vir die snelheids vektore in die mat en slak stem ooreen met die van Sheng *et al.* (1998b). Verskillende resultate word egter verkry as die grens toestande tussen die mat en slak verander word. Geen verklaring hiervoor is egter nog gevind nie en moet dus nog verder bereken word.

Die impak van borrels wat vorm rondom die elektrodes is ondersoek en dit is gevind dat dit n belangrike rol speel in die berekening van die snelheids vektore. Dit is gewys dat saam met die borrels, moontlike 'dooie zones' kan ontstaan wat die voer van

konsentraat na die oond kan beïnvloed asook op 'n indirekte wyse, die skeiding van die slak en mat. Hierdie resultate is egter nie gevalideer nie.

Verskillende elektrode dieptes is gemodelleer met konstante stroom na elkeen van die modelle. Dit is gevind dat die elektrode diepte, grootliks die roering in die area rondom die elektrodes beïnvloed maar dat die temperatuur 'n groter invloed het op die roering of snelheids vektore naby die middel en kant van die oond in die slak fase.

Die sensitiwiteit van die model t.o.v die vorm van die elektrode punt met die stroom vloei meer gekonsentreerd op die punt is getoets en gevind dat hierdie faktore baie belangrik is. 'n Volledige ondersoek om die ware elektrodepunt vorm by verskillende dieptes vas te stel asook die grens toestande van die stroomdigtheid op die punt word aan beveel.

Verskeie aanbevelings word gemaak vir verdere studie. Hierdie werk is noodsaaklik as die smelter kondisies beter verstaan wil word. Toekomstige werk moet die validasie, vloeibare mat model, 'MHD' effekte en verskillende oond omstandighede insluit, maar val buite die bestek van hierdie MSc verhandeling.

ACKNOWLEDGEMENTS

My thanks go to:

Anglo Platinum and specifically Polokwane Smelter for providing the support that enabled me to carry out this work. I am privileged to have been able to carry out this work in three different countries; Australia, Netherland and of course South Africa. Specifically, I would like to thank Roger Leighton, Dr Neville Plint and Bertus De Villiers for their support of the project. I would also like to thank Michelle Hempel for making all my travel arrangements. To Paul van Manen at Polokwane Smelter to allow as much time as possible for this research while already short staffed at the Smelter.

Prof Jacques Eksteen for his excellent supervision of the project as well as his mentoring, motivation and guidance on all related aspects of this project. Through Prof Eksteen, this project has been a valuable learning experience.

I would like to thank Danie de Kok, Qfinsoft South Africa, distributors of Fluent, for their support and fast responses to all my Fluent queries.

CSIRO minerals and specifically Dr Phil Schwarz for hosting me in Melbourne Australia and his guidance of the project while still in an early development phase.

The staff of the Materials Science and Engineering department at T.U Delft University of Technology in the Netherlands. My thanks go to Dr. Yongxiang Yang who taught me a great deal about CFD work and how to approach these types of projects and through his guidance the model really took shape. To Emile Scheepers, Allert Adema and Christa Meskers for their friendship and giving me a good taste of the European lifestyle.

To God, through whom everything is possible

CONTENTS

DECLARATION	ii
ABSTRACT	iii
ABSTRAK	v
ACKNOWLEDGEMENTS	vii
CONTENTS	viii
LIST OF FIGURES	xi
NOMENCLATURE	xvii
INTRODUCTION	1
1.1 Background	1
1.2 Plant description.....	3
1.3 Project Objectives.....	3
1.3.1 MSc Objectives	4
LITERATURE REVIEW	6
2.1 Electrical furnaces	6
2.1.1 Characterization of smelting furnaces	7
2.1.2 Immersed electrode operation	8
2.1.3. Bath Stirring	11
2.1.3.1 Natural convection in the slag.....	11
2.1.3.2 Bubble stirring.....	11
2.1.3.3 Magnetohydrodynamics (MHD) as stirring force	11
2.2 Magnetohydrodynamics (MHD)	12
2.2.1 The Governing equations of electrodynamics.....	12
2.2.1.1 The electrical field and the Lorentz force.....	12
2.2.1.2 Ohms Law and the volumetric Lorentz force	13
2.2.1.3 Ampere’s law.....	14
2.2.2 Maxwell’s equations	14
2.3 Material Properties.....	15
2.3.1 Slag Viscosity	15
2.3.2 Slag density	16
2.3.3 Slag electrical conductivity	17
2.3.4 Viscous heating	18
2.3.5 Magnetic Permeability.....	19
2.3.6 Interfacial Tension and surface tension	19
2.4 CFD	21
2.4.1 CFD codes	22
2.4.2 CFD principles and governing equations	22
2.4.2.1 Continuity Equation	23
2.4.2.2 Momentum conservation	24
2.4.2.3 Thermal energy conservation or enthalpy equation	24
2.4.3 Defining properties.....	25
2.4.3.1 Piecewise-linear functions.....	25
2.4.3.2 The Boussinesq model	26
2.4.4 Magnetic Hydrodynamics Model (MHD)	26
2.4.5 Multiphase modelling.....	27

2.4.5.1 The Volume of fluid method (VOF)	28
2.4.5.2 Mixture Model	29
2.4.6 Discrete phase modelling	31
2.4.7 Boundary Conditions	32
2.4.7.1 Walls	32
2.4.7.2 Symmetry planes	34
2.4.7.3 Moving solid zones	34
2.4.8 Numerical Solution	34
2.4.8.1 Computational Grid (Mesh)	34
2.4.8.2 Discretization of the governing transport equations	35
2.4.8.3 Solvers	37
2.4.8.4 Under relaxation	37
2.5 Previous CFD models of a six-in-line furnace	38
2.5.1 Sheng, Irons and Tisdale 1998	38
2.5.1.1 Assumptions and formulation	38
2.5.1.2 Model results	41
2.5.2 CSIR model of the Polokwane furnace	44
2.6 Literature review summary	47
MODEL SET-UP	48
3.1 Creating the solution domain	48
3.1.1 The furnace slice	48
3.1.2 Model zones	51
3.1.2.1 Level Measurements	52
3.1.3 Meshing the computational domain	52
3.1.3.1 Creating the grid	52
3.1.3.2 Mesh quality	54
3.2 Model set-up and approach	55
3.2.1 Energy Generation	55
3.2.2 Energy sinks	57
3.2.2.1 Concentrate heat-up and melting	58
3.2.2.2 Slag and matte heat-up	61
3.2.2.3 Shell losses	62
3.2.2.4 Reactions around the electrode	63
RESULTS AND DISCUSSION OF RESULTS	65
4.1 Electrode current	65
4.2 Electrode potential and Power Distribution	68
4.3 Temperature distributions	70
4.4 Energy balance	73
4.5 Slag/matte interface	74
4.6 Flow profiles	76
4.6.1 Solid matte model	76
4.6.1.1 With gas circulation	76
4.6.1.2 Without gas circulation	78
4.6.2 Liquid matte model	79
4.6.3 Multiphase modelling	81
4.7 Surface heat fluxes	82
4.8 Computational efficiency	85
4.8.1 Grid Independence	85
4.8.2 Convergence	85
4.8.3 CPU time	87
4.9 Modelling at different immersion depths	87
4.9.1 Constant Current	88
4.9.2 Electrode tip shape and current distribution at the tip	93

CONCLUSION	98
5.1 Model conclusion	98
5.2 Conclusion on MSc Objectives.....	100
RECOMMENDATIONS	102
PAPERS WRITTEN	104
REFERENCES	105
APPENDIX.....	109
Material Properties	109
Furnace refractories	109
Copper properties	112
Carbon monoxide properties.....	112
Concentrate	113
Slag	113
Matte	115
User defined code	116

LIST OF FIGURES

Figure 2.1: a) Immersed electrode operation. b) Open arc operation. c) Submerged arc operation. d) Shielded arc operation	8
Figure 2.2: Load Resistance versus the electrode tip position. Ma <i>et al.</i>	9
Figure 2.3: Current flow in a electric matte furnace. The slag level and electrode immersion affect the current profile as shown in a and b.....	10
Figure 2.4: The surface tension of the ternary eutectic melt (.38% CaO, 20% Al ₂ O ₃ , 42% SiO ₂). A – Vaisburd results, B – Elliot’s results, X – Slag Atlas 95 results.....	21
Figure 2.5: Mass flows into and out of the fluid element for developing the continuity equation.....	23
Figure 2.6: Depicting discretization of scalar transport properties by the finite volume method.....	35
Figure 2.7: The electrical potential as calculated by Sheng <i>et al.</i> 1998b	41
Figure 2.8: The volumetric heat release as calculated by Sheng <i>et al.</i> 1998b	42
Figure 2.9: Temperature profile in the matte and slag as calculated by Sheng <i>et al.</i> 1998b	42
Figure 2.10: Comparison by Sheng <i>et al.</i> 1998b between measured and calculated data showing good comparison in the slag but a more uniform temperature in the matte.	43
Figure 2.11: Slag velocity vectors as calculated by Sheng <i>et al.</i> 1998b	43
Figure 2.12: Computed velocity vectors in a circular furnace by Jardy <i>et al.</i> (as referenced by Sheng et al 1998b.....	44
Figure 3.1: The complete furnace showing the 6 electrodes, off gas ports, hearth, sidewall, end walls, roof, matte tapping holes, matte, slag and concentrate layers. (CAD model by the CSIR).....	49
Figure 3.2: A quarter of an electrode starching towards the middle point between electrodes and the furnace sidewall.	49
Figure 3.3: The furnace slice to be modelled containing only the concentrate, slag and matte layers, the furnace hearth and a section of the sidewall.	50
Figure 3.4: The furnace slice with the electrode pair to be used as computational domain. The yellow lines indicate symmetry boundaries.....	50

Figure 3.5: The shape of the electrode tips indicated shallow immersion depths corresponding to the shape of the electrode tips in the model.....	51
Figure 3.6: The different furnace regions/zones assigned with a specific material and modelled as either a liquid or a solid zone.....	52
Figure 3.8: Pave meshing scheme coopered downwards	53
Figure 3.9: T-grid mesh in the bottom right corner coopered along the length of the slice and a course mesh in the matte area where the temperature is more uniform with fine mesh between the slag and the matte.	53
Figure 3.10: Model mesh showing a fine grid at the concentrate/slag interface where steep temperature gradients occur.	54
Figure 3.11: Mesh quality distribution showing that 85% of the meshed elements to be in the excellent region indicating a very high quality mesh.	55
Figure 3.12: Results for energy input: a) Electrode tip voltage and b) the joule heating generated in the bath.	57
Figure 3.13: Factsage heat-up and melting profile of concentrate. By dividing the curve in constant gradients, effective Cp_conc values can be calculated.	59
Figure 3.14: Effective Cp_conc values calculated from the gradients of the enthalpy vs temperature curve. The higher Cp values compensate for energy required for melting reactions	60
Figure 3.15: The heat-sink in the concentrate compensating for the energy due to the heat-up and melting of concentrate. Melting mainly occurring at the slag/concentrate interface	61
Figure 3.16: Energy sink due to the heat-up of slag and matte from melting temperature to bath/operating temperature. The energy sink is assumed to be uniform over the slag area.	62
Figure 3.17: CO bubbles being released at the electrode surface causing a stirring effect in the slag.	64
Figure 4.1: a. Three dimensional view of the current density profiles through the furnace slice indicating the majority of the current flowing through the matte layer and b) the current density vectors depicting the direction of the largest current density vectors to be vertical in the slag in horizontal or through the matte.	66
Figure 4.2: Two dimensional current density profiles through certain plains of the furnace slice. A – Cut through the centre of both electrodes along the length of the furnace. B - Cut through the middle of one electrode towards the sidewalls	

showing the arc of the hearth. C – Cut through the slag parallel to the slag/concentrate interface at the bottom the electrode tip. D – Cut just below the matte/slag interface parallel to the interface.	67
Figure 4.3: A three dimensional view as well as the two dimensional voltage profiles through certain plains of the furnace slice. A – Cut through the centre of both electrodes along the length of the furnace. B - Cut through the middle of one electrode towards the sidewalls showing the arc of the hearth. C – Cut through the slag parallel to the slag/concentrate interface at the bottom the electrode tip.	68
Figure 4.4: A three dimensional view as well as the two dimensional voltage profiles through certain plains of the furnace slice. A – Cut through the centre of both electrodes along the length of the furnace. B - Cut through the middle of one electrode towards the sidewalls showing the arc of the hearth. C – Cut through the slag parallel to the slag/concentrate interface at the bottom the electrode tip.	69
Figure 4.5: Temperature profiles a) The entire model domain b) Concentrate c) Slag d) Matte	70
Figure 4.6: The vertical temperature bath profile through the concentrate, matte and slag. The red line in the bottom left corner indicates where the temperature profile was taken.	71
Figure 4.7: Histogram of the temperature in the matte showing a very narrow Rayleigh distribution around 1656 K. The temperatures on the boundaries are not included.	72
Figure 4.8: Histogram of the temperature in the slag indicating a small amount of cells with temperatures from 1600K to 1750K with the majority of cells falling in the range between 1785K and 1825K. The temperatures on the boundaries are not included.	72
Figure 4.9: Pie charts to show the distribution of energy in the model. a) 99.4% of the energy is generated through joule heating in the slag. b) 67% of the energy is used for concentrate melting.	73
Figure 4.10: The electrode potential calculated with the mode (a) compared to the furnace measured value (b). The difference account for the arcing to the co-gas forming around the electrode tips.	74
Figure 4.11: Heat transfer results from slag to matte for different interface boundaries.	75

Figure 4.12: The two dimensional velocity vectors through certain plains of the furnace slice. A – Cut through the centre of both electrodes along the length of the furnace. B - Cut through the middle of one electrode towards the sidewalls showing the arc of the hearth. C – Parallel to cut B but in between the two electrodes. D – Cut along the slag concentrate interface. 77

Figure 4.13: The two dimensional velocity vectors without any gas formation around the electrodes through certain plains of the furnace slice. A – Cut through the centre of both electrodes along the length of the furnace. B - Cut through the middle of one electrode towards the sidewalls showing the arc of the hearth..... 78

Figure 4.14: Velocity distributions for the slag a) with gas formation at the electrodes and b) without gas formation at the electrodes indicating a much faster velocity in the slag with gas formation..... 79

Figure 4.15: Velocity vectors pointing in and out of the walls with the standard pressure discretization scheme..... 80

Figure 4.16: Calculated velocity vectors in the slag and matte with the 'PRESTO' discretization scheme. These velocity vectors resemble the results from *Sheng et al 1998* well in pattern and size. 81

Figure 4.17: The two dimensional velocity vectors for the VOF multiphase model through certain plains of the furnace slice. A – Cut through the centre of both electrodes along the length of the furnace. B - Cut through the middle of one electrode towards the sidewalls showing the arc of the hearth. 82

Figure 4.18: Total surface heat fluxes on the hearth of the furnace. b – indicates a plot of the heat flux from the centre of the furnaces where the heat fluxes are the highest and dropping to zero in the corner. An interesting kink is shown in the heat fluxes just off the centre..... 83

Figure 4.19: A change in refractory thickness causes a change in total surface heat fluxes in the hearth. 83

Figure 4.20: Total surface heat fluxes on the sidewall of the furnace. b – Indicates a plot of the heat flux from top of the sidewall cooling showing an increasing heat flux towards a maximum point and then decreasing again to zero at the corner of the furnace. 84

Figure 4.21: Copper cooler heat fluxes..... 84

Figure 4.22: Typical plot of the residuals during iterating. A steep drop during the initial iterations is observed and then gradually starts climbing until it stays constant. 86

Figure 4.23: Convergence monitoring of furnace slice. a) The average matte and slag temperature remaining almost 100% constant with iterations. b) indicates that the hearth temperature changes at less than 0.0003°C/iterations..... 87

Figure 4.24: Current densities at different electrode immersion depths. The highest current densities are still shown to be in the matte and not in between the electrodes for all four cases..... 89

Figure 4.25: Power dissipation in the a) slag and b) matte and concentrate. While the power generated in the slag decreases with increasing immersion depth, the power generated in the matte remains constant..... 89

Figure 4.26: The effect of immersion on the average temperature in the matte and the slag. The difference in the average temperature between matte and slag decreases with increasing electrode immersion. It is important to note here that the power generation also decreases with increasing electrode immersion as per the model parameters..... 90

Figure 4.27: Velocity vectors in the slag and the matte at different immersion depths. Higher velocity vectors are seen in the immediate vicinity of the electrodes with the deeper immersed electrodes..... 91

Figure 4.28: Velocity vectors indicating the vectors between 0 and 0.06 m/s. The areas with no vectors present are at velocities higher than 0.06 m/s. 92

Figure 4.29: Velocity vectors at different immersion depths at the copper sidewall. The velocity vectors decrease in size as the electrode immersion increases. 93

Figure 4.30: Pencil shaped electrode tip with 80% of the current flowing through the tip of the electrode and not evenly distributed as per the original assumption. 94

Figure 4.31: Comparison of the current density profiles between the flat end cylinder type electrode and the pencil shaped electrode with current flowing through the tip. The current density is significantly higher around the tip of the electrodes in the second case..... 95

Figure 4.32: Comparison of the voltage profiles between the flat end cylinder type electrode and the pencil shaped electrode with current flowing mainly through the tip. The electrode tip voltage is significantly higher at the tip of the electrode for the second case..... 95

Figure 4.33: Comparison of the joule heating profiles between the flat end cylinder type electrode and the pencil shaped electrode with current flowing

mainly through the tip. The second case shows significantly larger joule heating occurring at the tip of the electrodes..... 96

NOMENCLATURE

B	Magnetic field	T
C _p	Heat capacity	J/kgK
E	Electrical field	N/C
f,F	Force	N
h	Heat transfer coefficient	W/m ² K
I	Current	A
J	Current density	A/m ³
k	Thermal conductivity	W/mK
q	Heat flux	W/m ²
T	Temperature	K
t	time	s
ρ	Density	kg/m ³
ρ _e	Charge density	C/m ³
ε ₀	Permittivity of free space	μf/m
κ	Specific electrical conductivity	S/m
σ	Electrical conductivity	S/m
σ	Stefan Boltzman constant	W/m ² K
τ	Shear stress	Pa
γ	Surface tension	N/m
μ	Viscosity	Kg/ms
Br	Brinkman Nr Dimensionless number related to heat conduction from a wall to a viscous fluid	
C _D	Drag coefficient Coefficient of forces acting on a specific shaped particle when moving in a fluid	
Re	Reynolds number Measure of the ratio of inertial forces to viscous forces	
ε	Emissivity Ratio of energy radiated by material to energy radiated by a black body	
f _g	Geometric cell factor Constant factor that depends on geometry relating resistance to conductivity	

Chapter 1

INTRODUCTION

1.1 Background

The single six-in-line furnace at Polokwane Smelter is the largest installed high-intensity furnace for the platinum group metals and base metals sulphide smelting in the world. It treats concentrates mined from the Merensky reef as well as the UG2 reef which can contain 4% Cr₂O₃ or higher. Chrome increases the potential for undesirable precipitation of solid spinel phases which can form an intermediate zone between the slag and the matte of high viscosity or form as build-up on the hearth. This requires more intensive energy to smelt.

Fundamental to addressing the chrome issue was the selection of adequate transformer capacity to permit operation at deep electrode immersion and ability to operate at high hearth power density to substantially prevent built-up of spinel on the hearth.

Practical experience, however, shows that the deeper the electrodes are immersed in the slag bath, the higher the temperatures of the matte will be which can lead to a variety of problems and can be plain dangerous. Matte temperatures can be influenced by a number of factors such as:

- Material levels:
 - Absolute and relative depths of slag and matte
 - Depth and distribution of the concentrate layer
 - Thickness and depth of intermediate layers
 - Build-up
- Chemical / metallurgical factors:
 - Effect of flux (e.g. lime) addition to the physical properties of the slag, especially spinel stability, sulphide capacity, and slag electrical conductivity.

- Effect of variable feed mineralogy, with special reference to chrome content and matte fall due to unknown feed blend of UG2 and Merensky reef types.
- Chemical conditions that lead to excessive chrome and magnetite spinel formation
- Effect of increased MgO content of the feed.
- Matte fall as dependent on available base metal sulphides in the feedstock.
- Effect of slag chemistry on the observed (effective) viscosity
- Effect of recycles (furnace dust, reverts and magnetite-bearing slag concentrates).
- Electrode Immersion:
 - Effect of slag conductivity on electrode immersion for given resistance and power setpoints.
 - Effect of immersion in conjunction with matte proximity
 - Effect of electrode proximity along the current path
 - Effect of electrode immersion on mixing and turbulence
 - Effect of electrode immersion on current and power density
 - Effect of electrode immersion on the ratio of power dissipated in the slag vs. power dissipated in the matte.
- Factors related to the nature of the feed and its ratio to the power to the furnace:
 - Crust formation due to sintering of the concentrates, which shields the fresh concentrates from the melt and which may lead to poor melting rates and local overheating.
 - Conditions of over-power or under-feed and associated high current densities.
 - Poor electrical behaviour leading to brush-arcing.

By fundamentally understanding the energy distribution inside the furnace and the effects of electrode movements in the bath, matte and slag temperatures can be controlled and heat losses minimized, which will become even more important in future with ever increasing electrical costs.

Computational fluid dynamics (CFD) is a numerical tool to analyze the flow and heat transfer phenomena as well as coupled chemical reactions in engineering processes. The aerospace industries were the early users of CFD applications since the 1960s, but have been developing in other industrial areas such as automotive, energy, chemical and metallurgical industries since the 1980s. With the rapid growth of computer speed it can also become more popular in future as an optimization and design tool.

1.2 Plant description

Anglo Platinum's Polokwane Smelter is situated just outside Polokwane, in the Limpopo province in South Africa. Wet concentrate is received from various concentrators along the Eastern Bushveld complex with 60% of the total concentrate received being from the UG2 reef and the 40% from the Merensky reef.

After being dried in two flash driers, the concentrate is fed via airslides into the 68 MW electric immersed arc furnace with six 1.6m diameter Söderberg electrodes. The feed rate of concentrate at 68 MW is around 80 - 85 ton/hr depending on furnace conditions. Concentrate is melted by heat generated when electric current passes through the electrodes and resistive slag layer. On melting, two immiscible phases form. Furnace matte, containing the bulk of the base metal sulphides and PGMs, is denser than slag and collects naturally at the bottom of the furnace. The slag and matte are then separated by tapping the slag and matte from the furnace at two different levels of tap holes.

The furnace is constructed of a combination of refractory brick and water cooled copper coolers. The furnace sidewalls and hearth are cooled air drawn through the area by cooling fans. The copper coolers reside only on the slag zone of the furnace along the entire perimeter of the furnace. The cooler hot face has vertical and horizontal grooves cast across the entire face which forms the characteristic waffle pattern. Two independent monel pipe circuits are cast into the copper for water cooling of the copper. One staggered row of plate coolers are installed above the waffle coolers along the perimeter of the furnace. The furnace area is in the region of 30 x 10 x 6m.

The off gas is drawn from the furnace through one of two ducts situated in line with the electrodes near the slag and matte walls. The off gas will flow through a set of bag houses where filter bags will clean the gas from any concentrate particulates before it is released to the atmosphere. The off gas dust is recycled back to the furnace.

1.3 Project Objectives

The primary objectives of this project were:

- To develop expertise in CFD modelling, with the ability to critically evaluate a range of furnace operating conditions, new furnace designs or modifications to existing furnaces;

- To develop a calibrated CFD model, validated on actual operating data, which is inherently capable of handling the disturbances and set point changes imposed on the furnace.

To achieve these goals, the following specific objectives were defined for the model:

- Incorporation of sufficient phase equilibrium information to predict the presence of solids, which significantly influences the observed viscosity which, in turn, plays the dominant role in fluid flow and heat transfer.
- The incorporation of accurate physical property models for the prediction of melt (slag and matte) viscosities, thermal and electrical conductivities and densities, taking into account the significant presence of chrome in its various dissolved and crystallized states.
- Incorporation of magneto-hydrodynamics (MHD) in the CFD model to address the magnetic driving forces on the matte melt that arise from the high current densities in the matte. Heating, fluid flow and mixing are intricately coupled in alternating current systems where electromagnetic fields induce significant turbulence in conductive melts.
- Calibration of the model using actual plant measurements where possible.
- Validation of the model, again using actual plant measurement.
- Generation of a sufficiently large set of realistic scenarios / case studies based on sensitivity analyses around operating set points.

It was however clearly specified at the start of the project, that the goals and objectives could only be properly and sufficiently achieved if the project were undertaken at PhD level. However, MSc (Eng.) level outcomes were identified for a potential earlier exit-level which would provide the basic training and experience for CFD simulation. The in-depth understanding and accurate modelling of the real furnace would only be dealt with at the PhD-level.

1.3.1 MSc Objectives

To achieve the basic training and experience for the MSc (Eng) level, the objectives were:

- To identify a smaller initial, but complete project, which could be used to establish a basic understanding of the principles of CFD, which should include the

establishing of the geometry and applying an applicable grid (mesh) to it and to model basic fluid flow and heat transfer?

- To develop a model of the slice of the furnace which is to be used as basis from where it can grow in accuracy and complexity as progress is made towards a PhD.

It was, however, clearly stated that magneto-hydrodynamics (MHD), due to its complexity, as well as the validation of the model against actual plant data, would not be included on MSc (Eng) level.

Chapter 2

LITERATURE REVIEW

The objectives of the literature survey were:

A: Obtain an in depth knowledge of the operation of a six-in-line furnace

B: Understand the principles of CFD and the techniques and mathematical assumptions used to calculate a solution.

C: Study previous modelling work on six-in-line furnaces.

The modelling of a six-in-line furnace requires an in depth knowledge of the furnace operation and conditions. The aim of this chapter is therefore to obtain as much knowledge into the workings of similar furnaces and also to determine what research has already been done. The properties of the matte and slag were studied in detail but also certain furnace phenomena like bath stirring and heat generation etc to compare the CFD results obtained in this project with.

Understanding the principles of CFD, but also the techniques and mathematical assumptions used by Fluent are essential, and the models used in this study are therefore also discussed in this chapter.

Finally, before this modelling work was started, a study of all the previous modelling work on six-in-line furnaces was done to evaluate the various methods used and assumptions made to speed up the modelling work in this project and also to determine where improvements can be made.

2.1 Electrical furnaces

The electric furnace used for smelting copper and nickel sulphide ores, concentrates and other non-metallic raw materials have mainly replaced the fuel-heated reverberatory furnaces. Two types of electrical furnaces are common:

- The three electrode furnace consisting of one three phase transformer bus connected to a delta closure over the furnace roof. All the electrodes of a three electrode furnace are electrically coupled.
- The six electrode furnace consists of three single phase furnace transformers, each transformer supplying a pair of electrodes. There is virtually no electrical coupling between pairs of electrodes. This is a distinct benefit of a six electrode furnace, permitting independent control of phase power set points.

The focus of this research will be on the latter.

2.1.1 Characterization of smelting furnaces

Most electric smelting furnaces contain a molten bath of conductive metal or matte on the hearth, underlying a relatively resistive slag layer onto which unmelted charge mix is added. There are four distinctive types of electric smelting operations, characterized primarily by the mechanisms of power conversion to heat and transfer of the liberated heat to the furnace charge:

- Immersed electrode
- Open arc
- Shielded arc
- Submerged arc

In practice, the four methods are distinguished by the operational positions of the electrode tips relative to the molten bath and the presence and depth of unmelted charge cover surrounding the electrodes.

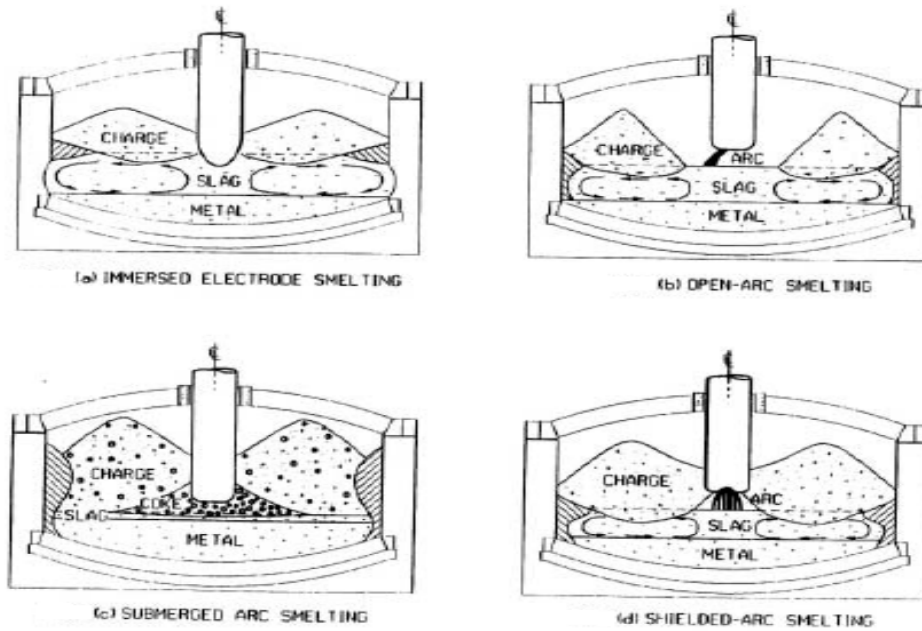


Figure 2.1: a) Immersed electrode operation. b) Open arc operation. c) Submerged arc operation. d) Shielded arc operation

For submerged arc smelting operations the electrodes are deeply buried in a conductive charge mix with micro arcing from the tips to a floating coke bed.

2.1.2 Immersed electrode operation

In the immersed electrode mode the electrode tips are immersed into the slag bath, which forms the only significant resistance in the circuit, and power is liberated solely by joule heating:

$$P_E = I^2 R_{bath} \quad (2.1)$$

The liberated heat superheats the slag locally establishing circulating flows that distribute the heat to the charge banks. Electrical conversion to heat energy is very stable. Bath resistance fluctuations and the associated power swings are very small. Low speed electrode regulation is sufficient for power set point regulation. The power factor is high, typically above 0.95.

The slag bath resistance is dependent primarily on the slag resistivity, which is dependent on slag composition and temperature, electrode size and the immersed depth of the tips into the slag. The resistance increases as the electrode tip is moved upwards from the slag metal interface to the slag surface as shown in Figure 2.2. This simple resistance to

immersion depth relationship provides the basis for regulating the furnace power. The transformer secondary voltage tap is set at the desired value and the electrodes are raised or lowered to maintain the set point resistance or impedance. Control of load resistance essentially controls furnace power through the relationship: Ma *et al.*

$$P_E = \left(\frac{V \cdot PF^2}{R_{bath}} \right) \quad (2.2)$$

P_E = Electrode power

V = Voltage

PF = Power factor

R_{bath} = Bath resistance per electrode

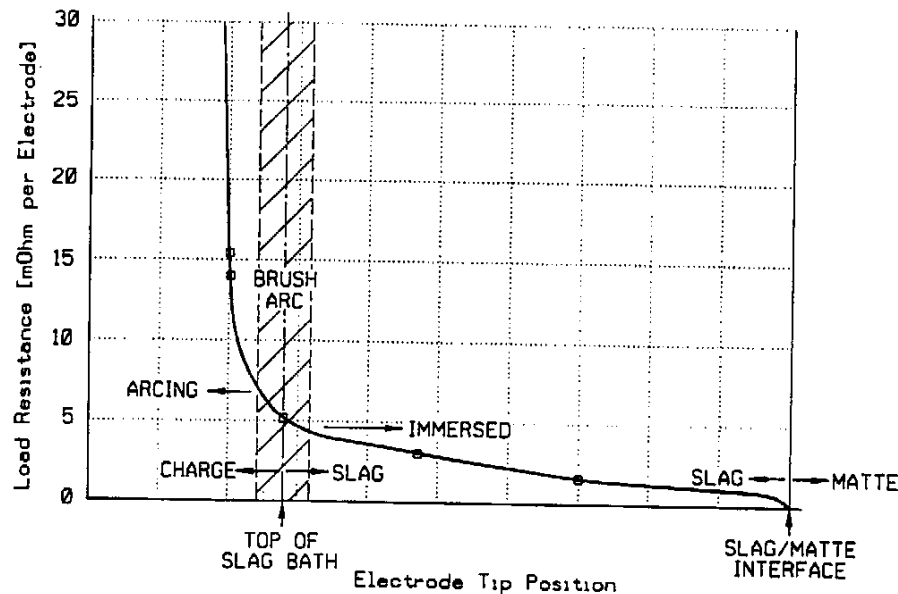


Figure 2.2: Load Resistance versus the electrode tip position. Ma *et al.*

The thickness of the slag layer is important. Barth (1961), in his review of electric smelting of sulphide ores, estimates that about $\frac{1}{4}$ to $\frac{1}{3}$ of the current passes between the electrodes and $\frac{2}{3}$ to $\frac{3}{4}$ between the tip of the electrode and the matte. This proportion will, however, depend to some extent on the electrode spacing. The matte, because of its high conductivity, plays little part in the heat generation. If the slag layer is too thin, the electrode will seek a position too close to the matte, which will lead to overheating of the hearth. On the other hand, if it is too thick, the matte will be inadequately heated. Figure 2.3 illustrates typical current flow through the matte and slag for different electrode positions.

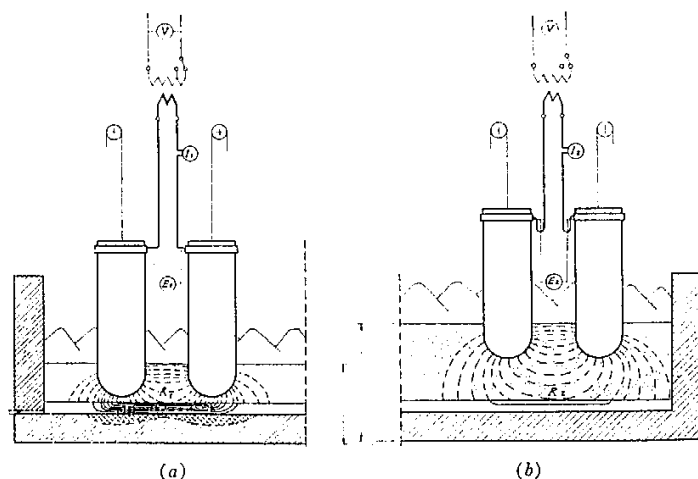


Figure 2.3: Current flow in a electric matte furnace. The slag level and electrode immersion affect the current profile as shown in a and b.

Experiments performed by Channon *et al.* (1974) showed that at electrode current densities of less than 12 A/cm^2 , it was found that the oscilloscope trace of the current flow pattern was sinusoidal and Ohm's Law obtained. It should be remembered that the magnitude of the slag resistivity under these 'submerged furnace like conditions' of high current density and low frequency is higher than the absolute resistivity as determined in fundamental studies in the Lab.

At current densities in excess of 12 A/cm^2 , the pattern of current flow was characterised by the occurrence of unstable arcing even if the electrodes were immersed in the slag. With the high current densities at the tip of the electrode, extreme localised heating occurs that leads to an increase in the rate of reaction between the carbon electrode and the slag, resulting in gaseous products (CO and SiO) The rate of reduction of SiO_2 to SiO by carbon at temperatures greater than 1500 deg C is rapid and this mechanism was confirmed.

It was found by Sheng *et al.* (1998 part 1), as mentioned earlier in this report, that there is a substantial voltage drop at the electrode interface 100 to 120V for applied potentials of 180 to 230 V for the Falconbridge furnace. This potential drop was attributed to the creation of an arc from the carbon monoxide evolved at the electrodes due to chemical erosion. Therefore, heat is evolved both at the electrode surface and in the bulk of the slag by ohmic heating. The resistance of the arc increases with applied potential, but the resistance due to arcing is not a strong function of immersion depth.

2.1.3. Bath Stirring

Bath stirring is a major contributor to heat distribution in the slag and the matte and can also be an important tool to ensure that smaller matte particles collide with each other and therefore settling to the bottom of the furnace sooner. Stirring in the bath occurs mainly due to natural convection, formation of bubbles at the electrodes and electromagnetic forces which are discussed in the following sections.

2.1.3.1 Natural convection in the slag.

Natural convection takes place in the slag, because the density of the slag changes with temperature. This will be discussed in more detail in a later section. As the area around the electrode is at a higher temperature the slag density will decrease, which will cause it to rise. The slag closer to the outer wall will, however, start cooling down because of the heat losses to the outer wall and the density will therefore increase causing the slag to settle. The effect is therefore a circulation of slag moving away from the electrode towards the outer wall where it starts cooling down and dropping down from where it will move from the outer wall along the bottom of the slag layer towards the electrode until the temperature starts increasing again, causing the slag to rise towards the electrode. The natural convection is therefore to a large extent determined by the dependency of the material density on the temperature.

2.1.3.2 Bubble stirring

With the high current densities at the tip of the electrode extreme localised heating occurs, that leads to an increase in the rate of reaction between the carbon electrode and the slag, resulting in gaseous products (CO and SiO) The rate of reduction of SiO₂ to SiO by carbon at temperatures greater than 1500 deg C is rapid and this mechanism was confirmed. These gaseous products, as they rise to the top of the slag, cause an additional stirring effect in the slag in the same direction as the natural convection.

2.1.3.3 Magnetohydrodynamics (MHD) as stirring force

Magnetohydrodynamic force, or Lorentz force, also contributes to the stirring forces in the bath. It has been found by numerous authors like Choudhary and Szekely, Jardy *et al.* Sheng *et al.* (1998 part 2) and Hadley *et al* (2006) that for large scale operations this force is negligible in comparison to natural convection forces. Sheng *et al* (1998 part 2), found that electromagnetic stirring force is of the order of 1% of the natural convection

and bubble-driven forces. No research, however, shows the stirring forces in the matte and mainly focuses on the slag. MHD is discussed in more detail in the following section.

2.2 Magnetohydrodynamics (MHD)

Magnetohydrodynamics as per Davidson (2000), is the study of the interaction between magnetic fields and moving conducting fluids. The mutual interaction of a magnetic field, B , and a velocity field u arises partially as a result of the laws of Faraday and Ampere, and partially because of the Lorentz force experienced by a current-carrying body. Now the only difference between MHD and conventional electrodynamics lies in the fluidity of the conductor and therefore many of the important features of MHD are latent in electrodynamics.

2.2.1 The Governing equations of electrodynamics

It is assumed that the material properties such as the conductivity are spatially uniform and that the medium is incompressible. The laws that will be discussed are the Ohm's law, Ampere's law, Faraday's law and the Lorentz force.

2.2.1.1 The electrical field and the Lorentz force

A particle moving at a certain velocity and carrying a charge is generally subject to three forces:

$$f = qE_s + qE_i + qu \times B \quad (2.3)$$

The first is the electrostatic force, or Coulomb force, which arises from the mutual repulsion or attraction of electrostatic charges (E_s is the electrostatic field). The second is the force which the charge experiences in the presence of a time-varying magnetic field, E_i being the electrical field induced by the changing magnetic field. The third contribution is the Lorentz force which arises from the motion of charge in a magnetic field.

The electric field can be defined as:

$$E = E_s + E_i \quad (2.4)$$

Now if equation 2.4 is combined with Gauss's law (2.5) and Faraday's law (2.6), 2.3 can be re-written as equation 2.7:

$$\nabla \cdot E = \frac{\rho_e}{\epsilon_0} \quad (2.5)$$

$$\nabla \times E = -\frac{\partial B}{\partial t} \quad (2.6)$$

$$f = q(E + u \times B) \quad (2.7)$$

2.2.1.2 Ohms Law and the volumetric Lorentz force

In a stationary conductor it is found that the current density, J , is proportional to the force experienced by the free charges. This is reflected by the conventional form of Ohm's law:

$$J = \sigma E \quad (2.8)$$

In a conducting fluid the same law applies, only now the electrical field is measured in a frame moving with the local velocity of the conductor:

$$J = \sigma E_r = \sigma(E + u \times B) \quad (2.9)$$

Now in MHD the individual charges are of much less concern than the bulk force acting on the medium and equation 2.7 is therefore summed over a unit volume and becomes:

$$F = \rho_e E + J \times B \quad (2.10)$$

Conservation of charge requires that:

$$\nabla \cdot J = -\frac{\partial \rho_e}{\partial t} \quad (2.11)$$

Equation 2.11 simply states that the rate at which charge is decreasing inside a small volume is equal to the rate at which charge flows out across the surface of that volume. It is assumed here, however, that the charge density is so small that equation 2.11 simplifies to:

$$\nabla \cdot J = 0 \quad (2.12)$$

As the charge density is very small (it is too small to produce any significant electric force) $\rho_e E$, the Lorentz force in equation 2.10, completely dominates and is therefore written as:

$$F = J \times B \quad (2.13)$$

2.2.1.3 Ampere's law

The differential form of Ampere's law states that:

$$\nabla \times B = \mu J \quad (2.14)$$

Maxwell introduced a new term, however, as a correction to equation 2.14, called the displacement current:

$$\nabla \times B = \mu \left(J + \varepsilon_0 \frac{\partial E}{\partial t} \right) \quad (2.15)$$

2.2.2 Maxwell's equations

The Maxwell's equations embody all that we know about electrodynamics:

$$\nabla \cdot E = \frac{\rho_e}{\varepsilon_0} \quad (\text{Gauss's law}) \quad (2.5)$$

$$\nabla \cdot B = 0 \quad (\text{Solenoidal nature of B}) \quad (2.16)$$

$$\nabla \times E = -\frac{\partial B}{\partial t} \quad (\text{Faraday's law in differential form}) \quad (2.6)$$

$$\nabla \times B = \mu \left(J + \varepsilon_0 \frac{\partial E}{\partial t} \right) \quad (\text{Ampere-Maxwell equation}) \quad (2.15)$$

As well as:

$$\nabla \cdot J = \frac{\partial \rho_e}{\partial t} \quad (\text{charge conservation}) \quad (2.11)$$

$$F = q(E + u \times B) \quad (2.7)$$

These equations can, however, be simplified. In MHD the charge density plays no significant role and the electric force is minute in comparison with the Lorentz force. It can also be assumed that the displacement currents are negligible by comparison with the current density so the Ampere-Maxwell equation reduces to the differential form of Ampere's law. When these simplified equations are summarised, they encapsulate all we need to know about electromagnetism for MHD.

Ampere's law plus the charge conservation:

$$\nabla \times B = \mu J, \quad \nabla \cdot J = 0 \quad (2.14)(2.12)$$

Faraday's law plus the solenoidal constraint on B:

$$\nabla \times E = -\frac{\partial B}{\partial t}, \quad \nabla \cdot B = 0 \quad (2.6)(2.16)$$

Ohm's law plus the Lorentz force:

$$J = \sigma(E + u \times B), \quad F = J \times B \quad (2.9)(2.13)$$

2.3 Material Properties

In order to obtain a good understanding of the behaviour of the slag, matte and concentrate, a detailed study of the material properties was done and summarized in the following sections.

2.3.1 Slag Viscosity

Eric (2004) showed that with increasing basicity, the viscosity decreases at constant temperature and the resistivity also decreases. The slag liquidus temperature increases with increasing basicity. It also shows the effect of Fe content on the slag properties.

The specific resistivity and the viscosity increase with increasing distance from the furnace centre. The tendency is that, with the increase of temperature, the gradients of both viscosity and resistivity become steeper, which will give rise to buoyancy effects.

Eric and Hejja (1995 part 2), also expressed the temperature gradient of viscosity vs the slag composition.

$$\lambda\eta = \frac{\eta^1 - \eta^2}{(T1 - T2)\eta_{avg}} \quad (2.17)$$

$\lambda\eta$ = temperature gradient of viscosity

Eric and Hejja (1995 part 1), found that the action of the electrical conductivity and viscosity is opposing. Increasing conductivities are associated with decreasing viscosity.

Utigard (2000), showed that the viscosity of both fayalite slags and Fe-Ni slags can be calculated with the viscosity ratio:

$$VR = \frac{wt\%SiO_2}{1.2wt\%FeO + 0.5wt\%Fe_2O_3 + 0.8wt\%MgO}$$

$$\log \mu = -0.49 - 5.1VR^{0.5} + \frac{12.080VR^{0.5} - 3660}{T}$$

T in Kelvin

μ in Pa.s

The presence of undissolved solids, product prills or slag precipitates within the slag, will increase the viscosity above that calculated, using this equation.

2.3.2 Slag density

Gunnewiek and Tullis (1996), evaluated the slag density as a function of temperature based on the following approximate temperature:

$$\beta \approx \frac{1}{\rho} \left(\frac{\rho - \rho_o}{T - T_o} \right)_p \quad (2.18)$$

β = Volumetric thermal expansion coefficient

ρ_o = reference density at

T_o = reference temperature

Utigard (2000) calculated the density for the following types of slag as follows:

For Fayalite slag:

$$\rho = 5.000 - 30(\text{wt}\% \text{SiO}_2 + \text{wt}\% \text{Fe}_2\text{O}_3) - (T - 1200) \quad (2.19)$$

P in kg/m³ and T in deg C

For Fe-Ni slag:

$$\rho = 2.680 + 581 \left(\frac{\text{wt}\% \text{FeO}}{\text{wt}\% \text{SiO}_2} \right) - 0.3(T - 1450) \quad (2.20)$$

It was found that in furnaces where most of the feed is consumed around the electrodes it has been seen that the density can easily increase more than one percent and counteracts the one-percent decrease in density a 100°C increase would cause. It has also been observed that, in extreme cases in the region around the electrodes, the density can increase and cause the flow to reverse with a circulating loop in the opposite direction.

2.3.3 Slag electrical conductivity

Hundermark (2003), studied the electrical conductivity of melter type slags in detail and derived correlations for iron-free and iron-containing slag systems. All the data for the iron-free and iron-containing slag systems were then combined in a unified model. The following correlation was then derived for the electrical conductivity of slags containing two or more of the following components: Al₂O₃, CaO, FeO_x, MgO and SiO₂:

$$\begin{aligned}
\ln \kappa = & \left(19.9 - \frac{47348}{T}\right) \cdot X_{Al_2O_3} + \left(15.4 - \frac{24087}{T}\right) \cdot X_{CaO} + \left(9.2 - \frac{14151}{T}\right) \cdot X_{MgO} \\
& + \left(-0.5 - \frac{7478}{T}\right) \cdot X_{SiO_2} + \left(10.0 - \frac{9140}{T}\right) \cdot X_{FeO} \cdot Fe^{2+} \\
& + \left(65.4 - \frac{82447}{T}\right) \cdot X_{FeO}^2 \cdot Fe^{2+} \cdot Fe^{3+} + \left(-2.6 + \frac{6642}{T}\right) \cdot X_{FeO} \cdot Fe^{3+}
\end{aligned} \tag{2.21}$$

X represents the mole fractions of the components, T is in Kelvin and Fe^{2+} and Fe^{3+} are the fractions of ferrous and ferric ions respectively.

The electrical conductivities of all the slag systems studied in literature increased with increasing temperature.

It was also found by Hundermark (2003), that the addition of chromium to slag containing Al_2O_3 -CaO- FeO_x -MgO- SiO_2 is likely to bring about a decrease in the electrical conductivity of the slag. It is likely that the decrease is caused by the precipitation of a spinel phase containing Al, Fe, and Mg ions. The locking up of conducting Fe and Mg cations in the spinel phase is considered to cause the decrease in the conductivity. The trend of decreasing conductivity with increasing chromium content can be reproduced with Hundermark's equation if it is assumed that the spinel phase and the Cr ions in the liquid slag did not contribute to the conductivity.

In the literature review by Sheng *et al.* (1998 part 2), it is reported that resistance of a slag is inversely proportional to its conductivity:

$$R_s = \frac{f_g}{\kappa} \tag{2.22}$$

Where R_s is the total resistance of the slag between electrodes and f_g is the geometric factor and depends on the geometry of the cell.

2.3.4 Viscous heating

When a fluid is sheared, some of the work done is dissipated as heat. This shear-induced heating gives an inevitable increase in temperature within the fluid. (Yesilata 2002)

Viscous heating will be important when the Brinkman nr approaches or exceeds unity.

$$Br = \frac{\mu U_e^2}{k\Delta T} \quad (2.23)$$

2.3.5 Magnetic Permeability

The magnetic permeability of solid ferro- and ferrimagnetic materials (iron and magnetite) is dependent on the applied magnetic field and therefore experiences magnetic hysteresis. A hysteresis loop occurs when an alternating magnetic field is applied to the material and its magnetization traces out a loop called a hysteresis loop which doesn't relax back to zero magnetism when the magnetic field is removed. Energy losses are proportional to the area inside the hysteresis loop. High energy losses are usually associated with hard magnetic materials and smaller losses are associated with soft magnetic materials. All materials will lose their ferro/ferrimagnetism above the Currie temperature though.

Above the Currie temperature (<1000°C for all metals) all materials are either paramagnetic or diamagnetic, which include metals in the fluid phase like iron. Paramagnetic materials have the tendency to align with the magnetic field, but they lose their magnetic properties when the magnetic field is removed, and hysteresis therefore doesn't occur.

For paramagnetic materials the magnetic susceptibility is very small, but positive, and will decrease with increasing temperature, but is independent of the magnetic field strength. The relative permeability will therefore be close to one, but positive.

Diamagnetic materials will experience very little magnetism and will be opposite in direction to the applied magnetic field. Diamagnetic materials therefore have negative susceptibilities and its permeability's will be close to one, but negative. (Eksteen 2007)

2.3.6 Interfacial Tension and surface tension

Eric (2004), found that when the interfacial tension between matte and slag is low, the matte is wet by the slag and the settling velocity of the matte prills is reduced. The tendency for coalescence should increase with increasing interfacial tension, but it also depends on viscosity. Due to a severe lack of data on interfacial tensions pertinent to the

slag-matte systems encountered in an electric arc furnace, a rather indirect approach was adopted by using surface tensions available.

At 1400°C, the expression used in the calculation of the surface tension of slag in dynes/cm is:

$$\gamma = 570X_{FeO} + 285X_{SiO_2} + 640X_{Al_2O_3} + 614X_{CaO} + 512X_{MgO} \quad (2.24)$$

The magnitude of the surface tension in the slags, studied under operating conditions, is between 420 and 460 dynes/cm (0.42-0.46 N/m) and tends to increase with total iron, CaO, MgO and basicity ratio. Increasing SiO₂, in agreement with literature, decreases the surface tension.

According to Eric (2004), a direct relationship between matte-slag separation efficiency and surface tension appears to exist.

Mnasell, as reported in Sheng *et al.* (1998 part 2), investigated the interface between the fluid flowing in a channel and another immiscible fluid inside a square cavity below the channel and used the following equation as a boundary condition:

$$\tau_{xy}^- - \tau_{xy}^+ = \frac{d\sigma_o}{dy} \quad (2.25)$$

τ_{xy}^+ = shear stress in upper moving liquid

τ_{xy}^- = resisting shear in the lower liquid

σ_o = the surface tension

The interfacial tension between matte and slag is 300 to 500 mN/m.

Vaisburd and Brandon (1997), found the following relationship (see Figure 2.4) between the surface tension and temperature of a slag with composition 38% CaO, 20% Al₂O₃ and 42% SiO₂ (eutectic composition). The statistical analysis of the measuring instruments' error and the statistical treatment of the measured data gave an uncertainty of 3% for the surface tension. Similar results were obtained for the density and viscosity of the same slag system.

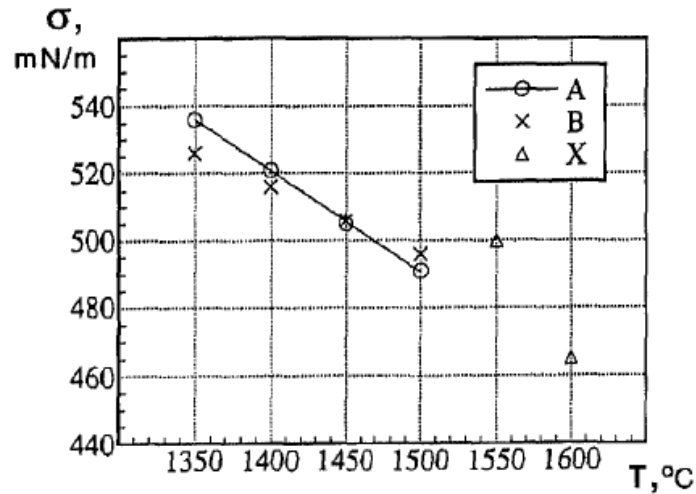


Figure 2.4: The surface tension of the ternary eutectic melt (.38% CaO, 20% Al₂O₃, 42% SiO₂). A – Vaisburd results, B – Elliot’s results, X – Slag Atlas 95 results

2.4 CFD

According to *Anderson (1995)* Computational Fluid Dynamics (CFD) is the science of predicting fluid flow, heat and mass transfer, chemical reactions and related phenomena by solving numerically a set of governing mathematical equations.

The results of CFD analysis are relevant in:

- Conceptual studies of new designs
- Understanding the process better
- Detailed product development
- Troubleshooting
- Redesign

The basic steps of a CFD analysis are as follows:

- *Pre-processing*: Identify the modelling goal and domain to be modelled. Design and create the grid
- *Solver Execution*: Set-up of the numerical model, boundary conditions and computing and monitor the solutions.
- *Post-processing*: Colour postscript output. Examination of the results and validating of model.

2.4.1 CFD codes

There are several commercial CFD packages on the market for example Phoenics, Fluent, Fidap, Flow-3D and CFDS-Flow3D. The available packages differ from one another in some aspects, for instance: multiphase flow, particle tracking, free surface flows, compressible flows, turbulence models, radiation heat transfer models, chemical reactions as well as numerical methods and mesh structure.

Fluent, a general-purpose CFD code, will be used in this study.

Fluent, first released in 1983, addresses a wide range of applications across many industries. In the automotive industry it is used from full vehicle aerodynamics and under hood cooling to climate control and power train design. In the chemical, oil-gas and process industry it is used to model separators, reactors, packed beds, fluidised beds, stirred tanks and heat and mass transfer equipment. In power industries it is used for combustion system modelling, furnace design and air or particulate handling and classification. Other applications include glass processing, metal processing, turbo machinery etc.

2.4.2 CFD principles and governing equations

All of CFD is based on the fundamental governing equations of fluid dynamics – the continuity, momentum and energy equations. The mathematical statement of the three fundamental physical principles upon which fluid dynamics is based is:

1. Mass is conserved
2. Newton's second law, $F = ma$
3. Energy is conserved.

Although a couple of different methods can be followed to derive the equations, the principles remain the same. A couple of different methods include the *Finite Volume Method (FVM)*, *Finite Difference Method (FDM)*, *Finite Element Method (FEM)*, and *Spectral Method*. As Fluent uses the Finite Volume Method, as well as most other commercial CFD codes, this method will be used to explain some of the governing equations.

There are also many different notations and ways of deriving these conservation equations. This paper follows the notations as explained by Reuter and Yang (2000).

2.4.2.1 Continuity Equation

Physical Principle: Mass is conserved

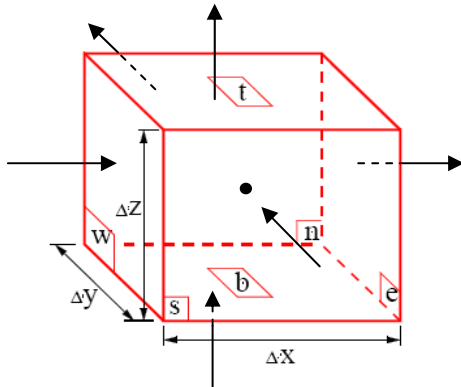


Figure 2.5: Mass flows into and out of the fluid element for developing the continuity equation.

According to the physical principle that mass is conserved, it can be said that the rate of change of density (mass per unit volume) equals the net flow of mass into the element cross its boundaries.

Rate of increase of mass in fluid element	=	Net rate of flow of mass into fluid element
---	---	---

$$\frac{\partial \rho}{\partial t} = -\text{div}(\rho \mathbf{u}) \quad (2.26)$$

For incompressible fluids, the density is constant ($\frac{\partial \rho}{\partial t} = 0$) and the continuity equation becomes:

$$\text{div}(\mathbf{u}) = 0 \quad \text{or} \quad \frac{\partial u}{\partial x} + \frac{\partial v}{\partial y} + \frac{\partial w}{\partial z} = 0 \quad (2.27)$$

2.4.2.2 Momentum conservation

This equation is also called the Navier Stokes equation and state that the rate of change of momentum equals the sum of forces acting on the fluid particle.

Rate of momentum increase	=	Net rate of momentum into the element	+	Sum of forces acting on the element
---------------------------	---	---------------------------------------	---	-------------------------------------

$$\frac{\partial}{\partial t}(\rho u) + \text{div}(\rho u u) = \text{div}(\mu \text{grad } u) - \frac{\partial p}{\partial x} + S_F \quad (2.28)$$

$\frac{\partial}{\partial t}(\rho u)$: Rate of momentum increase of the fluid element.

$\text{div}(\rho u u)$: Net rate of momentum into the fluid element.

$\text{div}(\mu \text{grad } u)$: Surface force on the element due to viscous stress.

$-\frac{\partial p}{\partial x}$: Surface force on the element due to pressure gradient.

S_F : Different body forces – gravity, centrifugal, coriolis or electromagnetic forces.

2.4.2.3 Thermal energy conservation or enthalpy equation

The first law of thermodynamics states that the rate of change of energy equals the sum of the rate of heat addition to and the rate of work done on a fluid element.

Rate of increase of enthalpy in the fluid element	=	Convective heat into the element	+	Conduction heat into the element	+	Pressure work	+	Mech work	+	Other sources
---	---	----------------------------------	---	----------------------------------	---	---------------	---	-----------	---	---------------

$$\frac{\partial}{\partial t}(\rho h) + \text{div}(\rho u h) = \text{div}(k \text{ grad } T) + \frac{dp}{dt} + \phi + S_h \quad (2.29)$$

$\frac{\partial}{\partial t}(\rho h)$: Rate of enthalpy increase in the fluid element

$-\text{div}(\rho u h)$: Convective heat.

$\text{div}(k \text{ grad } T)$: Conduction heat

$\frac{dp}{dt}$: Pressure work

ϕ : Mechanical work

S_h : Other sources

2.4.3 Defining properties

An important step in the setup of the model is to define the materials and their physical properties. Properties may be temperature-dependent and/or composition-dependent, with temperature dependence based on a polynomial, piecewise-linear, or piecewise-polynomial function and individual component properties either defined by you or computed via kinetic theory.

The methods of defining these properties that were used and considered will be discussed here and were obtained from the Fluent users guide (2005).

2.4.3.1 Piecewise-linear functions

A piecewise-linear function of temperature for a material property follows the following equation:

$$\phi(T) = \phi_n + \frac{\phi_{n+1} - \phi_n}{T_{n+1} - T_n}(T - T_n) \quad (2.30)$$

where $1 \leq n \leq N$ and N is the number of segments.

If the temperature exceeds the maximum Temperature (T_{\max}) you have specified for the profile, the value corresponding to T_{\max} will be used. If the temperature falls below the minimum Temperature (T_{\min}) specified for the profile, the value corresponding to T_{\min} will be used in the calculations.

2.4.3.2 The Boussinesq model

For many natural-convection flows, you can get faster convergence with the Boussinesq model than you can get by setting up the problem with fluid density as a function of temperature. This model treats density as a constant value in all solved equations, except for the buoyancy term in the momentum equation.

$$(\rho - \rho_0)g \approx -\rho_0\beta(T - T_0)g \quad (2.31)$$

where ρ is the (constant) density of the flow, T_0 is the operating temperature, and β is the thermal expansion coefficient. Equation 2.31 is obtained by using the Boussinesq approximation $\rho = \rho_0(1 - \beta\Delta T)$ to eliminate ρ from the buoyancy term. This approximation is accurate as long as changes in actual density are small; specifically, the Boussinesq approximation is valid when $\beta(T - T_0) \ll 1$.

2.4.4 Magnetic Hydrodynamics Model (MHD)

Magnetohydrodynamics (MHD) refers to the interaction between an applied electromagnetic field and a flowing, electrically-conductive fluid. The coupling between the fluid flow field and the magnetic field can be understood on the basis of two fundamental effects: the induction of electric current due to the movement of conducting material in a magnetic field, and the effect of Lorentz force as the result of electric current and magnetic field interaction.

Except for the stirring effect it may have on the liquid material, it is also used as the heat source for the furnace when the current is passing through the slag and matte. Two approaches can be used to model the flow of current through the bath. One is through the solution of a magnetic induction equation and the other is through solving an electric potential equation for which the latter will be discussed here.

The electric potential equation is given by:

$$\nabla^2 \varphi = \nabla \cdot (\vec{U} \times \vec{B}_0) \quad (2.32)$$

The boundary condition for the electric potential is given by:

$$\frac{\partial \varphi}{\partial n} = (\vec{U} \times \vec{B}_0)_{\text{boundary}} \cdot \vec{n} \quad (2.33)$$

Depending on what is specified at the boundary, the electric potential or the current density is then calculated, which is then used to calculate the Joule heating rate, which is the additional source term for the energy equation. The Joule heating is calculated as follows, which has units of W/m^3 .

$$Q = \frac{1}{\sigma} \vec{j} \cdot \vec{j} \quad (2.34)$$

For multiphase flows, assuming that the electric surface current at the interface between phases can be ignored, the electric conductivity for the mixture is given by:

$$\sigma_m = \sum_i \sigma_i v_i \quad (2.35)$$

which uses the electric conductivity and the volume fraction of each phase to calculate the mixture conductivity. This will be discussed in more detail in the multiphase modelling section when the mixture properties are discussed.

2.4.5 Multiphase modelling

Physical phases of matter are gas, liquid, and solid, but the concept of phase in a multiphase flow system is applied in a broader sense. In multiphase flow, a phase can be defined as an identifiable class of material that has a particular inertial response to and interaction with the flow and the potential field in which it is immersed. For example, different-sized solid particles of the same material can be treated as different phases, because each collection of particles with the same size will have a similar dynamical response to the flow field.

Currently there are two approaches for the numerical calculation of multiphase flows: the Euler-Lagrange approach and the Euler-Euler approach. The Euler-Lagrange approach will

be further discussed in the Discrete Phase modelling section (2.4.6). Three different Euler-Euler multiphase models are available: the volume of fluid (VOF) model, the mixture model, and the Eulerian model. The VOF and the mixture model will be discussed in the following sub-sections.

2.4.5.1 The Volume of fluid method (VOF)

It is designed for two or more immiscible fluids where the position of the interface between the fluids is of interest. In the VOF model, a single set of momentum equations is shared by the fluids, and the volume fraction of each of the fluids in each computational cell is tracked throughout the domain.

The VOF formulation therefore relies on the fact that two or more fluids (or phases) are not interpenetrating. The tracking of the interface(s) between the phases is accomplished by the solution of a continuity equation for the volume fraction of one (or more) of the phases. For the q^{th} phase, this equation has the following form:

$$\frac{1}{\rho_q} \left[\frac{\partial}{\partial t} (\alpha_q \rho_q) + \nabla \cdot (\alpha_q \rho_q \bar{v}_q) \right] = S_{\alpha_q} + \sum_{p=1}^n (\dot{m}_{pq} - \dot{m}_{qp}) \quad (2.36)$$

where \dot{m}_{qp} is the mass transfer from phase q to phase p and \dot{m}_{pq} is the mass transfer from phase p to phase q and S is the source term. For the phases the following equation is applicable:

$$\sum_{q=1}^n \alpha_q = 1 \quad (2.37)$$

where n is equal to the number of phases present.

The properties appearing in the transport equations are determined by the presence of the component phases in each control volume according to the following equation:

$$\rho = \sum \alpha_q \rho_q \quad (2.38)$$

All the other properties are computed in this manner.

A single momentum equation is solved throughout the domain, and the resulting velocity field is shared among the phases. The momentum equation, shown below, is dependent on the volume fractions of all phases through the density and viscosity properties.

$$\frac{\partial}{\partial t}(\rho\vec{v}) + \nabla \cdot (\rho\vec{v}\vec{v}) = -\nabla p + \nabla \cdot [\mu(\nabla\vec{v} + \nabla\vec{v}^T)] + \rho\vec{g} + \vec{F} \quad (2.39)$$

One limitation of the shared-fields approximation is that in cases where large velocity differences exist between the phases, the accuracy of the velocities computed near the interface can be adversely affected.

The energy equation is also shared among the phases in a similar fashion as the momentum equation. The energy and temperature is treated as mass averaged variables though according to the equation below.

$$E = \frac{\sum_{q=1}^N \alpha_q \rho_q E_q}{\sum_{q=1}^n \alpha_q \rho_q} \quad (2.40)$$

where E_q for each phase is based on the specific heat of that phase and the shared temperature.

2.4.5.2 Mixture Model

The mixture model, like the VOF model, uses a single-fluid approach. It differs from the VOF model in two respects:

- The mixture model allows the phases to be interpenetrating. The volume fractions for a control volume can therefore be equal to any value between 0 and 1, depending on the space occupied by phase q and phase p.
- The mixture model allows the phases to move at different velocities, using the concept of slip velocities. The phases can also be assumed to move at the same velocity.

The mixture model solves the continuity-, the momentum- and the energy equation for the mixture, and the volume fraction equation for the secondary phases, as well as

algebraic expressions for the relative velocities (if the phases are moving at different velocities).

The continuity equation for the mixture model can be calculated according to the following equation:

$$\frac{\partial}{\partial t}(\rho_m) + \nabla \cdot (\rho_m \vec{v}_m) = 0 \quad (2.41)$$

where the mass-averaged velocity is used:

$$\vec{v}_m = \frac{\sum_{k=1}^n \alpha_k \rho_k \vec{v}_k}{\rho_m} \quad (2.42)$$

The mixture density is calculated similar to the density calculation in the VOF model as can be seen in equation 2.38.

The momentum equation for the mixture can be obtained by summing the individual momentum equations for all the phases and can be expressed as:

$$\begin{aligned} \frac{\partial}{\partial t}(\rho_m \vec{v}_m) + \nabla \cdot (\rho_m \vec{v}_m \vec{v}_m) = -\nabla p + \nabla \cdot [\mu_m (\nabla \vec{v}_m + \nabla \vec{v}_m^T)] + \\ \rho_m \vec{g} + \vec{F} + \nabla \cdot \left(\sum_{k=1}^n \alpha_k \rho_k \vec{v}_{dr,k} \vec{v}_{dr,k} \right) \end{aligned} \quad (2.43)$$

where F is a body force and the viscosity of the mixture is calculated in a similar fashion as the density of the mixture.

The drift velocity for the secondary phase is calculated as follows:

$$\vec{v}_{dr,k} = \vec{v}_k - \vec{v}_m \quad (2.44)$$

The energy equation takes the following form:

$$\frac{\partial}{\partial t} \sum_{k=1}^n (\alpha_k \rho_k E_k) + \nabla \cdot \left(\sum_{k=1}^n \alpha_k \vec{v}_k (\rho_k E_k + p) \right) = \nabla \cdot (k_{eff} \nabla T) + S_E \quad (2.45)$$

where k_{eff} is the effective conductivity being used according to:

$$k_{\text{eff}} = \sum \alpha_k (k_k + k_t) \quad (2.46)$$

with k_t being the turbulent thermal conductivity according to the turbulence model being used.

$$E_k = h_k - \frac{p}{\rho_k} + \frac{v_k^2}{2} \quad (2.47)$$

Equation 2.47 for the calculation of E_k is applicable for incompressible phases, but for compressible phases as in this study, the last two terms on the right falls away.

From the continuity equation for the secondary phase p, the volume fraction equation for the secondary phase p can be obtained from:

$$\frac{\partial}{\partial t} (\alpha_p \rho_p) + \nabla \cdot (\alpha_p \rho_p \vec{v}_m) = -\nabla \cdot (\alpha_p \rho_p \vec{v}_{dr,p}) + \sum_{q=1}^n (\dot{m}_{qp} - \dot{m}_{pq}) \quad (2.48)$$

2.4.6 Discrete phase modelling

In addition to solving the transport equations for a continuous phase, a discrete second phase can be simulated in a Lagrangian frame of reference. The second phase consists typically of particles (which may represent droplets or bubbles and in this study the bubbles released at each electrode) dispersed in the continuous phase. The trajectories of these discrete phase entities, as well as the heat and mass transfer to and from them are computed and the coupling between the phases and its impact on both the discrete phase trajectories and the continuous flow can be included.

The trajectory of the discrete phase particle is predicted by integrating the force balance on the particle which is written in a Lagrangian reference frame. This force equates the particle inertia with the forces acting on the particle and can be written for the x direction (in Cartesian coordinates) as:

$$\frac{du_p}{dt} = F_D (u - u_p) + \frac{g_x (\rho_p - \rho)}{\rho_p} + F_x \quad (2.49)$$

where F_x is an additional acceleration (force/unit particle mass) term and the first term on the right is the drag force per unit particle mass with:

$$F_D = \frac{18\mu}{\rho_p d_p^2} \frac{C_D \text{Re}}{24} \quad (2.50)$$

the subscript p indicates the particle. Re is the relative Reynolds number which is defined as:

$$\text{Re} \equiv \frac{\rho d_p |u_p - u|}{\mu} \quad (2.51)$$

The drag coefficient is calculated by:

$$C_D = a_1 + \frac{a_2}{\text{Re}} + \frac{a_3}{\text{Re}^2} \quad (2.52)$$

where a_1 , a_2 and a_3 are constants, that apply to smooth spherical particles over several ranges of Re. The drag coefficient for particles with a different shape is calculated differently, but won't be discussed here as it is not applicable to this study. Please see the Fluent users guide for more information.

2.4.7 Boundary Conditions

Boundary conditions specify the flow and thermal variables on the boundaries of the physical model and are critical components of the simulation. Various different types of boundaries can be specified in a CFD simulation of which only the relevant types will be discussed here.

2.4.7.1 Walls

Wall boundaries are used to bound fluid and solid regions. The parameters set at each wall can include wall heat transfer specification, wall movement, and the surface emissivity for thermal radiation. Different options for specifying the wall heat transfer are available:

- coupled walls, which have the same temperature on either side and are used to separate fluid and/or solid zones
- fixed temperatures, where the temperatures at the wall are known or measured

- fixed heat fluxes or non-conductive or isolated boundaries when zero heat flux is specified
- convection heat transfer
- radiation heat transfer
- combined convection and radiation boundaries
- boundaries which include shell conduction

When a convective heat transfer boundary condition is specified at a wall, the inputs from the user of the external heat transfer coefficient and external heat sink temperature are used to compute the heat flux to the wall as follows:

$$q = h_{ext}(T_{ext} - T_w) \quad (2.53)$$

h_{ext} = external heat transfer coefficient defined by the user

T_{ext} = external heat-sink temperature defined by the user

When the external radiation boundary condition is used, the heat flux to the wall is calculated as follows:

$$q = \varepsilon_{ext}\sigma(T_{\infty}^4 - T_w^4) \quad (2.54)$$

ε_{ext} = emissivity of the external wall surface defined by the user

σ = Stefan-Boltzmann constant

T_w = surface temperature of the wall

T = temperature of the radiation source or sink on the exterior of the domain as defined by the user

For the combined external heat transfer condition, equations 2.53 and 2.54 are added together to calculate a combined heat flux to the wall.

It is also possible to specify a wall thickness with a corresponding heat transfer coefficient which will calculate the heat conduction through this wall with the defined thickness normal to the wall. When the shell conduction is activated however, the heat transfer through this wall with the defined thickness will be calculated in all directions in this wall.

The shear stress at each wall can be defined with the default setting on a no-slip condition as also used in this model.

2.4.7.2 Symmetry planes

Symmetry boundary conditions are used when the physical geometry of interest and the expected pattern of the flow/thermal solution have mirror symmetry. Symmetry planes therefore imply a zero flux of all quantities across the boundary. There is no convective flux across a symmetry plane; the normal velocity component at the symmetry plane is thus zero. There is no diffusion flux across a symmetry plane; the normal gradients of all flow variables are thus zero at the symmetry plane.

2.4.7.3 Moving solid zones

A “solid” zone is a group of cells for which only a heat conduction problem is solved; no flow equations are solved. The only required input for a solid zone is therefore the type of solid and its properties.

The solid region can also be specified with a specific motion.

2.4.8 Numerical Solution

The technique used by Fluent to solve the governing integral equations for the conservation of mass and momentum and energy as discussed in section 2.4.2 is as follows:

- Division of the domain into discrete control volumes using a computational grid.
- Integration of the governing equations on the individual control volumes to construct algebraic equations for the ‘unknowns’ such as velocity, temperatures and pressure.
- Linearization of the discretized equations and solution of the resultant linear equations system to yield updated values of the dependant variables.

The first two points employ a similar discretization process (finite-volume), but the approach to linearize and solve the discretized equations depends on the solver that was chosen in Fluent which will be discussed in section 2.4.8.3

2.4.8.1 Computational Grid (Mesh)

This procedure is performed during the pre-processing stage when the solution domain is subdivided into a finite number of control volumes or computational cells. The largest advantage of the finite volume method when compared to the finite difference method is

its independence of a structured grid. Therefore it enjoys frequent application especially if the grid is coarse and non-uniform.

The finite volume method locates the conserved variables within the volume element as depicted in Figure 2.6. For this reason it is desired to obtain a solution grid with efficiently structured elements. A structured grid, consisting mainly of hexahedral elements, is preferred to an unstructured grid, which mainly contains tetrahedral mesh elements or a hybrid structure. A structural hexahedral grid is renowned to yield more accurate flow-filed solutions. Tetrahedral grids are more susceptible to numerical diffusion, i.e. false diffusion being calculated that has the effect of increasing the real diffusion coefficient. Hexahedral mesh allows a greater chance for the flow to be aligned with the grid, which is not possible with a tetrahedral mesh, thus limiting the occurrence of numerical diffusion.

Tetrahedral grids also require approximately double the storage space and CPU time than hexahedral meshes having the same distribution of vertices (due to increased number of edges). Another advantage of hexahedral elements is its ability to be repeatedly subdivided anisotropically (directional dependence of a property) without the deterioration of the element quality.

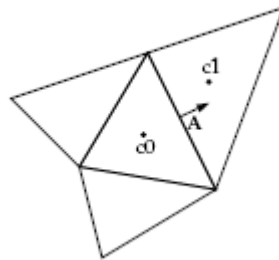


Figure 2.6: Depicting discretization of scalar transport properties by the finite volume method.

2.4.8.2 Discretization of the governing transport equations

Discretization of the governing equations is the second step in the solution algorithm of the finite volume method. During this step the governing transport equations are integrated over each control volume or computational cell for a discrete time interval:

$$\oint \rho \phi \vec{v} \cdot d\vec{A} = \oint \Gamma_{\phi} \nabla \phi \cdot d\vec{A} + \int_{\nu} S_{\phi} dV \quad (2.55)$$

When solving is initiated within the Fluent interface, the above equation is applied to each control volume within the solution domain. When applying discretion on a computational cell, the following typical equation will result:

$$\sum_f^{N_{faces}} \rho_f \vec{v}_f \phi_f \cdot \vec{A}_f = \sum_f^{N_{faces}} \Gamma_\phi (\nabla \phi)_n \cdot \vec{A}_f + S_\phi V \quad (2.56)$$

This equation is the general form for all the equations solved by Fluent.

When the values from the neighbouring cells are required for computation, interpolation of the cell centre values are required. An upwind scheme, which derives quantities from cells upstream, is used for this purpose. Various upwind schemes are provided by Fluent, of which the first and the second order schemes are the most important.

The first order scheme assumes the cell-centre values represent the cell-averaged value which holds throughout the entire cell; therefore the face quantities are identical to the cell quantities. The second order scheme computes the quantities at the cell faces by applying a multidimensional linear reconstruction approach. This method involves a Taylor series expansion of the cell-centered solution about the cell centroid. This method allows higher accuracy to be achieved and is essential when using a tetrahedral unstructured grid.

The gradient of a property in the upstream cell is computed by the following discrete form:

$$\nabla \phi = \frac{1}{V} \sum_f^{N_{faces}} \vec{\phi}_f \vec{A} \quad (2.57)$$

Where the face value for $\vec{\phi}_f$ is calculated by averaging ϕ from the two neighbouring cells to the face.

Other discretion schemes are also available, but won't be discussed here.

2.4.8.3 Solvers

FLUENT provides three different solver formulations:

- segregated
- coupled implicit
- coupled explicit

All three solver formulations will provide accurate results for a broad range of flows, but in some cases one formulation may perform better (i.e., yield a solution more quickly) than the others. The segregated and coupled approaches differ in the way that the continuity, momentum, and (where appropriate) energy and species equations are solved: the segregated solver solves these equations sequentially (i.e., segregated from one another), while the coupled solver solves them simultaneously (i.e., coupled together). Both formulations solve the equations for additional scalars (e.g., turbulence or radiation quantities) sequentially. The implicit and explicit coupled solvers differ in the way that they linearize the coupled equations.

The segregated solver traditionally has been used for incompressible and mildly compressible flows. The coupled approach, on the other hand, was originally designed for high-speed compressible flows. Both approaches are now applicable to a broad range of flows (from incompressible to highly compressible), but the origins of the coupled formulation may give it a performance advantage over the segregated solver for high-speed compressible flows. The coupled implicit solver is that it requires more memory (1.5 to 2 times) than the segregated solver.

2.4.8.4 Under relaxation

The equations being solved by Fluent are mostly non-linear. The need therefore arises to control the change in variable x by using under relaxation factors. Every iteration computes a new value of x from the old value (x_{old}) by adding a change factor Δx . This change can be controlled by using an under relaxation factor.

$$x = x_{old} + \alpha \Delta x \quad (2.58)$$

It is sometimes necessary to control these factors as too large under relaxation factors can lead to numerical instability.

2.5 Previous CFD models of a six-in-line furnace

Previous CFD models of a six-in-line furnace were developed by Gunnewiek and Tullis in 1996, Sheng, Irons and Tisdale in 1998 and the CSIR (Council for Scientific and Industrial Research) in South Africa on the Polokwane furnace which will also be used for this study. The models of Sheng *et al.* (1998b) and the CSIR are discussed. All the models, however, consist only of a slice of the furnace and no full model has been developed up to date due to the complexity of the problem as well as computer limitations and computing times.

2.5.1 Sheng, Irons and Tisdale 1998

These authors developed a three dimensional model of six-in-line 36 MVA capacity furnace for smelting nickel calcine operated by Falconbridge Limited. The slag was found to be thermally homogenized due to evolved gas and to a lesser extent by natural convection. The matte was thermally stratified and this was attributed to poor momentum transfer across the slag/matte interface. Ninety percent of the electrical energy was used in smelting reactions in the calcine.

The electrodes are immersed in the slag and the electrical energy is converted into heat by ohmic losses in the slag. The distribution of the generated heat is principally determined by the electrical field intensity distribution and the slag electrical conductivity. To obtain the heat distribution, Maxwell's equations for the electrical field intensity was solved along with the fluid flow and heat transfer equations.

2.5.1.1 Assumptions and formulation

Three major simplifications were made to the Maxwell's equations:

1. Only steady state solutions were sought; the alternating current was replaced with an equivalent direct current.
2. According to the magnetic Reynolds number, the charge carried by the fluid convection was neglected, as it was much less than the current due to potential gradients. This eliminated one source of coupling between the electromagnetic and fluid flow equations.
3. The electromagnetic force or the Lorentz force ($\mathbf{J} \times \mathbf{B}$) was found to be small compared to the bubble-driven and buoyancy forces and was therefore neglected.

Mathematical formulation

The transport equations were solved in three dimensions incorporating the buoyancy terms due to natural convection of the slag and the carbon monoxide bubbles in the vertical momentum equation. The CFD code PHOENICS was used.

Computational cell

The computational cell was chosen as the portion of the bath heated by half of an electrode. A 16 x 24 x 17 grid system was used incorporating a finer mesh near the boundaries of the fluid.

Boundary Conditions

Most of the boundary conditions took the conventional form and plant data was used to calculate federates and energy losses. The slag/matte interface was assumed to be motionless.

Electrode surfaces

The electrical potential on all the surfaces of the electrode was assumed to be uniform and equal to either the electrical potential applied to the electrode, V_e or the electrical potential experience by the slag, V_s . It was previously shown by the current authors that a significant electrical drop occurs at the electrode surface due to arcing to the gas. When the V_s was used as the boundary condition, the heat release due to arcing at the electrode surface was treated as an additional heat source evenly distributed in the first layer of the nodes around the electrode. It was assumed that there was no heat exchange between the electrode and the slag, so that the temperature gradients perpendicular to the walls were zero. For the flow field the non-slip-boundary condition was assumed.

Slag/calcine interface

No electrical current entered the calcine phase, because it was assumed to be electrically insulating. Therefore the vertical gradient of the electrical potential was zero at the interface, but the surface current flow along the interface was calculated once the electric potential field was available.

A heat balance, however, showed that 90% of the electrical energy supplied to the furnace was consumed in the smelting reactions and the heat flow into this zone is therefore very important. Utigard *et al.* (date unknown) according to Sheng *et al.* (1998b) classified the smelting zone as a region of semisolid oxysulphides, coke and calcine particles from which the molten slag and matte droplets fall. These reactions are strongly endothermic and cannot proceed without heat from the slag. There is thus a complex interplay between the rates of heat transfer, flow of reactants and products and chemical reactions to determine the thickness and structure of the smelting zone. At the authors present level of understanding it was not possible to model the smelting zone in detail and a heat flow to this zone was therefore empirically determined and used as boundary condition. Please see reference for the details.

The calcine/slag interface was used as a mass flow inlet to simulate the flow of fresh slag and matte in the bath and the rate was assumed to be uniform over the entire interface. A non-slip boundary condition was assumed for the horizontal component of slag velocity.

Slag/matte interface

It was found that a non-slip boundary condition was required to achieve a good agreement between the measured and computed temperature profiles. Two hypotheses were used to explain the immobile behaviour of the interface.

The first is that there is a balance between the surface shear forces and those due to surface tension gradients. The other hypothesis is that the interface is immobilized by the presence of a solid phase at the interface. Chromium may accumulate at the interface and may impede the motion of the interface.

Slag resistance

An empirical correlation for slag conductivity, proposed by Jiao and Themelis, was used. A conductivity that increases with temperature is inherently unstable. The equations used here show that more power are drawn if the temperature increases, leading to further increases in temperature. This instability caused the program to diverge and was therefore solved by under-relaxation of temperature changes and by limiting the conductivity to 60 mho/m.

Physical Properties

The following physical properties were used by Sheng *et al.* (1998)

Table 2.1: Physical properties of slag and matte at 1250 °C as used by Sheng *et al.* (1998)

Property	Symbol	Units	Slag	Matte
Density	ρ	kg/m ³	3200	4500
Coefficient of thermal expansion	B	K ⁻¹	2.70E-04	1.00E-04
Heat Capacities	Cp	J/kgK	1250	720
Viscosity	μ	Pa.s	0.3	0.05
Kinematic Viscosity	ν	m ² /s	9.38E-05	1.11E-05
Thermal conductivity	k	W/mK	8	17
Magnetic diffusivity	α	m ² /s	2.00E-06	5.25E-06
Prandtl Number	Pr		46.9	2.11
Electrical conductivity	σ	mho/m	30	93000

2.5.1.2 Model results

The electrical potential distribution derived in this paper can be seen in Figure 2.7. The corresponding volumetric heat release can be seen in Figure 2.8 and makes it clear that the heat release rate drops even more sharply away from the electrode than the electrical potential.

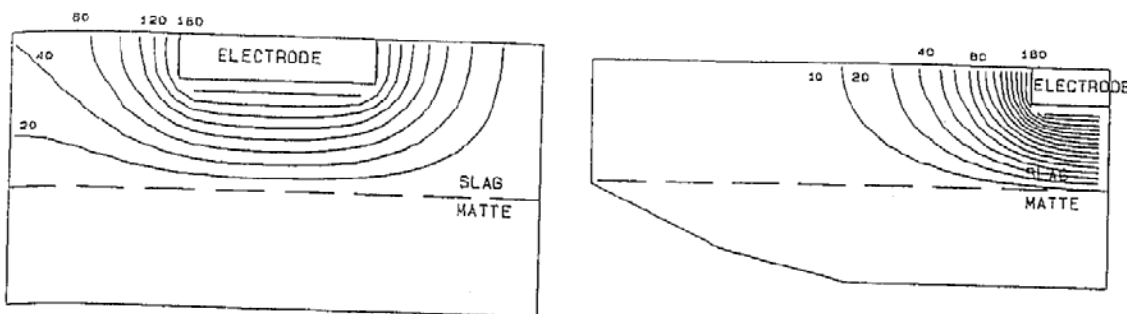


Figure 2.7: The electrical potential as calculated by Sheng *et al.* (1998b)

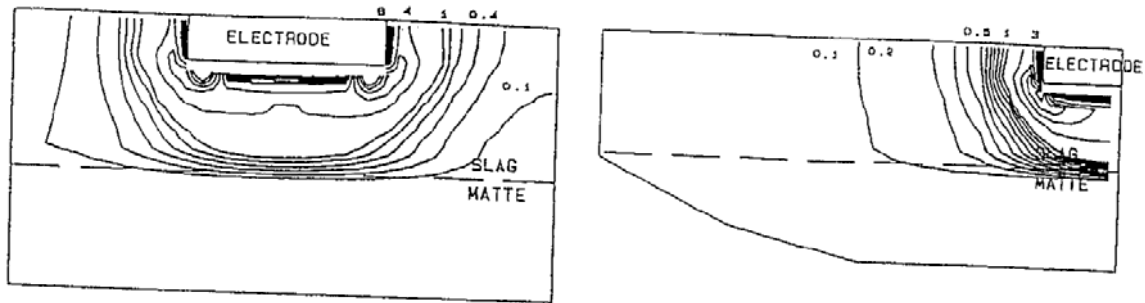


Figure 2.8: The volumetric heat release as calculated by *Sheng et al. (1998b)*

The calculated temperature profiles can be seen in Figure 2.9. The slag seems to be well mixed at a fairly constant temperature around 1230°C while the temperature in the matte decreases more rapidly towards the hearth area. When these data were validated however, it showed that the temperature in the matte is more uniform than the calculated data. Figure 2.10.

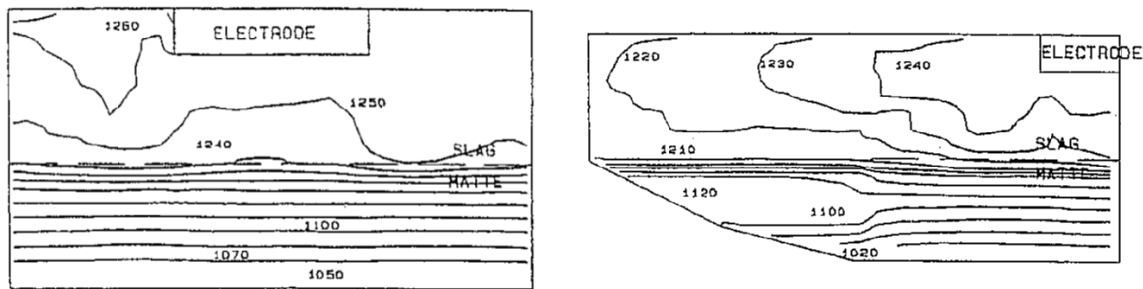


Figure 2.9: Temperature profile in the matte and slag as calculated by *Sheng et al. (1998b)*

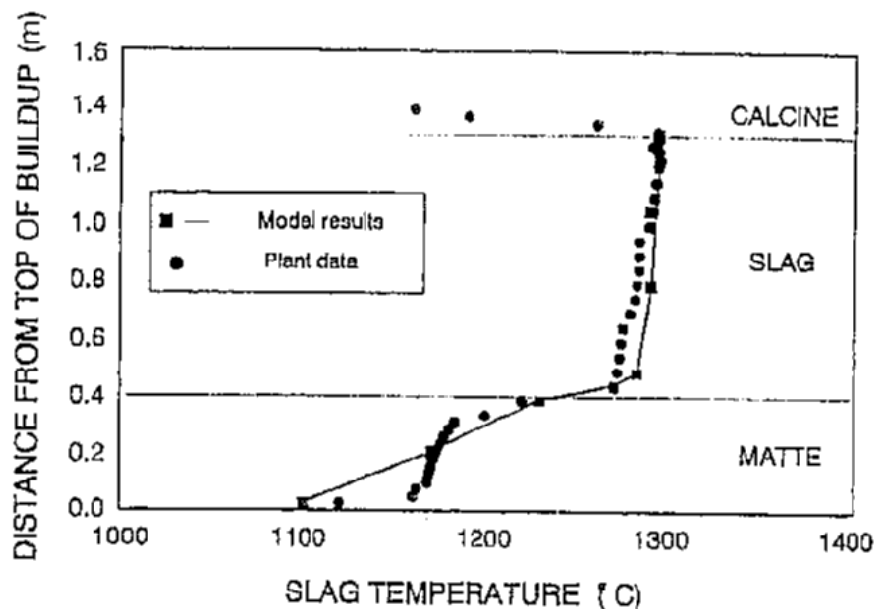


Figure 2.10: Comparison by Sheng *et al.* 1998b between measured and calculated data showing good comparison in the slag but a more uniform temperature in the matte.

The calculated flow velocities are in the region of 0.2 m/s and indicate a direction from the electrode outwards towards the slag wall. No movement in the matte however. Figure 2.11

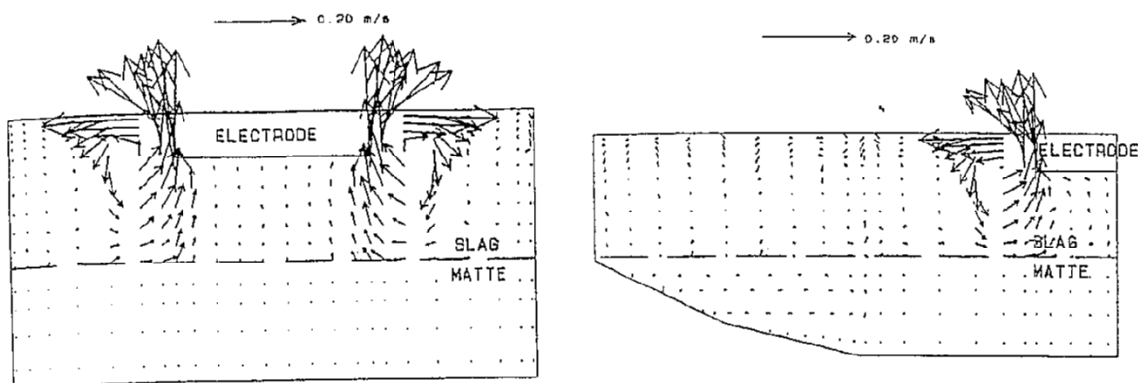


Figure 2.11: Slag velocity vectors as calculated by Sheng *et al.* (1998b)

It is interesting to note here that *Jardy et al.* calculated a different flow profile for a pilot plant on a circular furnace as indicated in Figure 2.12. They estimated that the velocity vectors around the electrode would be downwards as if a vortex had been created around the electrode surface right down to its tip. Contrary to this, visual observations by *Eric et*

al. on a 5MW circular three electrode matte smelting furnace indicated a boiling reaction around the electrodes which could hardly be conducive to downward flow directions.

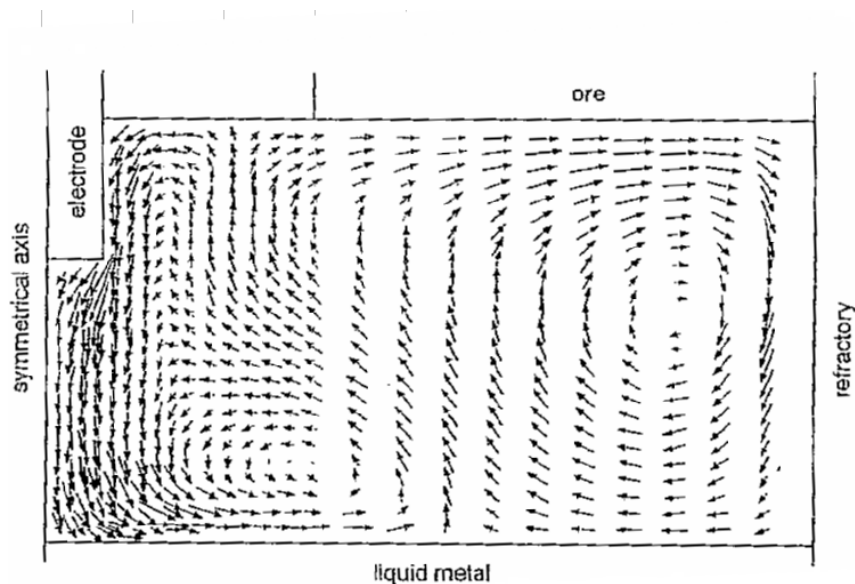


Figure 2.12: Computed velocity vectors in a circular furnace by *Jardy et al.* (as referenced by *Sheng et al 1998b*)

2.5.2 CSIR model of the Polokwane furnace

The CSIR (Council for Scientific and Industrial Research) was asked by Anglo Platinum to develop a model for the Polokwane furnace which is also the aim of this study. FLUENT was used as CFD code. Hadley *et al.* (2005). The furnace geometry as developed by the CSIR was used but the mesh was improved as well as most of the boundary conditions. It is believed by the author that the results showed in this study is a significant improvement on the results found by the CSIR (mainly due to more time spent on the research) and the results of the CSIR are therefore not discussed in this thesis. The main simplifications that were made in the CSIR study are discussed below:

Time dependence

The system was considered as a steady state operation with no variation in the operating parameters over time. This ignores the cyclic operation of the furnace with charging and tapping that occurs during normal operation.

Electric potential distribution

The flow of the molten material was neglected in the calculation of the electric potential distribution. Instead a simpler finite-element analysis of the current distribution and resulting joule heating was used to supply the location and magnitude of the joule heating for the CFD model.

Magneto-hydrodynamic effects

After a calculation of the magnetic fluxes around the furnaces, and found to be small, it was assumed that the stirring effect due to electromagnetic forces is negligible compared to the buoyant effect of the slag and was therefore not included in the model.

Domain

The present study focused on the activity in the vicinity of the electrodes where the heat is generated in the furnace. To facilitate a gradual increase in model complexity, the smallest representative modelling unit was chosen to reduce the size and runtime of the computations. As a result the area around a single electrode was isolated and further reduced, using symmetry, to include a quarter of the electrode and surrounding furnace geometry. Initial calculations included the freeboard and roof of the furnace – however the steady state assumption with no air flow modelled in the freeboard resulted in a very high temperature gas pocket developing on top of the concentrate. Although this could be addressed by adding source terms to extract the heat, a simpler solution was to further reduce the geometry by only modelling the lower half of the furnace, with the cut being made at the top of the air/concentrate interface. The details of the inner surface of the copper cooler (the hexagonal protrusions) were not included in the CFD. Instead, the surface was modelled as a smooth wall.

Material flow

The flow of material through the furnace forms an integral part of the operation, but requires inclusion of the chemistry of the melting and subsequent slag-matte separation process. This implies modelling a system with at least 5 materials (air, concentrate, mush, slag and matte) and inclusion of phase changes for some of the materials – although theoretically possible, validation would be required before such a simulation would yield acceptable results. The assumption of treating the furnace as a steady state process further complicates inclusion of material flows, which is by default a dynamic process. In

general the flow velocities associated with smelting and tapping are very small (of the order of mm/s) and should not affect the buoyant flow significantly.

Furnace chemistry

The chemical reactions occurring during heating the concentrate were ignored. The thermodynamic analysis showed that the energy consumed by chemical reactions is only about 1% of the total energy used.

Furnace surroundings

Furnace heat is lost to the surrounding environment through convection and radiation from the external surfaces, through the copper coolers and through off-gas. A CFD model including the space around the furnace would again become very large and the solution times excessive. Therefore all external surfaces were allowed to exchange heat with the surroundings through combined convection and radiation.

Electrical input power

The smelting process consumes between 70 and 80% of the total electrical power injected into the furnace. Heat losses to the copper coolers, the off-gas stream, electrode baking and through the walls to the surroundings consume the rest of the power. In this study the process chemistry was not included in the CFD model and as a result the energy associated with the chemical processes cannot be added to the simulation. Following Henning et al the heat generation was reduced to that lost to the surroundings and the copper cooler – this was varied between 8% and 14% of operating power to investigate the effects.

Slag/matte

Only the slag was modelled as a liquid, the matte was considered to be stationary. When modelled as a circulating liquid, the program was unstable and convergence couldn't be reached. The flow of slag is driven by density differences which result from temperature gradients in the material.

Concentrate/slag interface

The 'mushy' layer was modelled by fixing the temperature in this zone and secondly assuming a constant electrical conductivity into this zone.

2.6 Literature review summary

As this project was started with no prior knowledge of CFD techniques and equations, a literature review was done on CFD principles to be able to do the required modelling work. It is, however, necessary to understand furnaces first and this overview is therefore given first.

This literature review contains therefore the background information on furnaces from where the review focusses on immersed electrode operation (as with the Polokwane furnace) in section 2.1.2 to 2.2. It also contains the literature data on all the material properties (section 2.3) that is needed as model inputs and also how they will be used in the CFD equations (CFD – section 2.4.2).

Lastly after a good knowledge of how furnaces works as well as the material properties relating to this furnace and a understanding of how CFD calculates results was obtained, a review was done on all similar work completed in the past to learn from it, as well as to improve on it.

Chapter 3

MODEL SET-UP

In order to establish a suitable computational domain, it is important to have a good understanding of the system that is being modelled. As stated previously, only a section of the furnace has been modelled before due to complexity and computational limits and it will therefore also be the starting point for this study.

3.1 Creating the solution domain

The creation of the solution domain requires mainly three steps: creating the model geometry and identifying the different sections and dividing that specific domain into computational cells (grid) otherwise referred to as meshing.

3.1.1 The furnace slice

The slice that will be modelled was developed by starting from a complete furnace model as shown in Figure 3.1. The normal operating condition is a delta (Δ) connection, with two electrodes per phase resulting in three electrode pairs to introduce the electricity to the furnace.

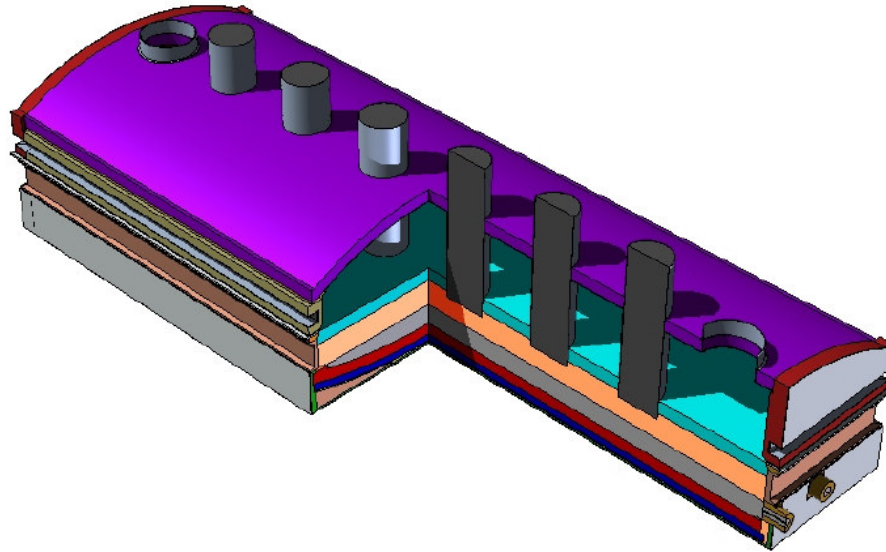


Figure 3.1: The complete furnace showing the 6 electrodes, off gas ports, hearth, sidewall, end walls, roof, matte tapping holes, matte, slag and concentrate layers. (CAD model by the CSIR)

A quarter of the electrode extending towards the sidewall of the furnace and the middle point between electrodes was chosen as the furnace slice to be modelled.

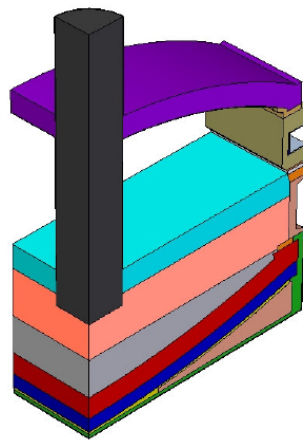


Figure 3.2: A quarter of an electrode starting towards the middle point between electrodes and the furnace sidewall.

As the focus is mainly on the heat transfer and flow in the matte and the slag, Figure 3.2, was further reduced to only contain the concentrate, matte and slag layers, furnace hearth and a section of the sidewall which will include the copper cooler, plate cooler and sidewall cooling section. The freeboard, roof and the electrode were not included. See Figure 3.3.

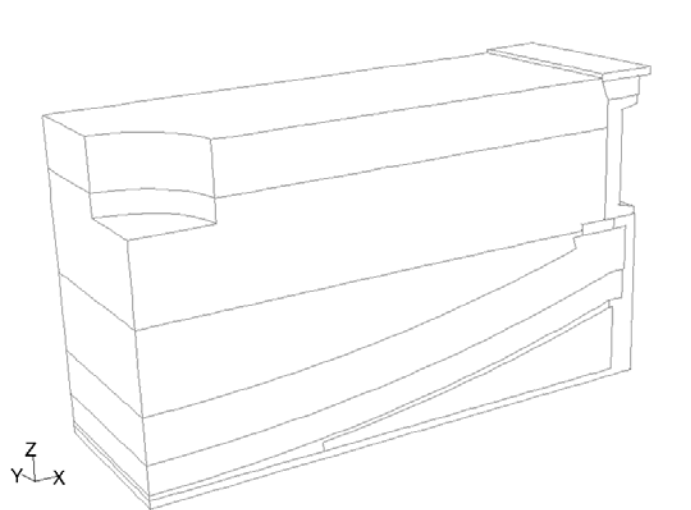


Figure 3.3: The furnace slice to be modelled containing only the concentrate, slag and matte layers, the furnace hearth and a section of the sidewall.

The approach for modelling the electrical input to the furnace that will be taken in this study is to make use of the Magneto Hydrodynamic Model of Fluent which will require two electrodes or an electrode pair to be included in the modelling domain so that an electrical flow path can be calculated through-out the domain. The slice in Figure 3.3 was therefore expanded to include the halves of two electrodes as shown in Figure 3.4. The yellow lines indicate where symmetry boundaries exist.

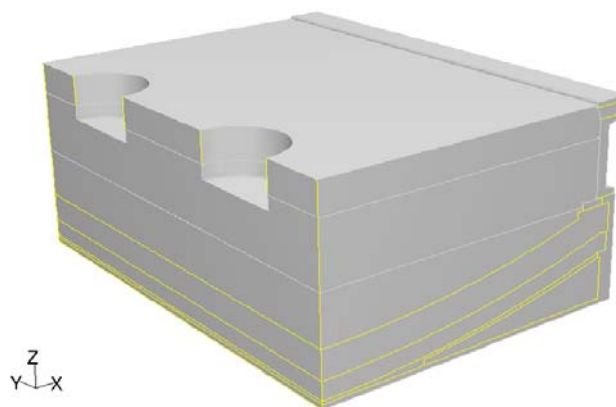


Figure 3.4: The furnace slice with the electrode pair to be used as computational domain. The yellow lines indicate symmetry boundaries.

The shape of the electrodes was modelled as a cylinder without any tapering or rounding of the edges. Figure 3.5 show the shape of the electrode tips during a shutdown also indicating a very flat bottom surface with a little bit of rounding around the edges. This

type of electrode tip shape is usually an indication of shallow immersion depths. The slice was modelled at 20% immersion depth into the slag.



Figure 3.5: The shape of the electrode tips indicated shallow immersion depths corresponding to the shape of the electrode tips in the model.

3.1.2 Model zones

The model is divided into different regions or zones to which a specific material needs to be assigned and indicated whether it is a solid or a liquid zone. Figure a in the appendix indicates the furnace materials

Figure 3.6 was used to assign all the zones in the model.

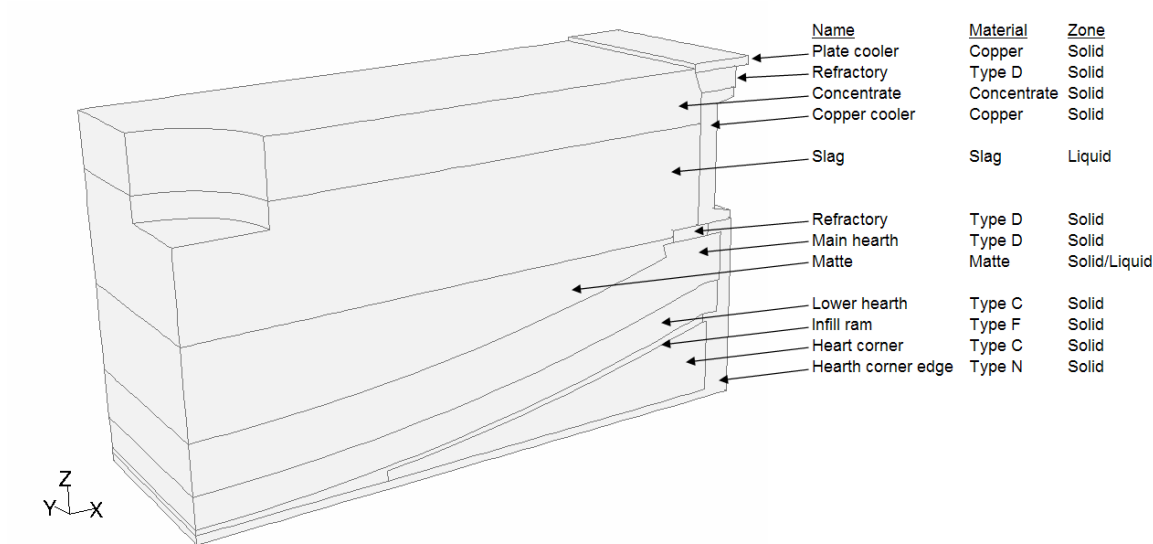


Figure 3.6: The different furnace regions/zones assigned with a specific material and modelled as either a liquid or a solid zone.

The material properties can be seen in the appendix.

3.1.2.1 Level Measurements

Level measurements or soundings are taken on an hourly basis by lowering a steel rod into the bath to determine the slag, concentrate and matte depths. The following depths were assumed for the model:

- Concentrate: 500 mm
- Slag: 1000 mm
- Matte: 720 mm

3.1.3 Meshing the computational domain

3.1.3.1 Creating the grid

The meshing of the model domain was done with *Gambit 2.3.16*. (Figure 3.8 to 3.10) A cooper mesh scheme was used through-out the entire modelling domain with difference in the face meshing of the top of the concentrate where a pave-scheme was used, coopered in the negative Z-directions and the corner section of the furnace where a T-grid face mesh was used and coopered in the Y-direction. The interface between the slag and the concentrate layer shows a very fine mesh, which is very important, as a very steep

temperature gradient occurs here and the user-defined function, that was developed to compensate for heat-up and melting of concentrate, uses cell values to calculate heat-losses. A coarser grid here therefore influences the total energy balances of the model dramatically. Please refer to section 4.2.1 for more detail. The coarser mesh in the matte area is acceptable as a very uniform temperature occurs in the matte due to its high thermal conductivity. The total number of cells are 218 648.

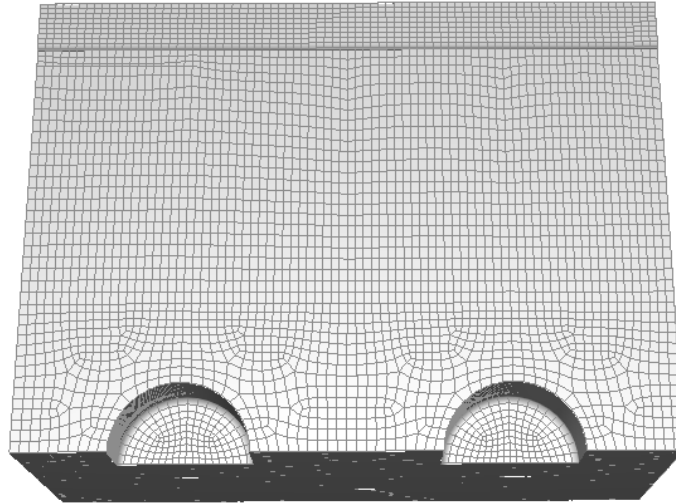


Figure 3.8: Pave meshing scheme coopered downwards

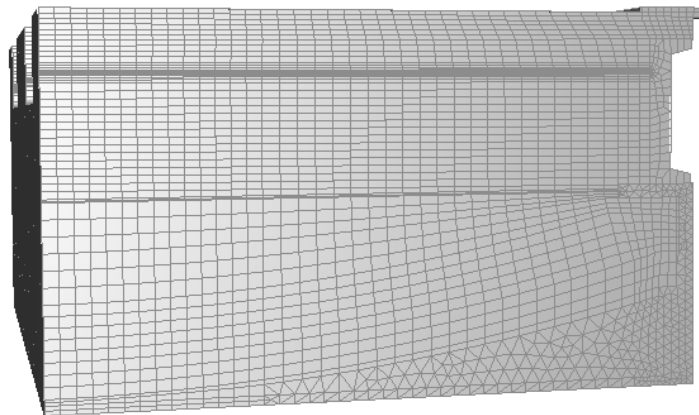


Figure 3.9: T-grid mesh in the bottom right corner coopered along the length of the slice and a course mesh in the matte area where the temperature is more uniform with fine mesh between the slag and the matte.

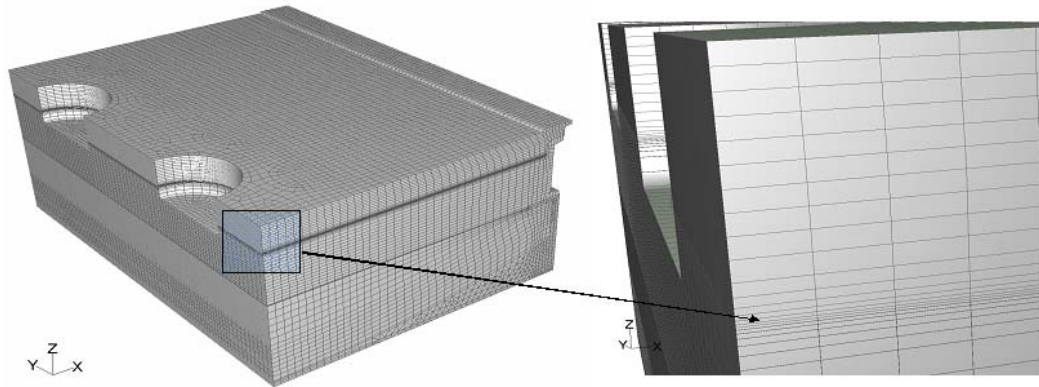


Figure 3.10: Model mesh showing a fine grid at the concentrate/slag interface where steep temperature gradients occur.

3.1.3.2 Mesh quality

The quality of the mesh plays a significant role in the accuracy and stability of the numerical computation. The shape of the cell has a significant impact on the accuracy of the numerical solution. The skewness is defined as the difference between the shape of the cell and the shape of an equilateral cell of equivalent volume. Highly skewed cells can decrease accuracy and destabilize the solution.

The aspect ratio is a measure of the stretching of the cell. If a simple geometry is used, where the flow conforms to the shape of the geometry, a mesh with cells of high aspect ratios is likely to have far fewer cells with accurate results, than if triangular/tetrahedral cells are used as in this case.

The mesh quality distribution is depicted in Figure 3.11 showing that the majority of the mesh elements (85%) are below an equiangle skew value of 0.2.

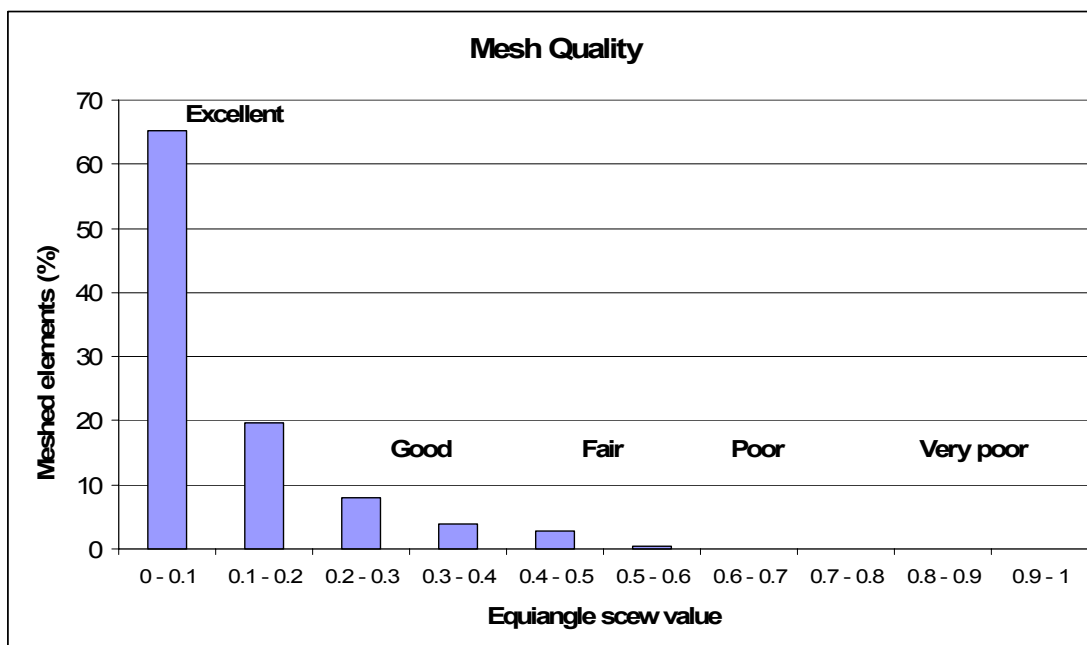


Figure 3.11: Mesh quality distribution showing that 85% of the meshed elements to be in the excellent region indicating a very high quality mesh.

3.2 Model set-up and approach

A systematic approach was taken in setting up the model. The energy was divided into energy generation and energy sinks and each was treated and will be discussed separately.

Accounting for the energy is the main focus of this research, but it is also a necessity to ensure that the CFD model is properly converged. Although no formal validation of the results has taken place, there are constantly being referred back to plant data to ensure that the model is representative of the particular operation.

3.2.1 Energy Generation

Fluent's *Magnetohydrodynamics Model 2.1* was used to model the energy input or electrical charge. The resistance of current flow through the furnace bath is converted to Joule heating according to the equation:

$$P_E = I^2 R_{bath} \quad (2.1)$$

This relationship is also used to model the energy input to the model. The current density at the electrode tips is calculated by dividing the measured current flow through the electrodes by the area of the electrodes that are immersed into the slag. This value is then used as boundary condition at the electrode/slag interface and the current flow through the model is solved.

The electrical conductivity is the second term that determines the energy input to the model. Table 3.1 gives an indication of the values used for the electrical conductivity of the matte, slag and concentrate:

Table 3.1: Bath conductivities (S/m or 1/ohm-m)

Material	Conductivity
Slag	16.7 - 76.2 depending on temperature*
Matte	93000
Concentrate	1.2

*The electrical conductivity of the slag will increase as the temperature of the slag increases, Hundermark (2003). A constant slag composition is assumed.

Although the electrical conductivity of the slag is temperature dependent, a constant value is used for the power input. This will prevent the energy input to fluctuate as the slag temperature changes with the iterations. With this method the energy input can be controlled to the model to a point where it compares with operations.

Furnace power is controlled in a similar manner with the immersion depth of the electrodes. The resistance increases as the electrode tip is moved upwards from the slag metal interface to the slag surface. This simple resistance to immersion depth relationship provides the basis for regulating the furnace power. The transformer secondary voltage tap is set at the desired value and the electrodes are raised or lowered to maintain the set point resistance or impedance. Control of load resistance essentially controls furnace power through the relationship:

$$P_E = \left(\frac{V \cdot PF^2}{R_{bath}} \right) \quad (2.2)$$

P_E = Electrode power

V = Voltage

PF = Power factor

R_{bath} = Bath resistance per electrode

For the model, however, the immersion depth is fixed and the electrical conductivity (resistance or impedance) needs to be adjusted to control the power input.

Two sets of results can now be obtained and compared with furnace data:

- The electrode tip voltage (Figure 3.12a)
- The total power generated (Figure 3.12b)

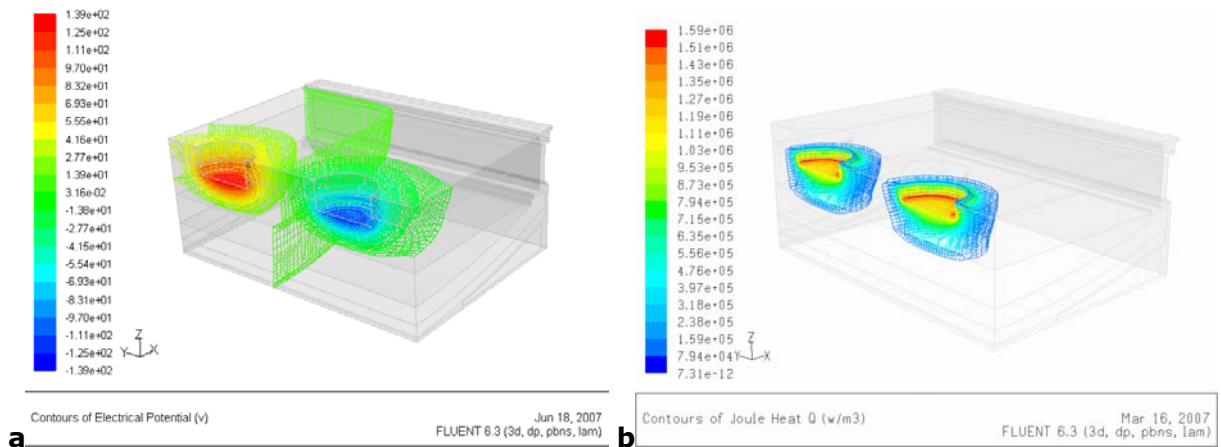


Figure 3.12: Results for energy input: a) Electrode tip voltage and b) the joule heating generated in the bath.

Sheng *et al.* (1998a) found that there is a substantial voltage drop at the electrode interface, 100 to 120V for applied potentials of 180 to 230 V for the Falconbridge furnace. This potential drop was attributed to the creation of an arc from the carbon monoxide evolved at the electrodes due to chemical erosion. A similar trend is observed here where the voltage at the electrode tips is significantly less than the measured value at the contact clamps in the furnace. This voltage drop should therefore also be taken into account when the model energy input is compared with furnace power, as this voltage drop is not included in the model, only the heat generation through joule heating.

3.2.2 Energy sinks

The energy sinks that were taken into consideration are the energy associated with the heat-up and melting of concentrate, the heat-up of slag and matte particles after melting, the shell losses and the reactions occurring around the electrode.

3.2.2.1 Concentrate heat-up and melting

Sheng *et al.* (1998b) reported the smelting zone to be a complex interplay between heat transfer, flow of reactants and products and chemical and melting reactions. An empirical heat transfer equation was used to account for the heat transfer in the concentrate.

In the present study, a user defined function in C++ was developed to account for the energy associated with the concentrate heat-up and melting. The energy sink is defined as:

$$Q_{conc} = C_{p_{conc}} \rho_{conc} T_{RG[z]} v_{conc} \quad (3.1)$$

The bulk density of concentrate is used for the density term in equation 3.1 and is assumed to be a constant value. It is expected here that the density of the concentrate will change as the temperature rises and a semisolid to liquid zone develops. At the present level of understanding, it was, however, not possible to incorporate these density changes.

The $T_{RG[z]}$ term is the reduced temperature gradient in the Z-direction in the concentrate. This means that the top of the concentrate should be at lower temperature than at the concentrate/slag interface for the heat-sink to be accounted for in the calculations. A larger temperature gradient means a larger heat-sink or more energy for heat-up and melting purposes.

The v_{conc} is the speed of the concentrate moving down, which is calculated from the feed rate of concentrate to the furnace at a certain power setting. It is assumed that the smelting rate or speed of concentrate moving down is uniform across the furnace. Although this is a rather gross assumption, it was deemed more important by the authors to specify the size of the energy sink, than to determine the location. This value can, however, be adjusted according to space and temperature to allow for faster melting around the electrodes. Faster melting will occur here, because all the heat is generated in the vicinity of the electrodes. Visual observations of the furnace operations confirm that the concentrate is consumed faster around the electrodes as the layer of concentrate on top of the slag will burn away quicker.

Factsage was used to determine the enthalpy change of concentrate as it heats-up together with the heat consumed in melting reactions. (Figure 3.13) The latter is not a vertical line due to the various different components melting at different temperatures.

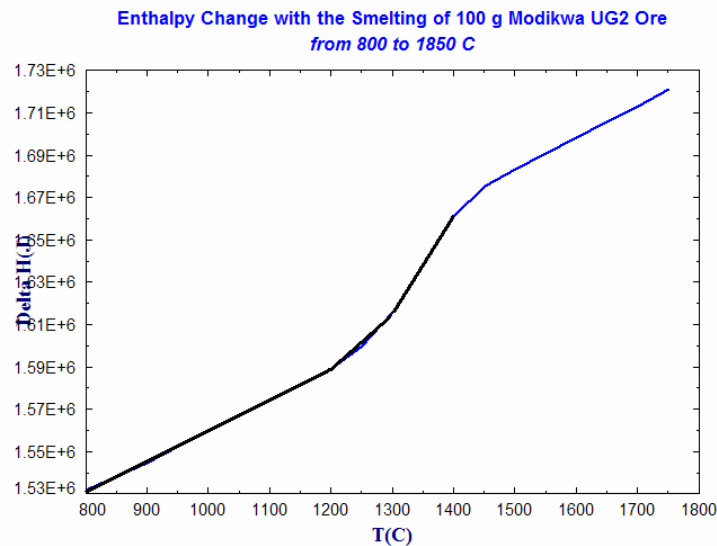


Figure 3.13: Factsage heat-up and melting profile of concentrate. By dividing the curve in constant gradients, effective Cp_conc values can be calculated.

An effective Cp_conc can now be calculated from the gradient of the enthalpy curve which will take the heat required for melting into account (Figure 3.14). Scheepers *et al.* (2006) According to thermodynamics the Cp of a material is not affected by melting. The enthalpy associated with the melting is only a vertical jump on the enthalpy graph at a specific temperature. If constant heat sinks at specific temperatures, to compensate for the melting reactions, are introduced at specific temperatures or points in the model, it results in negative temperatures at the localized points where the large heat sinks were introduced.

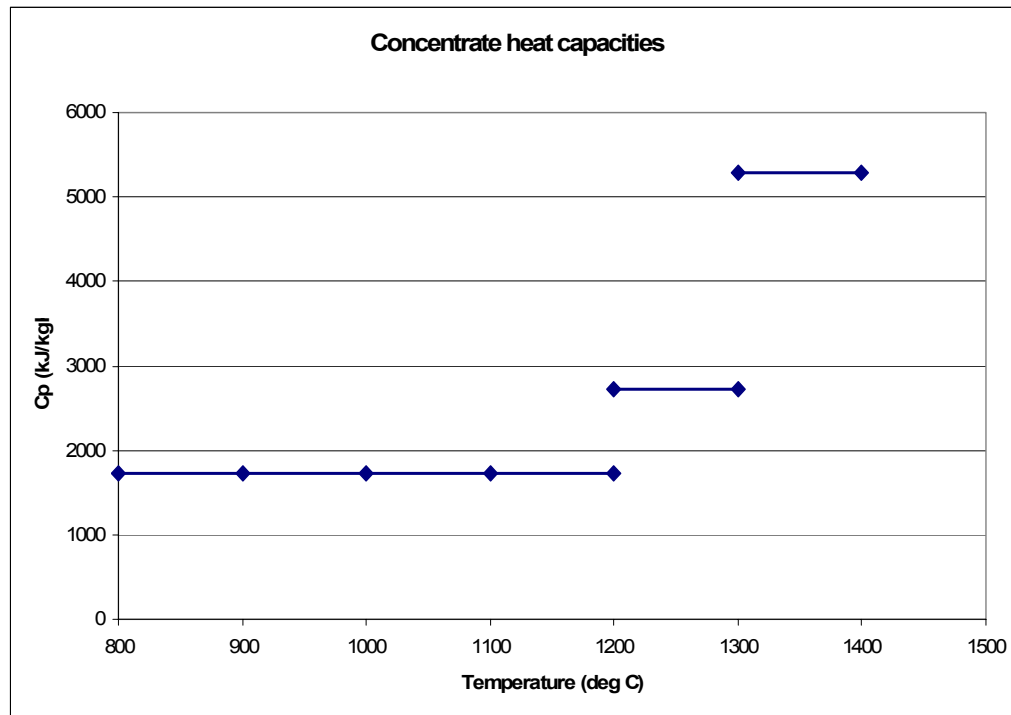


Figure 3.14: Effective Cp_conc values calculated from the gradients of the enthalpy vs temperature curve. The higher Cp values compensate for energy required for melting reactions

The heat-sink as calculated by equation 3.1 is therefore larger with higher temperature gradients in the concentrate and in the region where phase changes (melting) take place (at temperatures where the cp's are higher). The latter is expected to occur around the slag interface and the results indicate just this as shown in Figure 3.15.

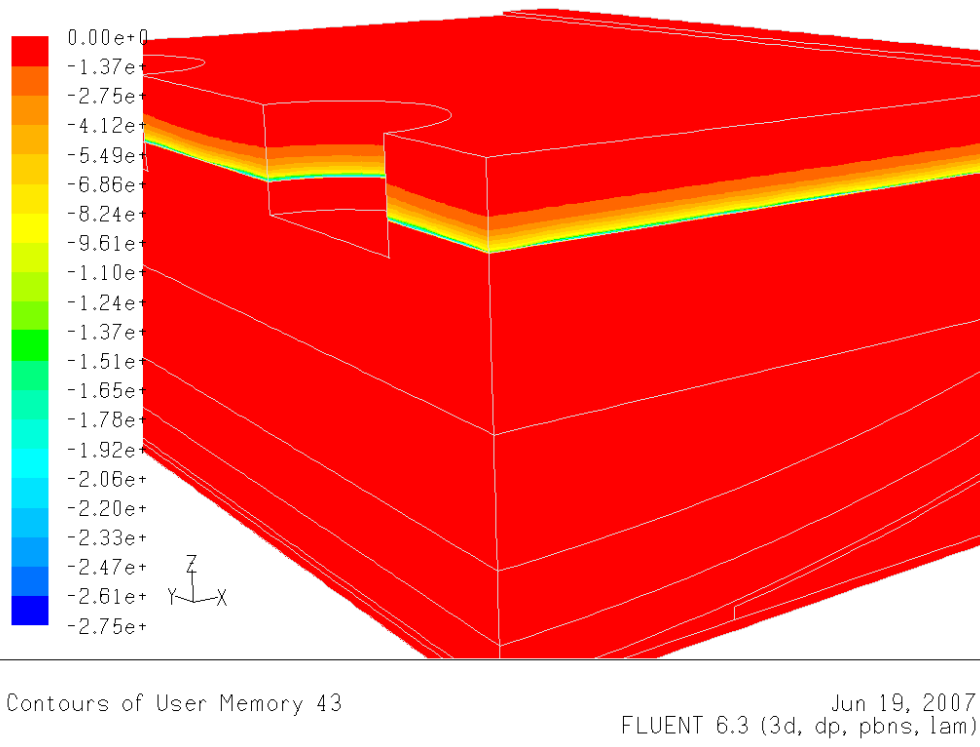


Figure 3.15: The heat-sink in the concentrate compensating for the energy due to the heat-up and melting of concentrate. Melting mainly occurring at the slag/concentrate interface

3.2.2.2 Slag and matte heat-up

The second energy sink is introduced, because the furnace bath temperature is operated at a significantly higher temperature than where the concentrate melts and separates into slag and matte particles. All new matte and slag particles require thus some energy to get to the operating temperature. A user defined function was written for this purpose and is defined as:

$$Q_{slag} = \frac{m_{slag} C_{p,slag} (T_{avg} - T_{melt})}{V_{slag}} \quad (3.2)$$

The ' m_{slag} ' term is the mass flow rate of slag and matte which corresponds to the feed rate of concentrate. It is assumed here that all the matte particles will heat-up with the slag as it falls through the slag and there is therefore not a heat-sink for matte in the matte area.

The average temperature ' T_{avg} ' in the slag area is calculated with every iteration and the energy sink therefore grows as the slag temperature increases. The ' T_{melt} ' term is the temperature in the first row of cells of the slag area at the slag/concentrate interface.

Equation 3.2 results in a uniform energy sink over the entire slag area as can be seen in Figure 3.16. This assumption corresponds to the assumption of a uniform melting rate of the concentrate. The size of the energy sink was deemed more important at this stage of the project than where it occurs.

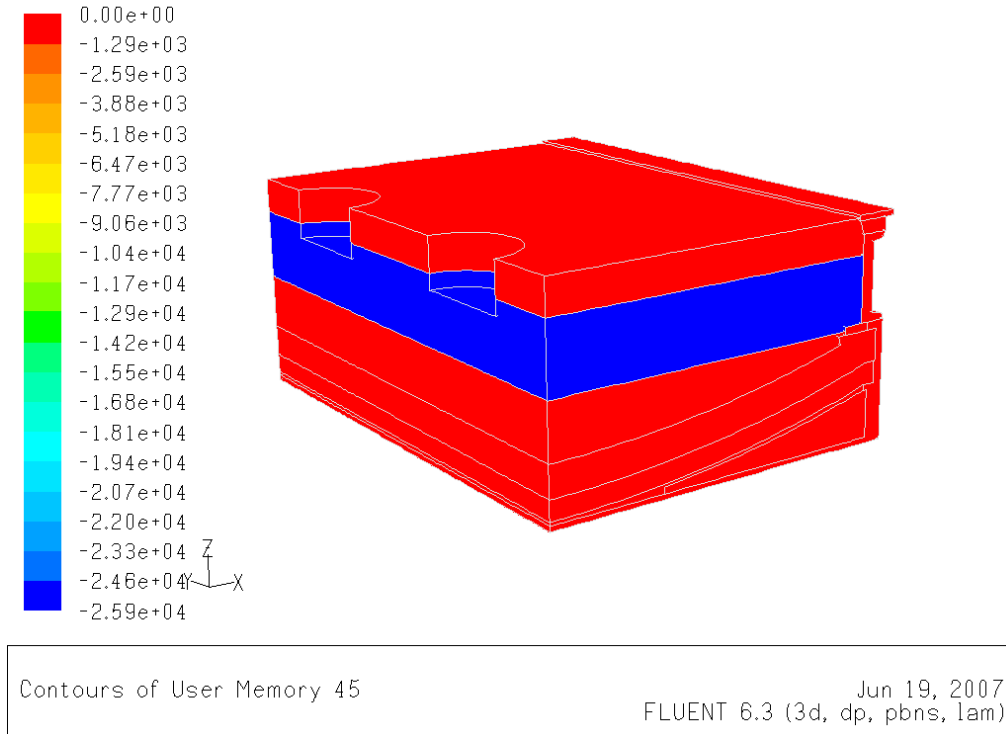


Figure 3.16: Energy sink due to the heat-up of slag and matte from melting temperature to bath/operating temperature. The energy sink is assumed to be uniform over the slag area.

3.2.2.3 Shell losses

The boundary conditions used to calculate the shell losses are mainly with fixed temperature wall boundaries and combined convection and radiation wall boundaries.

Table 3.2: The values specified at the boundaries for the computing of the shell losses. *Data from Hadley *et al.* (2005)

	Fixed	Combined convection and		
	Temperature	radiation		
	°C	h (W/m ² K)	ε (emissivity)	T _∞ (°C)
Copper cooler	45*			
Plate cooler	45*			
hearth cooling		8	0.85*	40
sidewall cooling		87	0.85*	30
conc to freeboard		0.5*	1*	500

The heat transfer rate for the combined convection and radiation wall boundary condition is calculated with:

$$q = h(T_{wall} - T_{\infty}) + \varepsilon\sigma(T_{wall}^4 - T_{\infty}^4) \quad (3.3)$$

Forced draught fans are used for air cooling the hearth, sidewalls and end wall matte zones. The forced convection coefficient is calculated from the Nusselt number:

$$h = \frac{Nu_L k}{L} \quad (3.4)$$

The Nusselt number is calculated using the equation for turbulent flow over a flat plate. Incropera and DeWitt (1996). The Nusselt number was calculated at three different points along the length of the furnace for the hearth and the sidewalls and the variation in the convection coefficient for both the hearth and the sidewalls was found to be small. The average of the calculated convection coefficients was therefore used.

$$Nu_L = 0.0296 Re^{\frac{4}{5}} Pr^{\frac{1}{3}} \quad (3.5)$$

3.2.2.4 Reactions around the electrode

With the high current densities at the tip of the electrode, extreme localised heating occurs, that leads to an increase in the rate of reaction between the carbon electrode and the slag, resulting in gaseous products (CO and SiO) The energy associated with the

endothermic reaction of Carbon dioxide with carbon at the electrodes has been found to be negligible and therefore not considered as a heat sink. The rate of CO release at the electrodes has been calculated from the paste consumption figures obtained from plant data at Polokwane Smelter according to reaction 1.



The bubble formation around the electrode causing a stirring effect in the slag has been simulated using the *discrete phase* model technique of Fluent based on Lagrangian modelling whereby CO bubbles are released at the surface of the electrode at low velocities at the same temperature as the slag bath and allowed to drift upwards causing a stirring effect by dragging slag particles along. Figure 3.17 It was assumed that the bubble size is about 20mm according to the voltage drop associated at the electrodes and that these bubbles retain their shape and size as they drift towards the concentrate/slag interface.

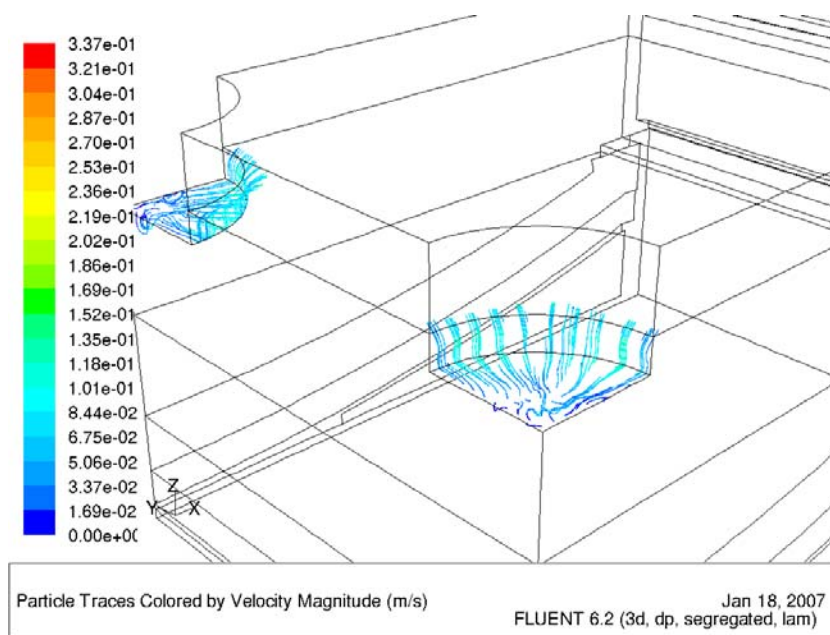


Figure 3.17: CO bubbles being released at the electrode surface causing a stirring effect in the slag.

Chapter 4

RESULTS AND DISCUSSION OF RESULTS

4.1 Electrode current

The current density profiles between the two electrodes were clearly found to be three dimensional as indicated by Figures 4.1 and 4.2. Even though the electrodes are only 20% immersed in the slag, the current profiles are computed to be mostly through the matte with the current path being downwards from the electrode, through the matte and up towards the second electrode as indicated by the current vectors shown in Figure 1 b.

Two dimensional views of the current density are shown in Figure 4.2. Cut A can be compared to Figure 2.3 in section 2.1.2 of the literature review showing the current to flow mainly through the matte. Cut B, C and D also accentuate the difference between the matte and the slag layers. The current in the slag drops to zero very quickly from the electrode towards the wall in a concentric circle formation while in the matte, however, the majority of the current is shown to be in the centre of the two electrodes and gradually drops towards the side wall with current running between 0 and 5320 A/m² at the side wall. It is according to the authors knowledge the only study indicating the current flow profiles in a three dimensional scale in the slag and the matte.

Now the electromagnetic force or the Lorentz force, ($J \times B$) was demonstrated by Choudhary and Szekely to be negligible in comparison to natural convection and bubble stirring for large scale furnaces. While this may be true for the slag, it may not necessarily be true for the matte as well, due to the large amount of current flowing through the matte. This phenomena is, however, not included in this study because, similar to Sheng *et al.* (1998b), only an equivalent DC current flow is assumed, but it is recommended for future research.

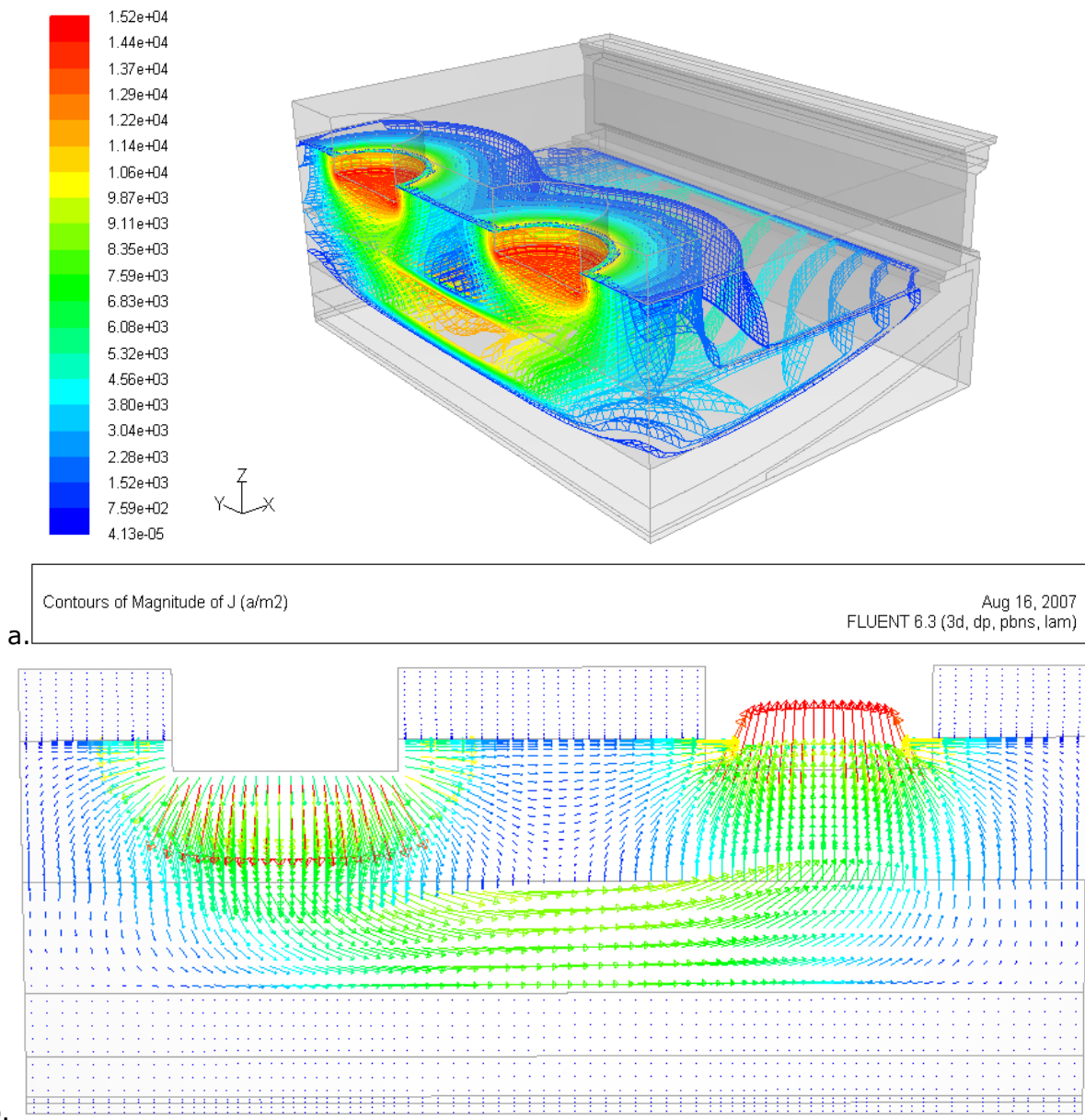


Figure 4.1: a. Three dimensional view of the current density profiles through the furnace slice indicating the majority of the current flowing through the matte layer and b) the current density vectors depicting the direction of the largest current density vectors to be vertical in the slag in horizontal or through the matte.

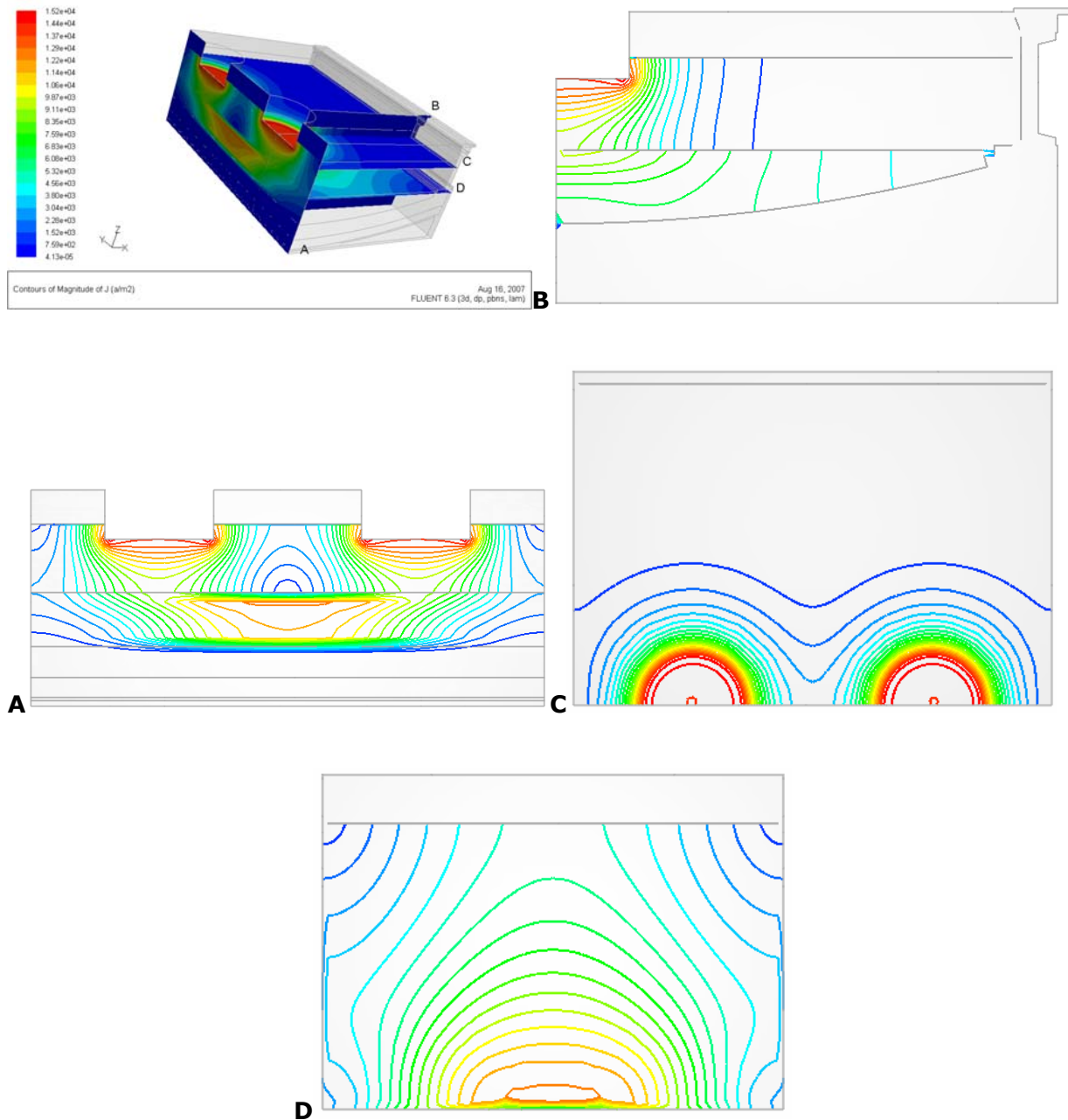


Figure 4.2: Two dimensional current density profiles through certain plains of the furnace slice. A – Cut through the centre of both electrodes along the length of the furnace. B - Cut through the middle of one electrode towards the sidewalls showing the arc of the hearth. C – Cut through the slag parallel to the slag/concentrate interface at the bottom the electrode tip. D – Cut just below the matte/slag interface parallel to the interface.

4.2 Electrode potential and Power Distribution

For the voltage profiles, an excellent agreement is obtained with the published data of Sheng, Irons and Tisdale (1998b).

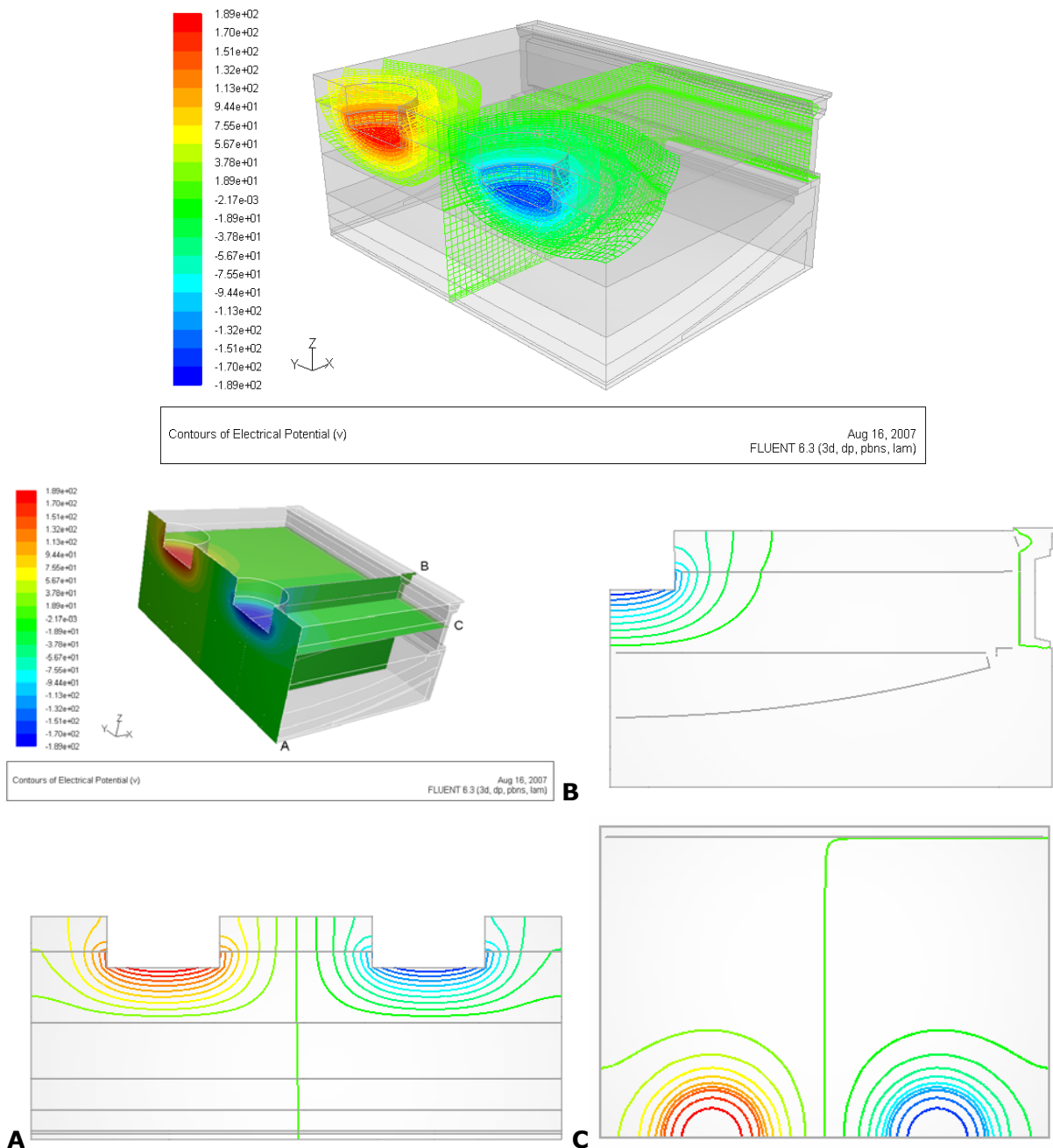


Figure 4.3: A three dimensional view as well as the two dimensional voltage profiles through certain plains of the furnace slice. A – Cut through the centre of both electrodes along the length of the furnace. B - Cut through the middle of one electrode towards the sidewalls showing the arc of the hearth. C – Cut through the slag parallel to the slag/concentrate interface at the bottom the electrode tip.

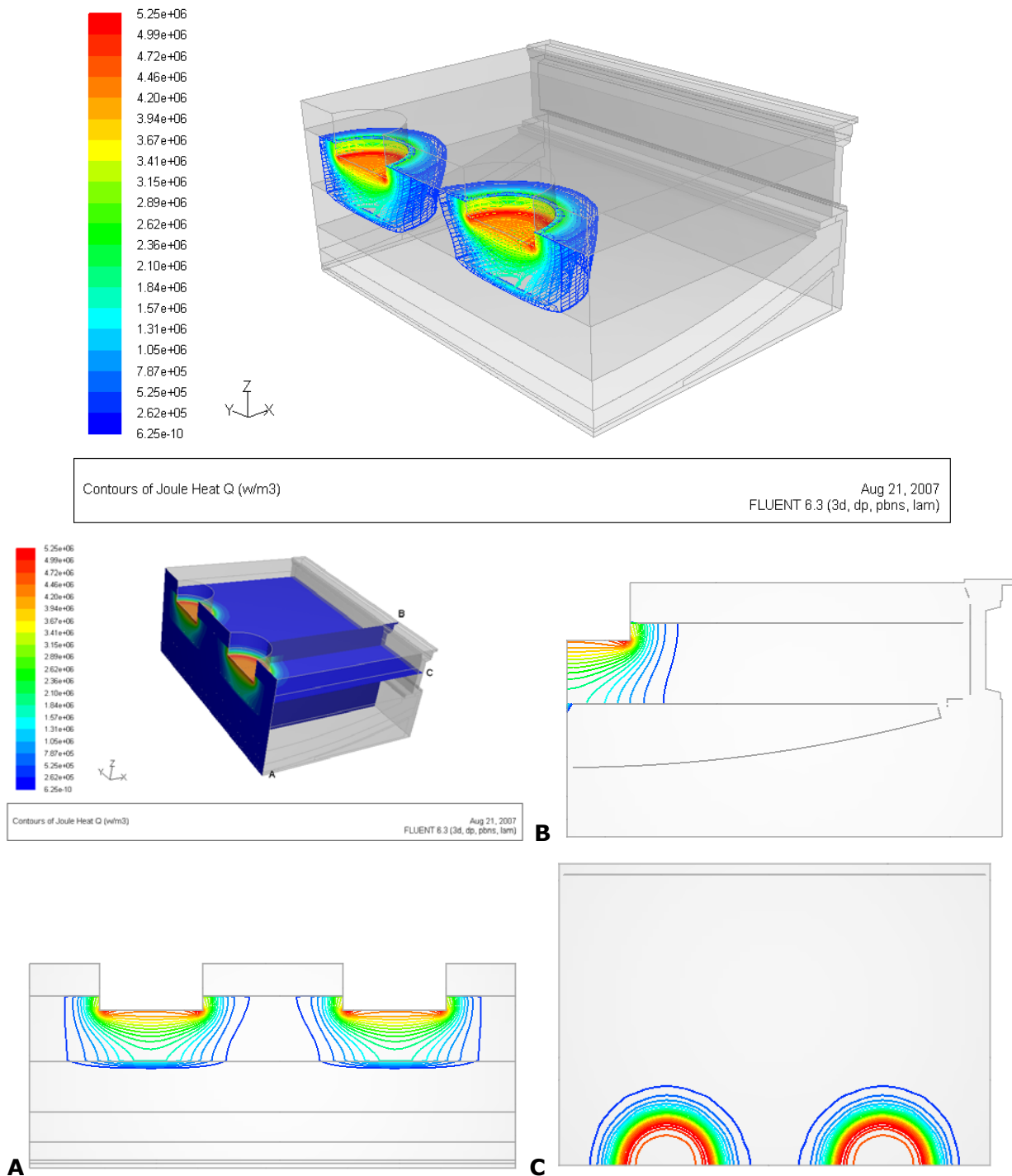


Figure 4.4: A three dimensional view as well as the two dimensional voltage profiles through certain plains of the furnace slice. A – Cut through the centre of both electrodes along the length of the furnace. B - Cut through the middle of one electrode towards the sidewalls showing the arc of the hearth. C – Cut through the slag parallel to the slag/concentrate interface at the bottom the electrode tip.

Sheng *et al.* (1998b) found that the heat release drops away even more sharply from the electrode than does the electrical potential and ascribed it to the heat release being dependent on the square of the potential gradient. A similar trend can be seen in the results given in Figure 4.4 for the heat release and Figure 4.3 for the potential distribution. It is also observed that even with the majority of the current flowing through the matte, the heat generation takes place mainly in the slag due to its resistivity being much higher.

4.3 Temperature distributions

Temperature profiles of the model can be seen in Figure 4.5

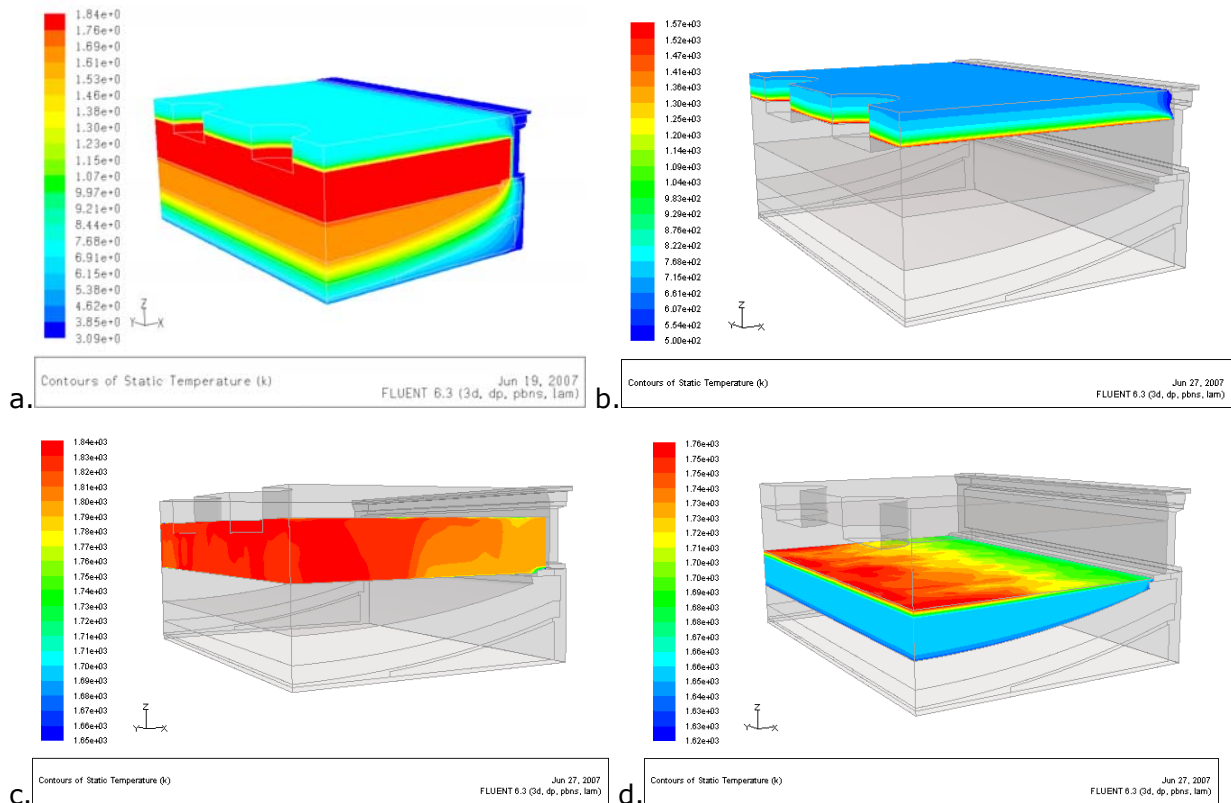


Figure 4.5: Temperature profiles a) The entire model domain b) Concentrate c) Slag d) Matte

Table 4.1 shows the calculated average matte and slag temperatures compared to commonly measured furnace tap temperatures. The calculations are slightly lower when compared to furnace data, which correspond to the energy input for the model, which also shows slightly lower values when compared to actual data.

Table 4.1: Model temperature compared to furnace data

	Model average temperature (°C)	Furnace tap temperatures (°C)
Slag	1533	1550 - 1600
Matte	1380	1450 -1500

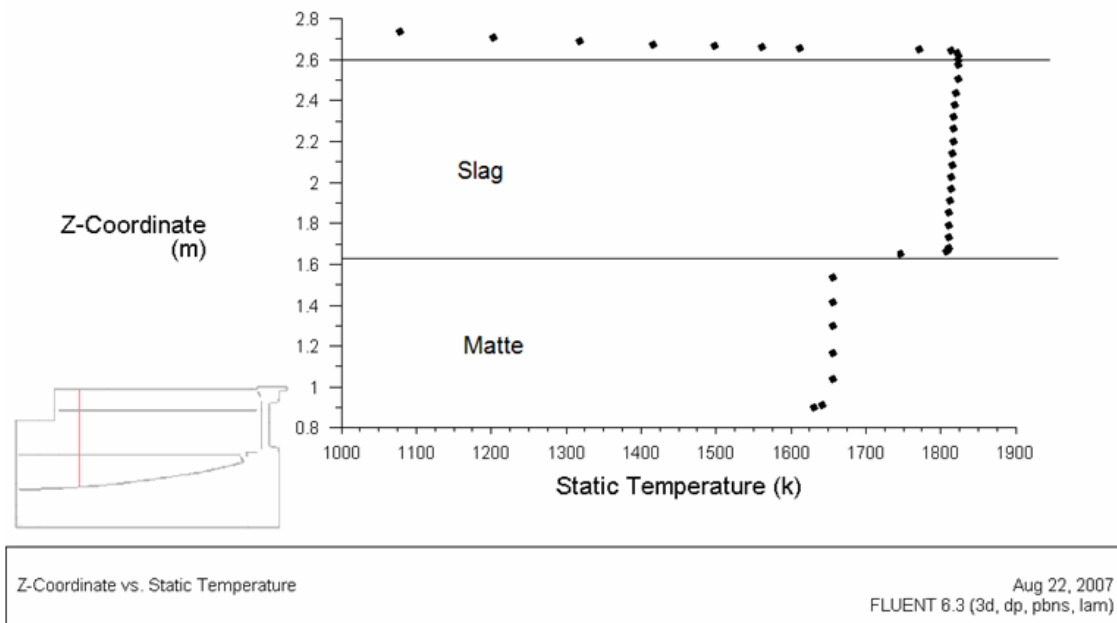
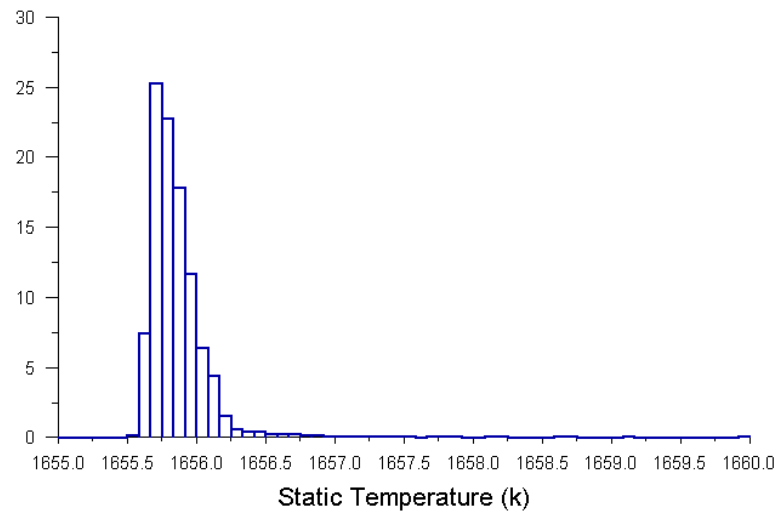


Figure 4.6: The vertical temperature bath profile through the concentrate, matte and slag. The red line in the bottom left corner indicates where the temperature profile was taken.

Figure 4.6 shows the vertical temperature profile through the concentrate matte and slag. A very good resemblance with the measured data from Sheng *et al.* (1998b) is obtained when these results are compared to Figure 2.10 in section 2.3.1.2. It also shows that the temperature through the slag is very homogenous with a sudden drop in temperature from the slag to matte and also a homogenous temperature in the matte layer. The calculated values from Sheng *et al.* (1998b), however, show a more gradual decrease in matte temperature.

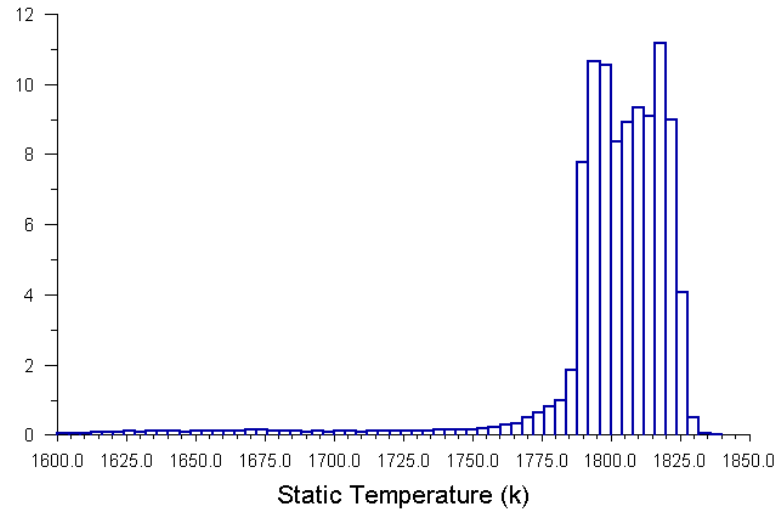
From the histogram for matte in Figure 4.7 it is also indicated that the matte has a very narrow distribution around 1656K, also indicating that the matte has a very uniform temperature through-out the entire bath. This can be attributed to the high thermal conductivity of the matte. The histogram for the slag in Figure 4.8 indicates a more rectangular distribution between 1785 and 1825 Kelvin.



Histogram of Static Temperature

Aug 22, 2007
FLUENT 6.3 (3d, dp, pbns, lam)

Figure 4.7: Histogram of the temperature in the matte showing a very narrow Rayleigh distribution around 1656 K. The temperatures on the boundaries are not included.



Histogram of Static Temperature

Aug 22, 2007
FLUENT 6.3 (3d, dp, pbns, lam)

Figure 4.8: Histogram of the temperature in the slag indicating a small amount of cells with temperatures from 1600K to 1750K with the majority of cells falling in the range between 1785K and 1825K. The temperatures on the boundaries are not included.

4.4 Energy balance

To compare the energy input of the model to furnace data, the total furnace power is divided by six, as the model contains only half of an electrode pair. It is assumed here, however, that the energy distribution to the three electrodes is equal. The energy to half of an electrode pair amounts therefore to 10.8 MW, which should be compared with the model energy input. The summary of the energy balance for the model can be seen in Figure 4.9 and Table 4.2.

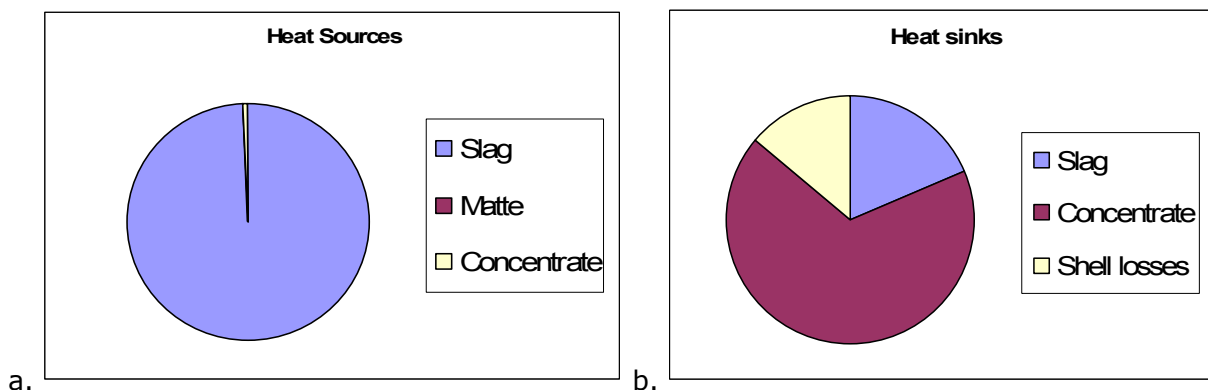


Figure 4.9: Pie charts to show the distribution of energy in the model. a) 99.4% of the energy is generated through joule heating in the slag. b) 67% of the energy is used for concentrate melting.

Table 4.2: A summary of the energy balance for the model showing the heat generation in each section as well as the amount of energy being used in each section of the bath.

	Heat Inputs		Heat Sinks		
	MW	%	MW	%	
Slag	7.5	99.4	Slag	-1.41	18.7
Matte	0.008	0.1	Concentrate	-5.08	67.3
Concentrate	0.035	0.5	Shell losses	-1.06	14.0
Total	7.543				

Even though most of the current flows through the matte (see Figure 4.1) 99.4% of the heat is generated in the slag at the modelled electrode depth. The total amount of energy generated in the bath amounts to 7.543 MW.

According to Figure 5.1b, 67.3% of the energy generated in the bath is used in the heat-up and melting of concentrate and 18.7% of the energy is used to heat the melted

material to the bath temperature. Shell losses amount to 1.06 MW for the model. The model volume comprises about 15% of the total furnace volume, therefore when the shell losses as extrapolated, a value of 7.07MW are predicted for the furnace. According to furnace data, shell losses are between 6 and 8 MW (energy losses due to the off gas is not included) and the predicted value for shell losses are therefore in range.

To account for the power associated with the voltage drop at the electrodes, the calculated electric potential is compared with the measured electric potential.

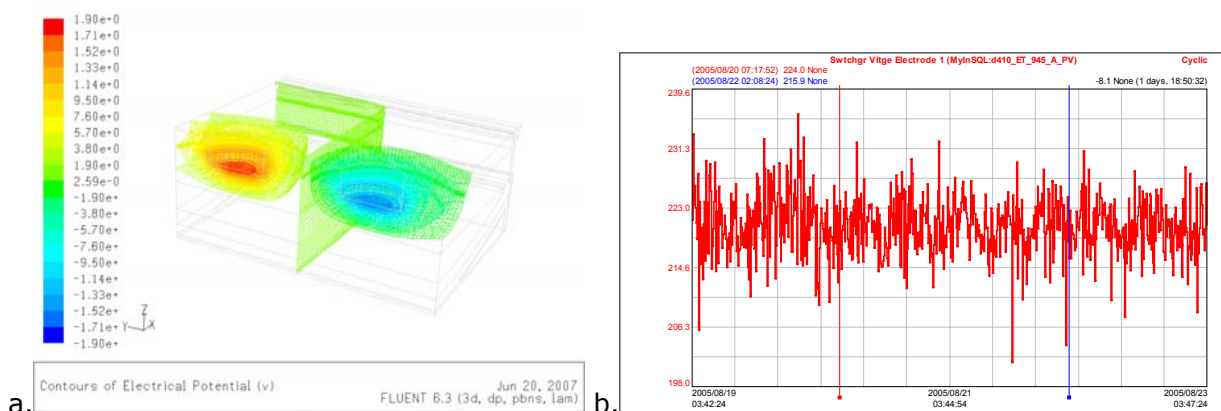


Figure 4.10: The electrode potential calculated with the mode (a) compared to the furnace measured value (b). The difference account for the arcing to the co-gas forming around the electrode tips.

The 30V drop in electric potential amounts to an additional 1.35MW. When added to the 7.54MW of energy generated in the bath, it results in a total amount of energy of 8.8MW, which is slightly lower than the 10.8MW calculated from furnace data. The 8.8MW input can now be adjusted by adjusting the electrical conductivity of the slag, matte and concentrate.

4.5 Slag/matte interface

Sheng *et al.* (1998b) reported that a no-slip boundary condition between the slag and the matte was required to achieve good agreement between computed and measured temperature profiles. Hadley *et al.* (2005) specified the matte zone as a solid layer and only calculated the flow profiles in the slag.

This interface is, however, regarded as critical when the heat transfer from slag to matte is researched and the effect of different boundary conditions between the matte and slag

was therefore investigated. Figure 4.11 shows a summary of the difference in heat transfer from the slag to matte for different boundaries between the matte and the slag.

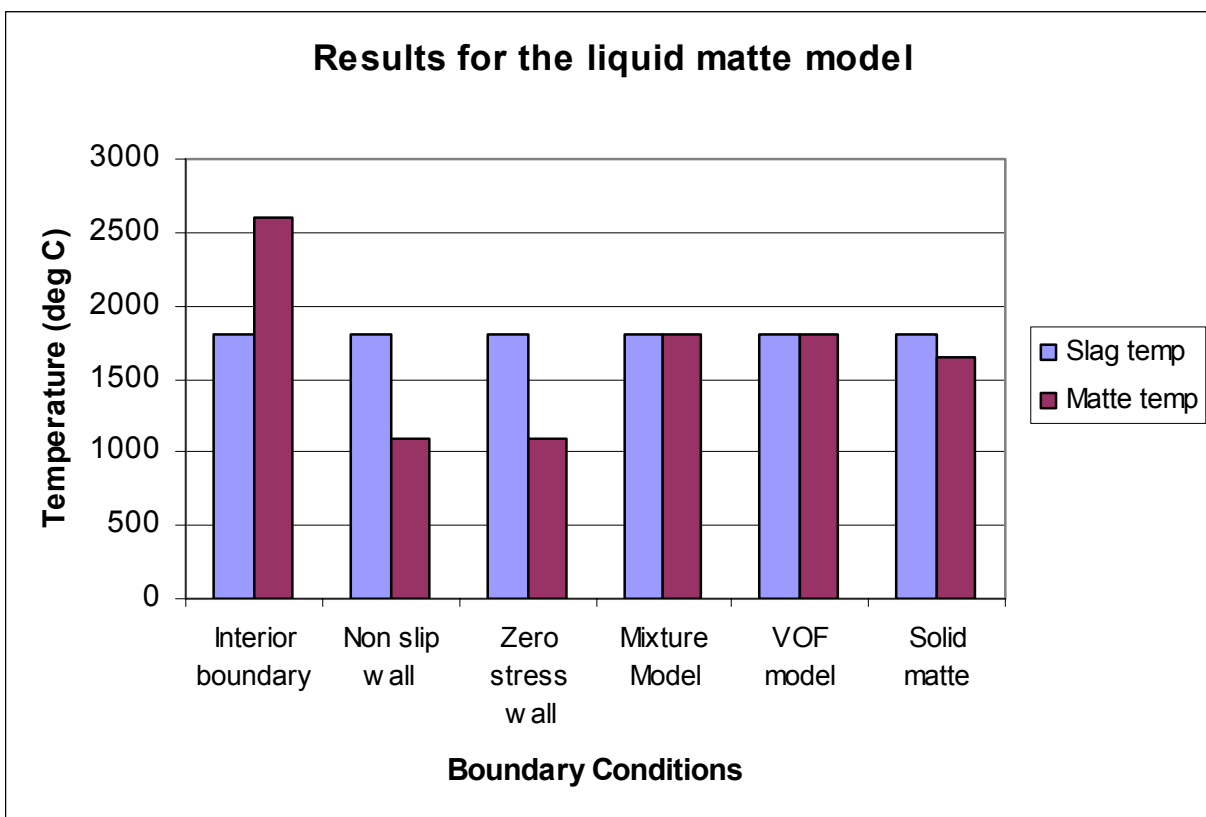


Figure 4.11: Heat transfer results from slag to matte for different interface boundaries.

Upon further investigation into the model, it was, however, found that with added heat sinks in the slag, as explained in section 4.2.2, the difference in slag and matte temperature for the non slip boundary condition is resolved. The desired temperature results for the matte and the slag are then achieved with the non slip boundary condition with the matte modelled as a liquid and when the matte is modelled as a solid zone. The difference is however seen in the flow profiles of the matte and the slag. Figure 4.12 indicates the flow profiles for a solid matte zone, which compare to literature data, but a random flow in the matte and the slag is computed when the matte is modelled as a liquid zone. This is often an indication of poor convergence of the specific variable. These flow profiles were, however, later resolved for the liquid matte model and are discussed in section 4.6.2.

4.6 Flow profiles

As discussed in the previous section, different flow results are obtained for different boundary condition settings between the slag and the matte. The results for the solid matte model, the non-slip wall and the multiphase (mixture and VOF) models will be discussed separately in the following sections.

4.6.1 Solid matte model

4.6.1.1 With gas circulation

A very good comparison between Sheng *et al.* (1998b) is seen for the velocity profiles when the matte is modelled as a solid.

This model indicates that the flow of slag will be from the electrodes towards the sidewall where it will cool down, drop towards the matte layer and circulate back to the electrode. A very interesting V-shape is observed when viewed from the top indicating an almost stagnant zone from the side wall towards the centre of the electrodes. This can be an important factor in determining the location of feed ports in the design of the furnace suggesting the feed ports to be closer towards the electrodes and more in between electrode pairs.

This shape in the velocity vectors might also be the explanation as to why the bath temperatures dropped after the concentrate feed ports were moved closer to the electrodes after the 2005 furnace shutdown. As the concentrate is fed to an area where the slag is moving at a higher velocity, the tendency will be to pull more concentrate into the slag with more energy therefore flowing into the concentrate and not heating up the slag. Validation of these results is still required though.

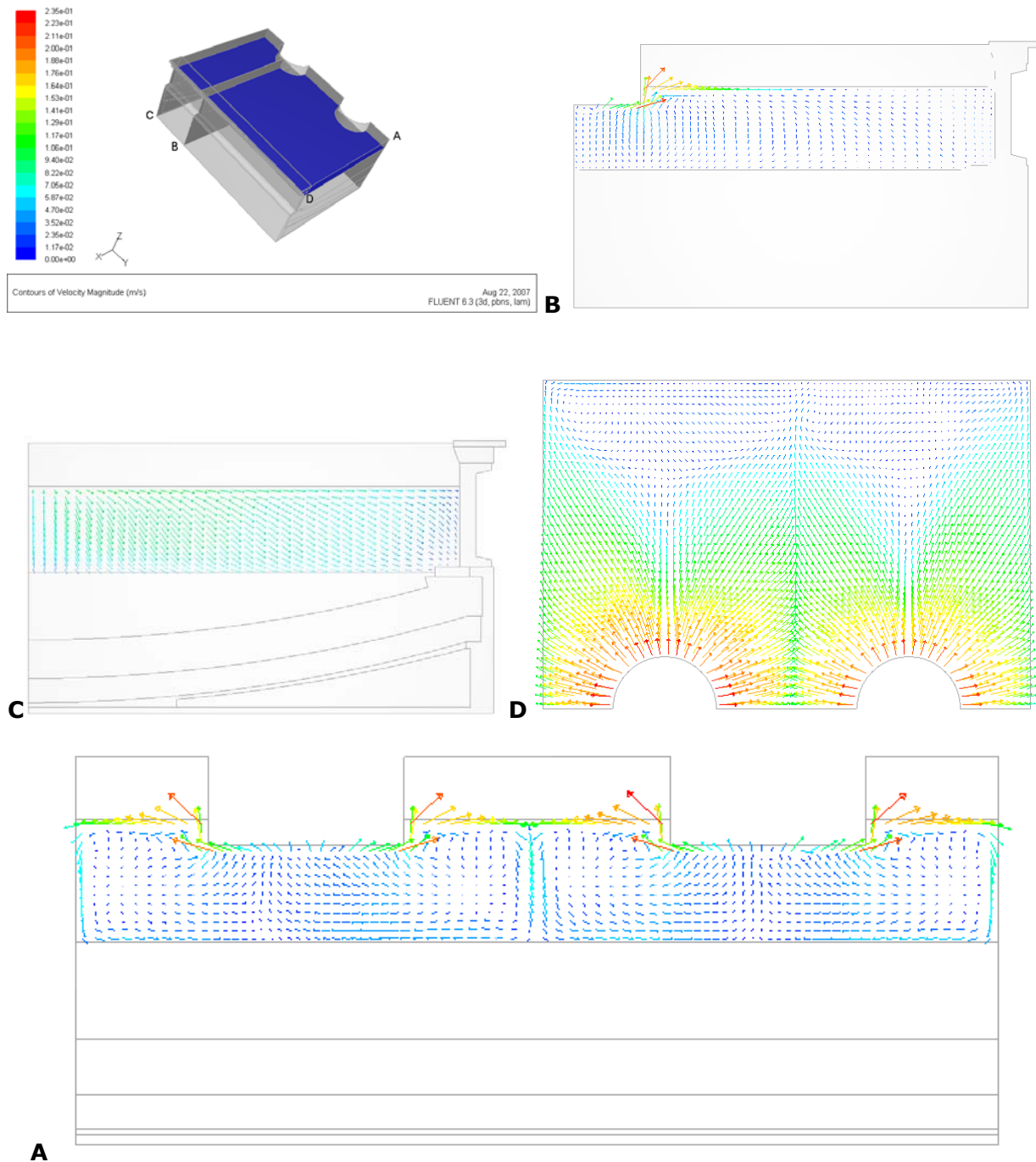


Figure 4.12: The two dimensional velocity vectors through certain plains of the furnace slice. A – Cut through the centre of both electrodes along the length of the furnace. B - Cut through the middle of one electrode towards the sidewalls showing the arc of the hearth. C – Parallel to cut B but in between the two electrodes. D – Cut along the slag concentrate interface.

4.6.1.2 Without gas circulation

To determine the effect of the gas bubble formation on the velocity vectors in the slag compared to only natural buoyancy effects due to density differences in the slag, the discrete element models for the formation of bubbles were switched off for one simulation. (Figure 4.13)

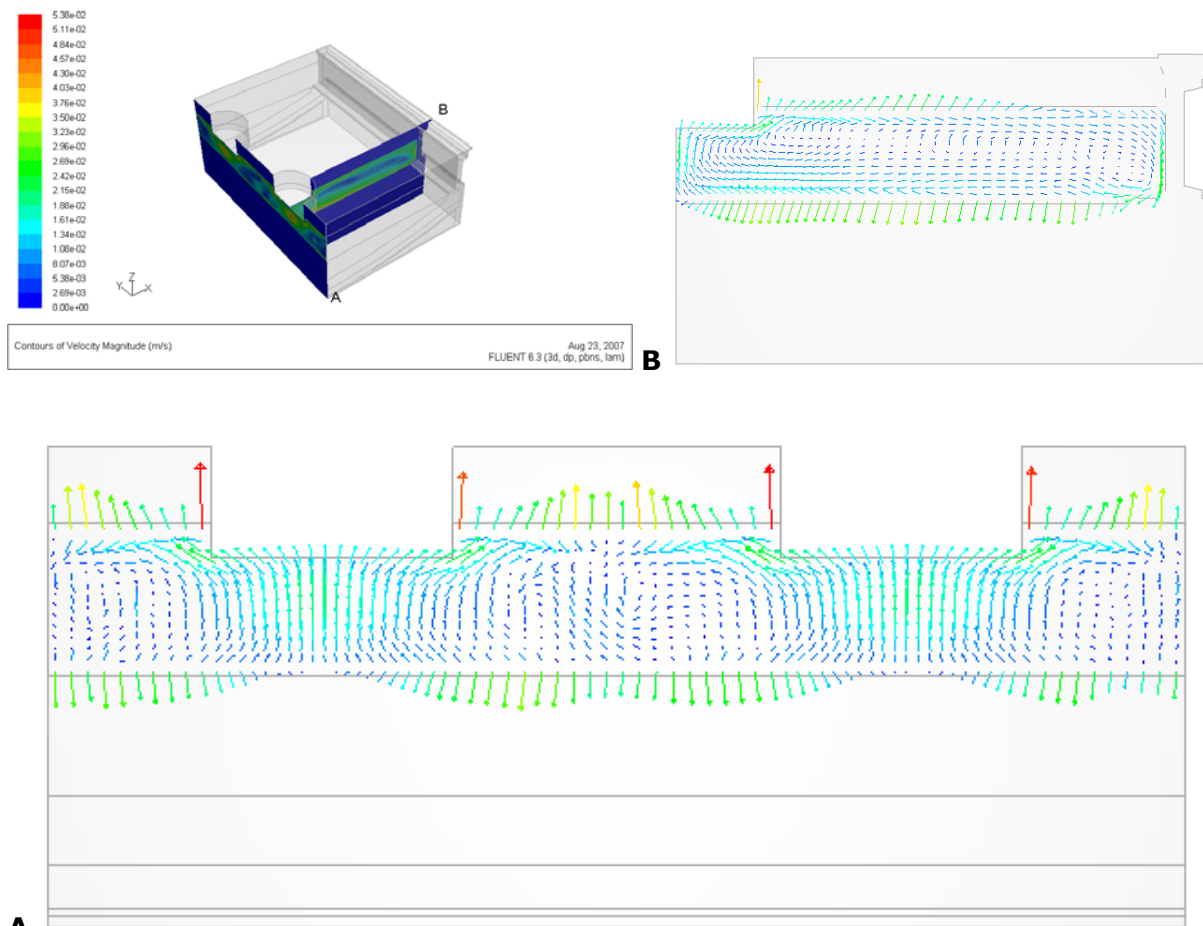


Figure 4.13: The two dimensional velocity vectors without any gas formation around the electrodes through certain plains of the furnace slice. A – Cut through the centre of both electrodes along the length of the furnace. B - Cut through the middle of one electrode towards the sidewalls showing the arc of the hearth.

The flow of the slag is also from the electrodes towards the outer wall and back as indicated in Figure 4.13. The velocity of the slag is compared in Figure 4.14a and Figure 4.14b. The contribution of the gas formation on the velocity of the slag is definitely significant.

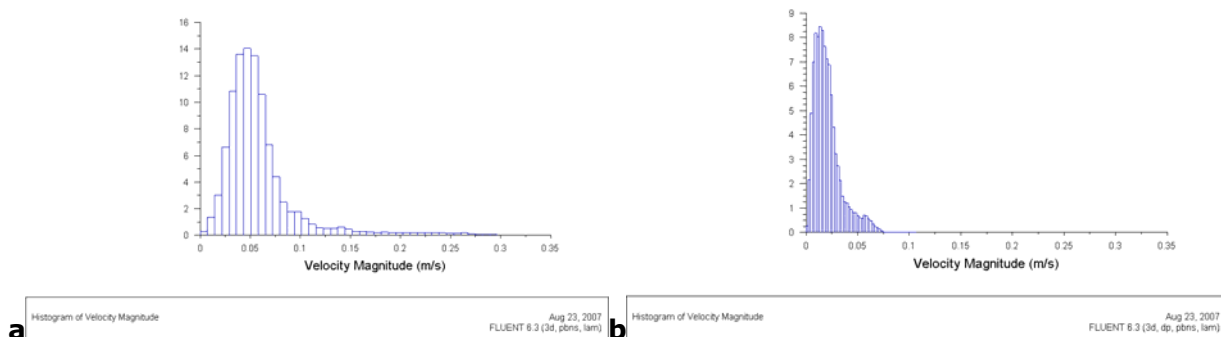


Figure 4.14: Velocity distributions for the slag a) with gas formation at the electrodes and b) without gas formation at the electrodes indicating a much faster velocity in the slag with gas formation.

4.6.2 Liquid matte model

As mentioned previously in section 4.5, when the modelling parameter for the matte is changed from a solid zone to a liquid zone, the flow in the slag and the matte indicates a random behaviour with no specific profile in either the matte or the slag.

To investigate this behaviour, a simplified model was developed to determine whether Fluent can indeed successfully solve the flow for two separate liquids in adjacent model zones and not having to use a multiphase model. The different approaches that were investigated for two adjacent liquid zones were:

- Flows in the same direction without any temperature modelling.
- Flows in the same direction with temperature modelling.
- Flows with opposite directions without temperature.
- Flows with opposite directions with temperature.
- One flowing liquid and one stagnant liquid without temperature.
- One flowing liquid and one stagnant liquid with temperature.

All these modelling approaches gave satisfactory results indicating that Fluent is indeed capable of handling two adjacent liquid zones with flow.

The solution to the problem is found in the discretization scheme used for pressure. The standard pressure interpolation scheme is acceptable in most cases and assumes that the normal pressure gradient at the wall is zero. This is valid for boundary layers, but not in

the presence of body forces or natural convection or curvature and the failure to correctly account for the wall pressure gradient is manifested in velocity vectors pointing in or out of the walls as shown in Figure 4.15 (*Fluent 6.2 Users guide 2005*)

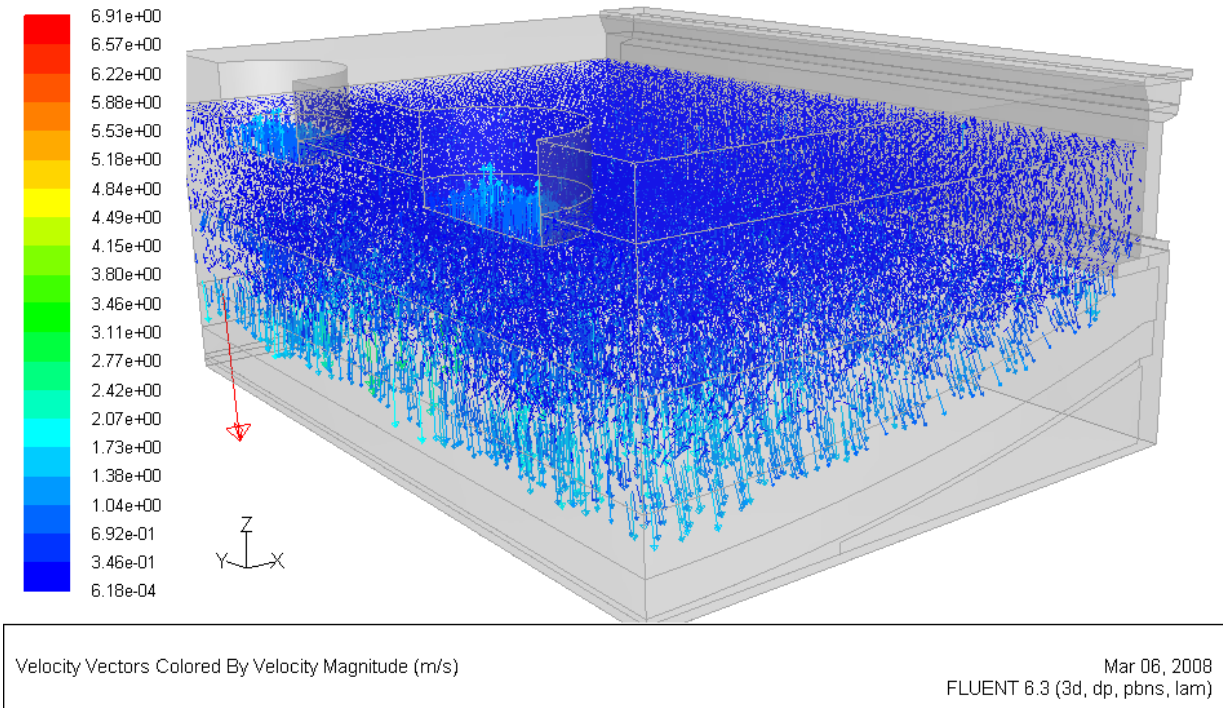
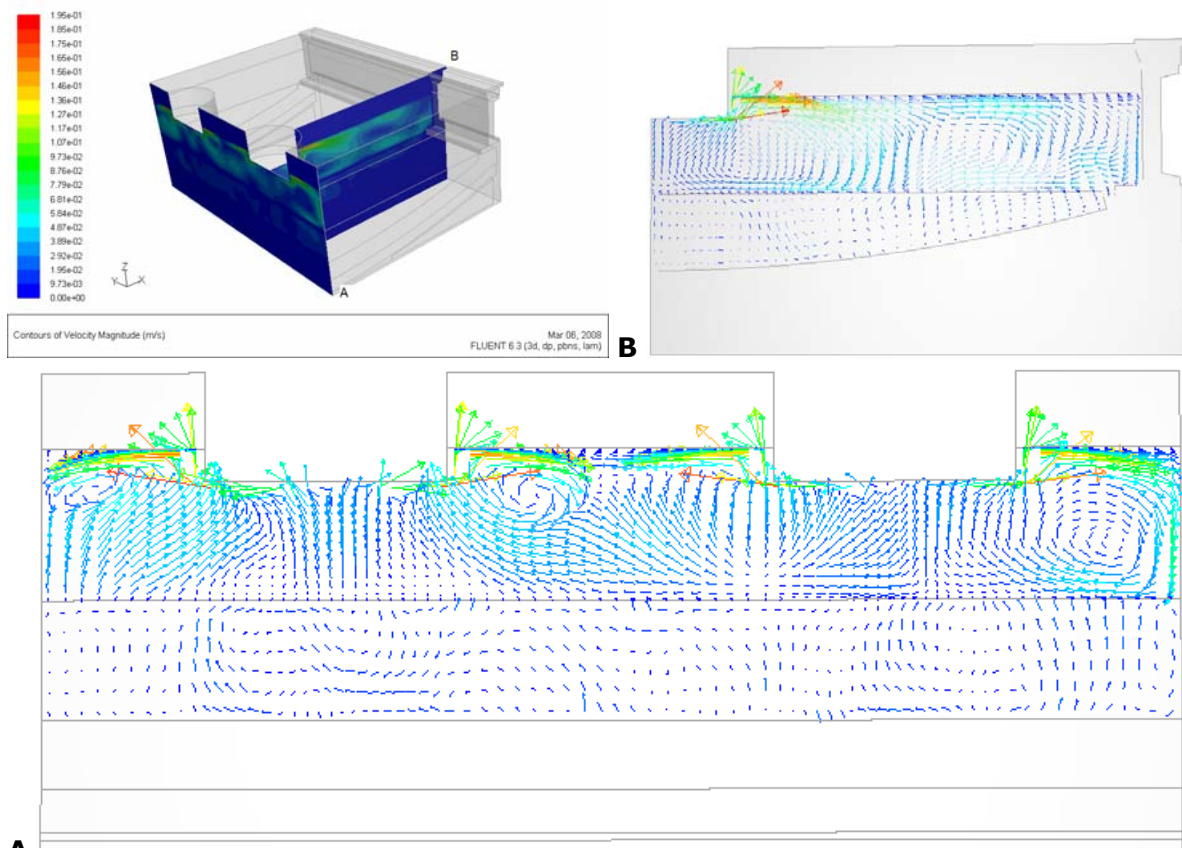


Figure 4.15: Velocity vectors pointing in and out of the walls with the standard pressure discretization scheme.

The PRESTO (Pressure Staggering Option) scheme calculates a staggered face pressure and is the recommended discretization scheme for flows with natural convection.

Figure 4.16 shows the calculated velocity profiles in the matte and the slag with the size of the vectors around the electrode calculated at 0.2 m/s in the slag with a more stagnant matte layer. These velocity profiles resemble the calculated profiles of Sheng *et al.* (1998b) in pattern and size remarkably well. Their calculated speed for the slag around the electrodes also indicates a size of 0.2 m/s. (see page 43)



A
Figure 4.16: Calculated velocity vectors in the slag and matte with the 'PRESTO' discretization scheme. These velocity vectors resemble the results from Sheng *et al.* (1998) well in pattern and size.

4.6.3 Multiphase modelling

One of the main purposes with the multiphase model was to determine whether there is a flow in the matte or whether it is a stagnant zone. Figure 4.17 clearly indicates a flow in the matte and the slag although the flow in the slag does not reflect the velocity profiles as indicated in section 4.6.1. It is, however, the first study making use of multiphase modelling to determine the flow in the matte and before any conclusions can be drawn, proper validation should take place. Multiphase modelling is also very computational intensive and the results shown in Figure 4.17 are at the specific point in time which is after only 5.27 seconds and should therefore be computed longer until a steady state operation is reached. Steady state operation here is assumed to be when the velocity vector results for the transient solution don't change anymore. This is necessary if a comparison between these results and the previous steady state operations is drawn. It is interesting to note that the velocity profiles calculated by the multiphase modelling are

very similar to the velocity vectors calculated by Jardy *et al.* for a circular furnace. See Figure 2.12 in section 2.5.1.2

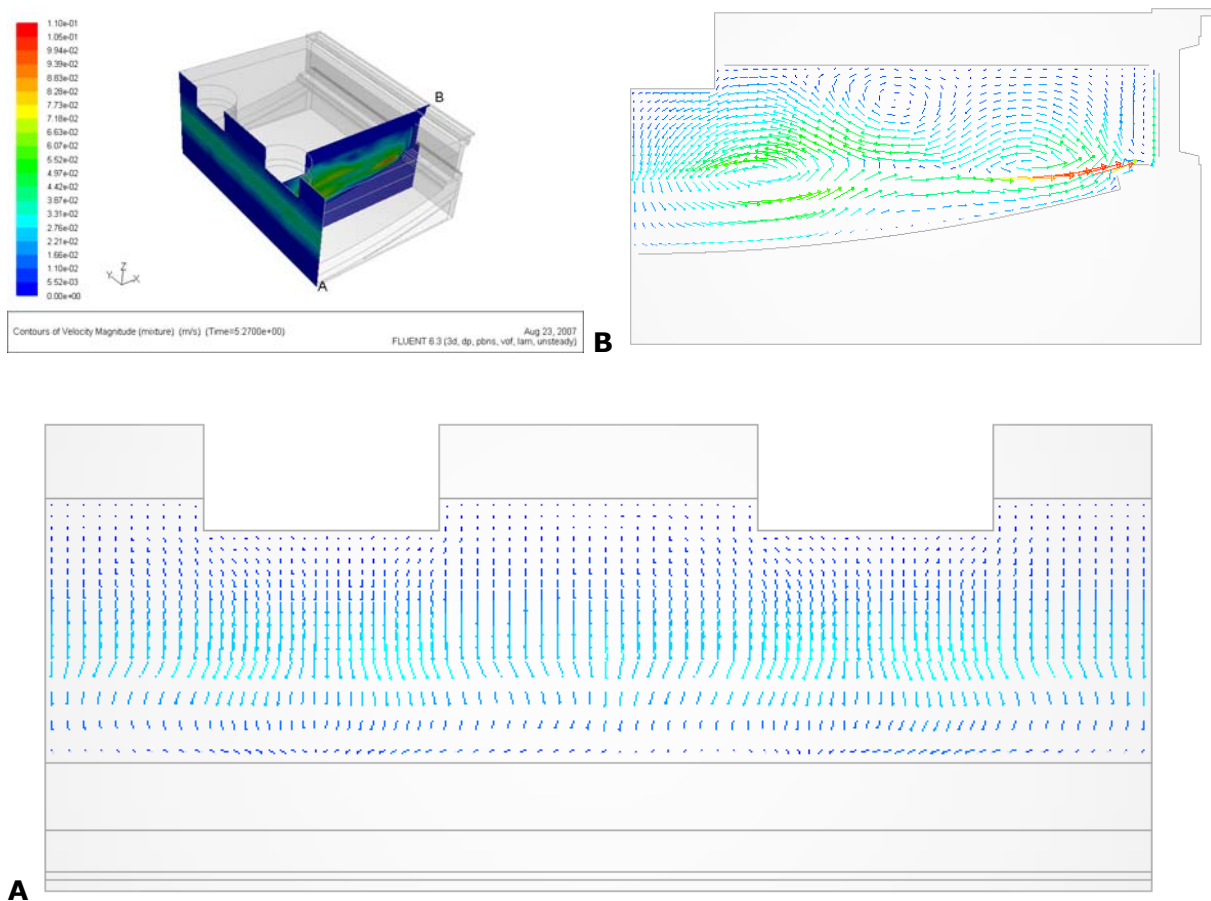


Figure 4.17: The two dimensional velocity vectors for the VOF multiphase model through certain plains of the furnace slice. A – Cut through the centre of both electrodes along the length of the furnace. B - Cut through the middle of one electrode towards the sidewalls showing the arc of the hearth.

4.7 Surface heat fluxes

One of the important areas of focus when managing and operating a large furnace is to ensure that the heat fluxes and temperatures of the outer walls are within the required limits to ensure that the integrity of the furnace walls and refractories is good. It was therefore deemed important to show these results as well. It will also play an important role when validating the model results as most of these temperatures can be measured.

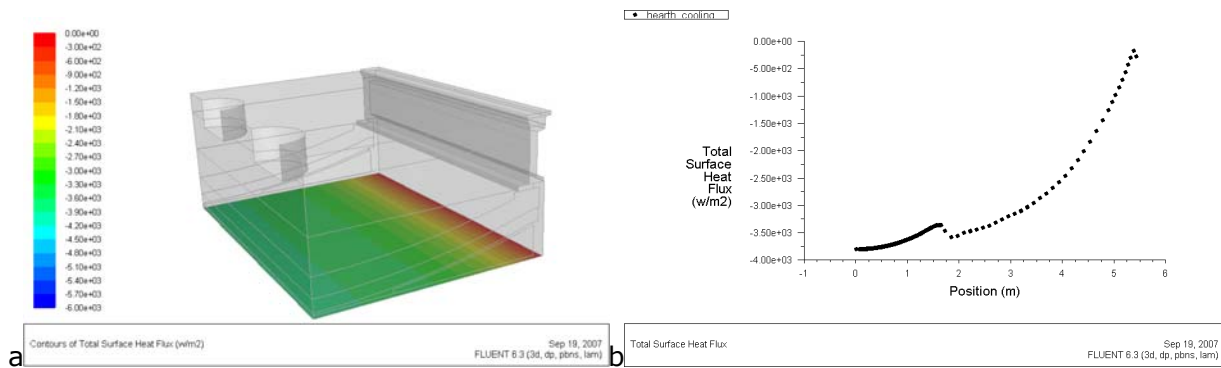


Figure 4.18: Total surface heat fluxes on the hearth of the furnace. b – indicates a plot of the heat flux from the centre of the furnaces where the heat fluxes are the highest and dropping to zero in the corner. An interesting kink is shown in the heat fluxes just off the centre.

Figure 4.18 gives an indication of the total surface heat flux for the hearth. The highest heat fluxes occur at the centre of the furnaces directly below the electrodes at just less than 4 kW/m² and then drops away to zero in the corner of the hearth and the sidewall. An interesting kink in the heat fluxes are observed at about 1.8 m from the centre of the furnace where the refractory changes slightly due to the arc of the furnace and less infill ram refractory is used. See figure 4.19.

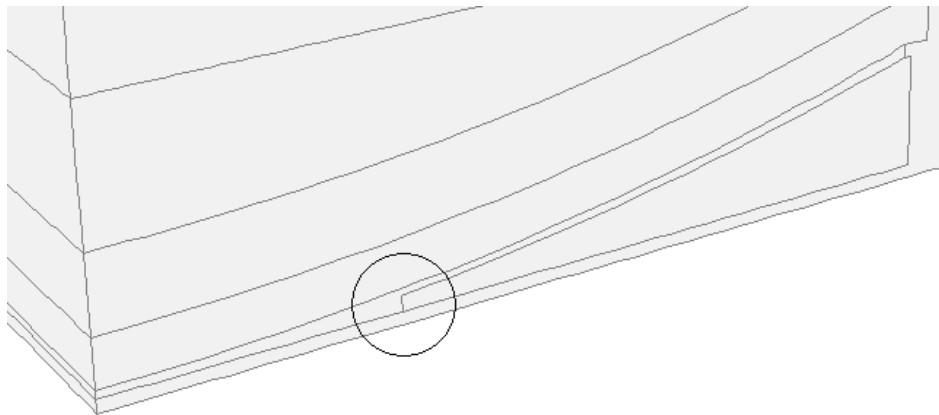


Figure 4.19: A change in refractory thickness causes a change in total surface heat fluxes in the hearth.

The sidewall heat fluxes are shown in a similar manner in Figure 4.20 with maximum heat flux at just less than 3 kW/m³.

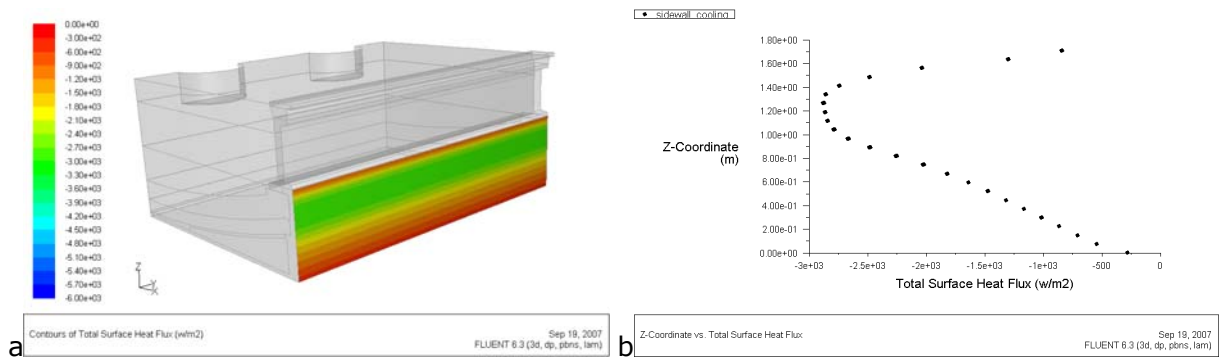


Figure 4.20: Total surface heat fluxes on the sidewall of the furnace. b – Indicates a plot of the heat flux from top of the sidewall cooling showing an increasing heat flux towards a maximum point and then decreasing again to zero at the corner of the furnace.

The copper coolers are also a critical area of the furnace. In reality the heat is removed with water channels flowing in the copper and not through the outer wall of the copper as indicated here, but the heat fluxes here are still shown to give perspective on the size of the heat fluxes in this region compared to the hearth and sidewalls.

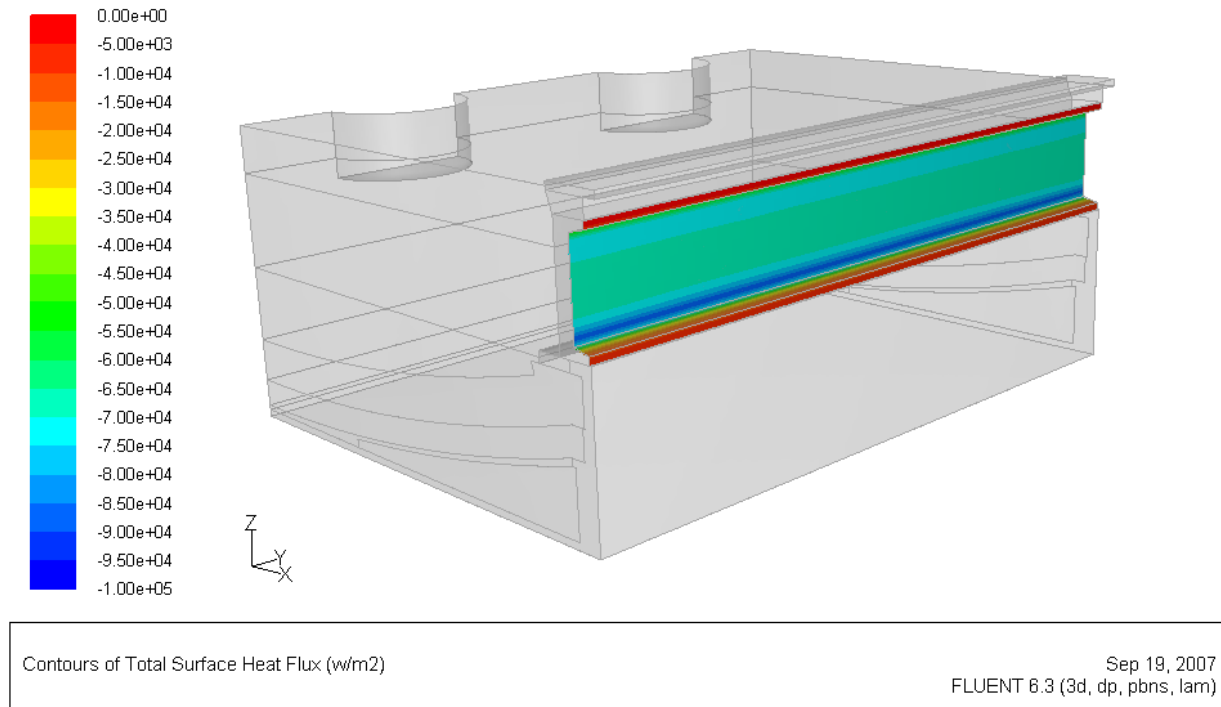


Figure 4.21: Copper cooler heat fluxes

4.8 Computational efficiency

The computational efficiency of a model can be determined by a number of factors. The type of grid and grid independence, as well as the complexity of the simulation, have a strong influence on the model convergence for example and all contribute to the accuracy of the model results. The time it takes to run one simulation has a detrimental effect on the blood pressure of the modeller and very long simulation times are unwanted for obvious reasons. This may be necessary though.

4.8.1 Grid Independence

The grid around the slag and concentrate interface, as well as the slag and matte interface was subjected to refinement until it was found that the temperature profile as well as the heat sinks in these areas, didn't change significantly anymore. The same structure as described in section 3.1.3.1 and only the sizes of the cells were therefore changed until grid independence was reached.

4.8.2 Convergence

Very strong converging criteria will cost unnecessary computing time and although computers have increased in computing power significantly, so has the complexity of the models that are being developed, and is therefore still a factor that needs to be taken into consideration. Too weak criteria, however, will reduce the accuracy of the results.

In a generally accepted rule of thumb, residuals should drop three orders of magnitude when judging convergence.

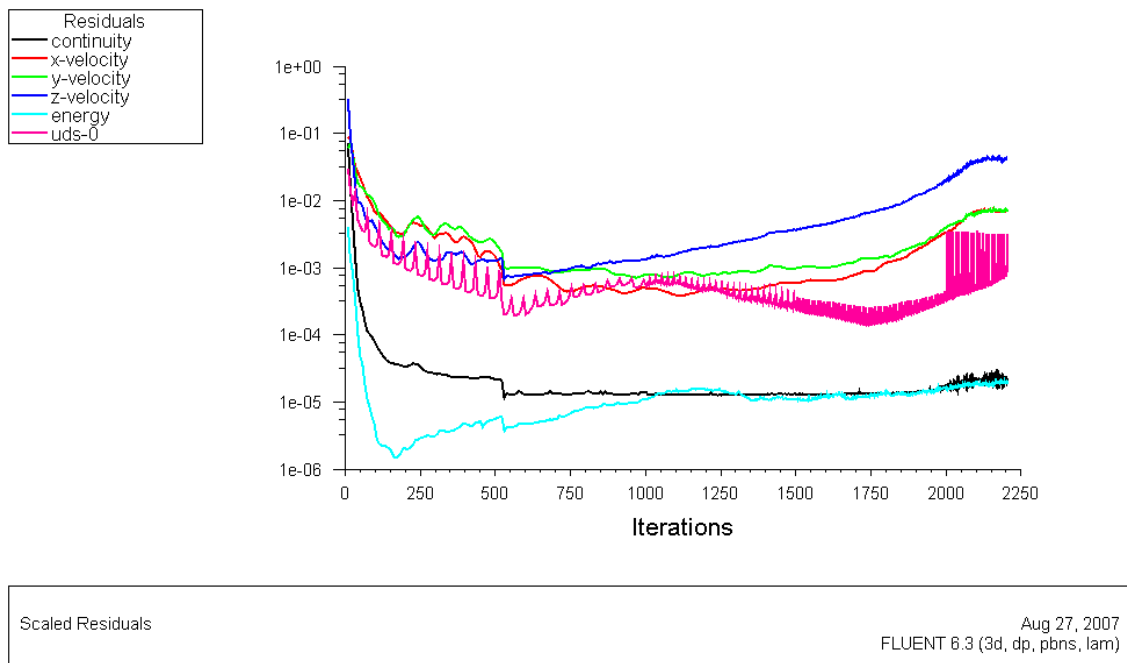


Figure 4.22: Typical plot of the residuals during iterating. A steep drop during the initial iterations is observed and then gradually starts climbing until it stays constant.

Figure 4.22 shows a typical plot of the residuals during the iterations. A sharp drop for all the residuals is initially observed from where it then gradually starts climbing until it reaches a constant value. According to only the residuals, the most converged point mathematically in the solution will be where the residuals are at the lowest point. It is, however, necessary to ensure that all the results, for example temperatures, are stable and not changing with iterations anymore as well as the residuals. It was mainly these plots that determined the convergence for this specific model.

From figure 4.23a it can be seen that the average volume weighted temperatures for the matte and slag remain almost 100% constant with iterations when judged by the eye only. The scale is, however, fairly large so the change rate of the temperature was calculated for the hearth of the furnace slice. The change rate is less than $0.0003^{\circ}\text{C}/\text{iteration}$ as can be seen in Figure 4.23b indicating that the model is well converged.

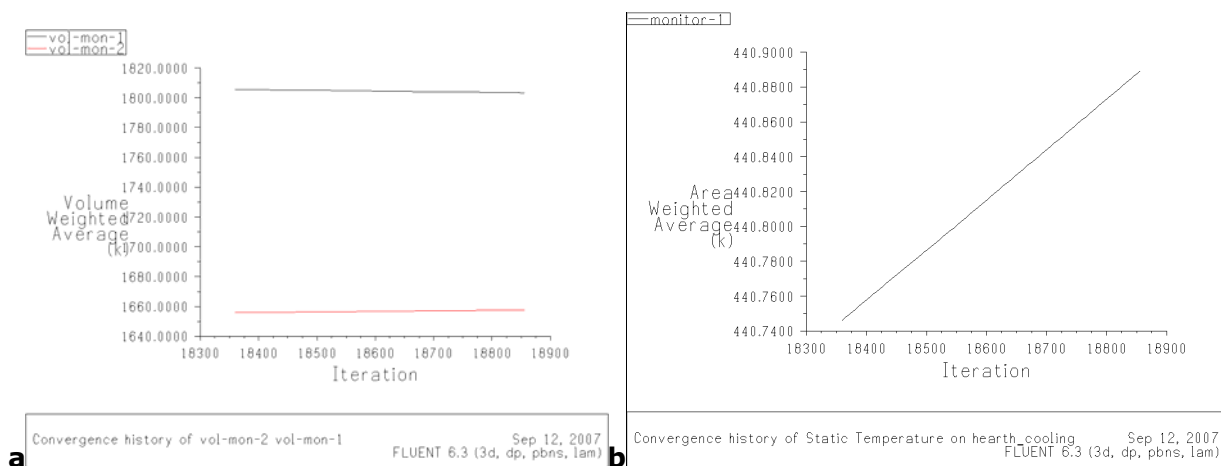


Figure 4.23: Convergence monitoring of furnace slice. a) The average matte and slag temperature remaining almost 100% constant with iterations. b) indicates that the hearth temperature changes at less than 0.0003°C/iterations.

4.8.3 CPU time

All the models and development models were simulated on a DELL Latitude D810 laptop computer with a single Intel Pentium processor rated at 2.13 GHz with 1.00 GB RAM of 787MHz.

For the latest model, convergence was reached after about 26 hours of uninterrupted computing time, indicating that the computing time is not as much a limiting factor as in the past.

Faster computing times can be reached with faster computers and parallel processing. Parallel processing is when 2 or more processors are used for computing a solution.

4.9 Modelling at different immersion depths

This section mainly falls outside the scope of the MSc study, but is introduction work to the primary objective of the study, which is to determine the factors that influence the energy distribution inside the furnace. The section mainly focuses on different electrode immersions.

Due to the complexity of the models, exact conversion of the models is difficult to determine and to determine the exact same degree of conversion for the different models

is even more difficult. The conversion in this section was mainly determined by the average temperature of the slag and the amount of joule heating in the slag. The results are acceptable for the purpose of comparison of the models, but slightly more accurate values can be expected with better conversed models. For a more in-depth research, the conversion of more variables should be taken into account. This, however, can be very timely and a science on its own and will not be discussed here.

4.9.1 Constant Current

Models were developed at 10, 20, 35 and 60% electrode immersion depths. All parameters were kept constant including current through the electrodes. For the current to remain the same, the current density boundary condition needs to be adapted for each electrode immersion. Table 4.1 show the boundary conditions used at the different electrode immersions.

Table 4.1: Current density boundary conditions specified at different electrode immersion depths

Current (kA)	Immersion (%)	Area in slag (m ²)	Current density (A/m)
45	10	2.5	17905
45	20	3.0	14921
45	35	3.8	11937
45	60	5.0	8952

From the boundary conditions as shown above, the difference in current path can now be investigated. It is found as per Figure 4.24 that the current density at all four electrode immersion depths tend to be similar with regards to the higher current densities in the matte and almost zero between the electrodes even with immersion depths as shallow as 10%.

Although the path of the current remains the same, the current density size does change around the tip of the electrode with a clearly visible higher current density around the tip if the electrodes are immersed at 10% and a slight indication of higher current densities through the matte at the deeper electrodes immersions. It is, however, recommended that the current density in the matte is analysed statistically before any substantial conclusions are drawn.

The higher current density in the slag around the electrode tips greatly affects the joule heating released in the slag. Figure 4.25a indicates the joule heating in the slag with regards to the electrode immersion and Figure 4.25b shows the joule heating in the matte and the concentrate.

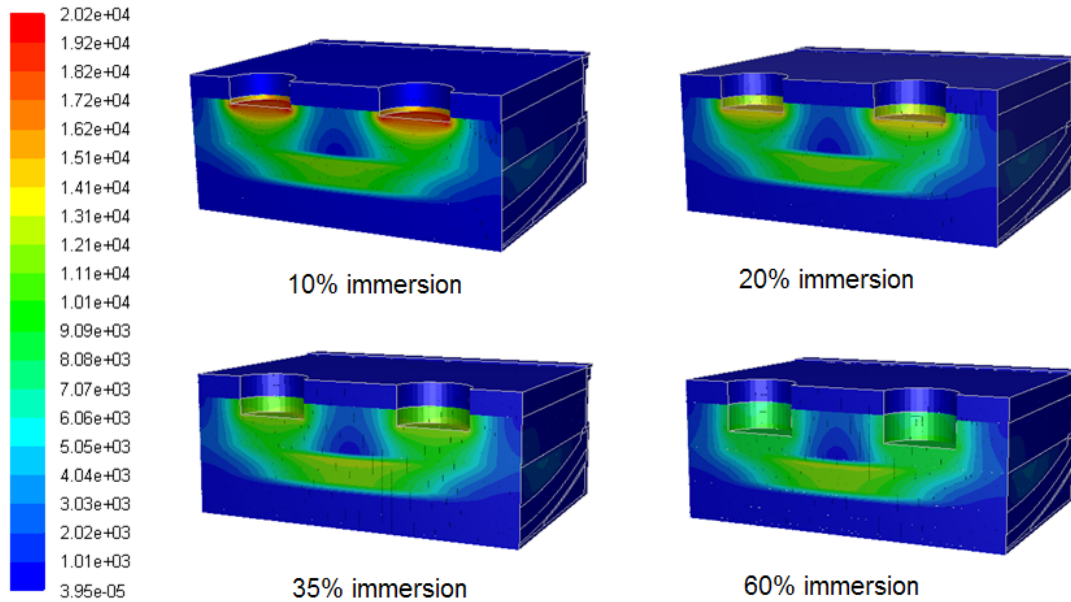


Figure 4.24: Current densities at different electrode immersion depths. The highest current densities are still shown to be in the matte and not in between the electrodes for all four cases.

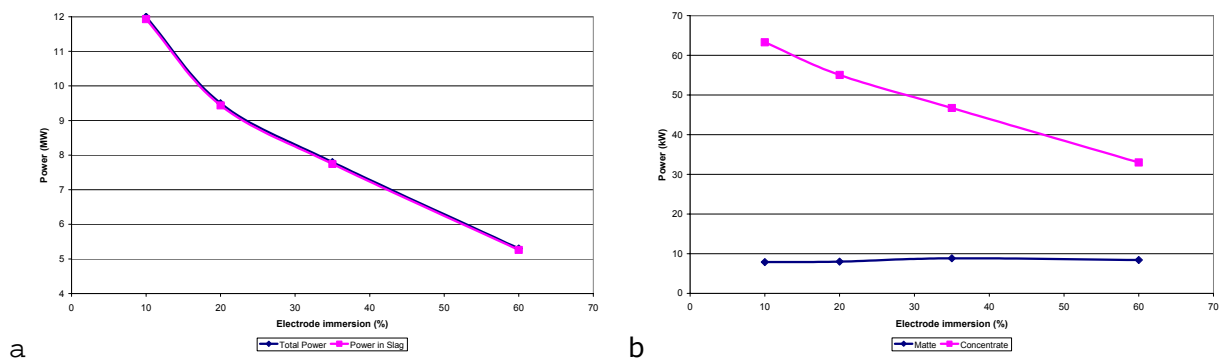


Figure 4.25: Power dissipation in the a) slag and b) matte and concentrate. While the power generated in the slag decreases with increasing immersion depth, the power generated in the matte remains constant.

The energy distribution, based on the calculated joule values of Figure 4.25, is shown in Table 4.2. A very slight increase in the amount of energy dissipated in the matte is seen. It is predicted, however, that the amount of joule heating and the increasing of energy in the matte will be enhanced with a lower matte conductivity. The sensitivity of the amount of energy generated in the matte due to electrical conductivity needs to be investigated formally.

Table 4.2: Energy generation distribution in the bath with immersion depth. The energy in the matte increases slightly with increasing electrode immersion.

Energy generation distribution (%)			
Immersion (%)	Matte	Concentrate	Slag
10	0.07	0.53	99.41
20	0.08	0.58	99.34
35	0.11	0.60	99.29
60	0.16	0.62	99.22

The effect of immersion on the average temperature in the matte and slag can be seen in Figure 4.26. It is clearly seen that the difference between the matte temperature and the slag temperature decreases as the electrode immersion depth is increased. At 60% immersion depth, a difference of only 50°C is predicted with the current modelling parameters and assumptions.

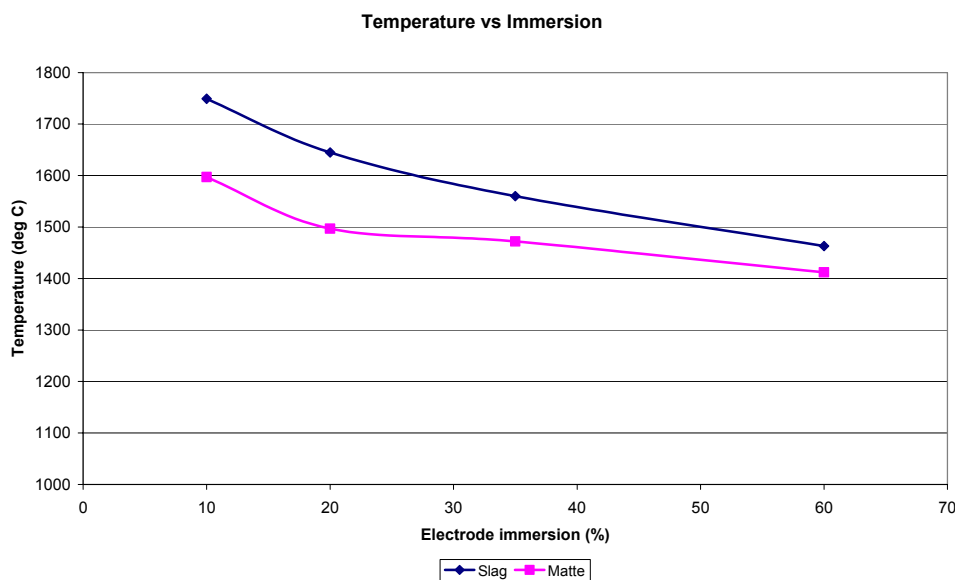


Figure 4.26: The effect of immersion on the average temperature in the matte and the slag. The difference in the average temperature between matte and slag decreases with increasing electrode immersion. It is important to note here that the power generation also decreases with increasing electrode immersion as per the model parameters.

The flow profiles were analysed and compared by changing the scale of the velocity vectors to first incorporate all the vectors and specifically to capture the area with high values and then to an averaged bath velocity vector at which most of the flow in the bath occurs.

Figure 4.27 shows the velocity vectors for different immersion depths including all the vectors. The scale is set to show vectors between the range of 1 and 0.4 m/s. From Figure 4.27, higher velocity vectors are seen and seem to increase in the slag in the immediate vicinity of the electrodes as the electrode immersion increases.

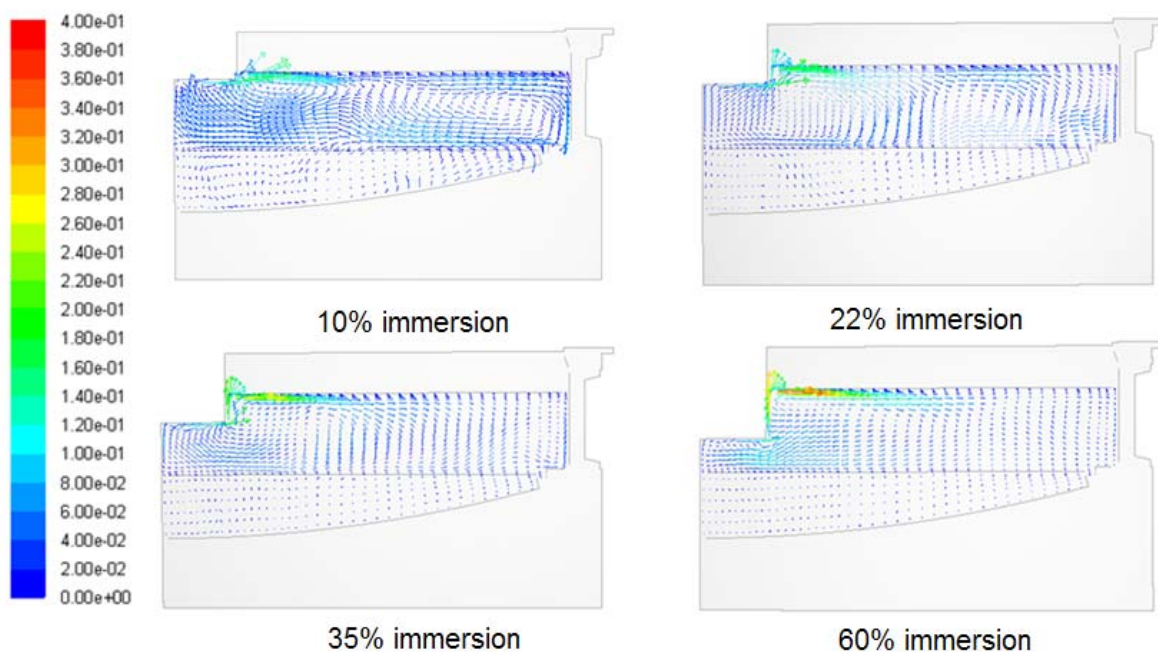


Figure 4.27: Velocity vectors in the slag and the matte at different immersion depths. Higher velocity vectors are seen in the immediate vicinity of the electrodes with the deeper immersed electrodes.

As the majority of the vectors in the bulk of the slag are much less than the 0.4 m/s, the scale was changed to be better able to compare the overall flow in the slag. Figure 4.28 shows the velocity vectors if the scale is changed to incorporate the vectors between 0 and 0.06 m/s. The areas where no vectors are present in Figure 4.28 are the areas where the vectors fall outside the set range of between 0 and 0.06 m/s, in other words, it's the areas where the vectors exceed 0.06 m/s.

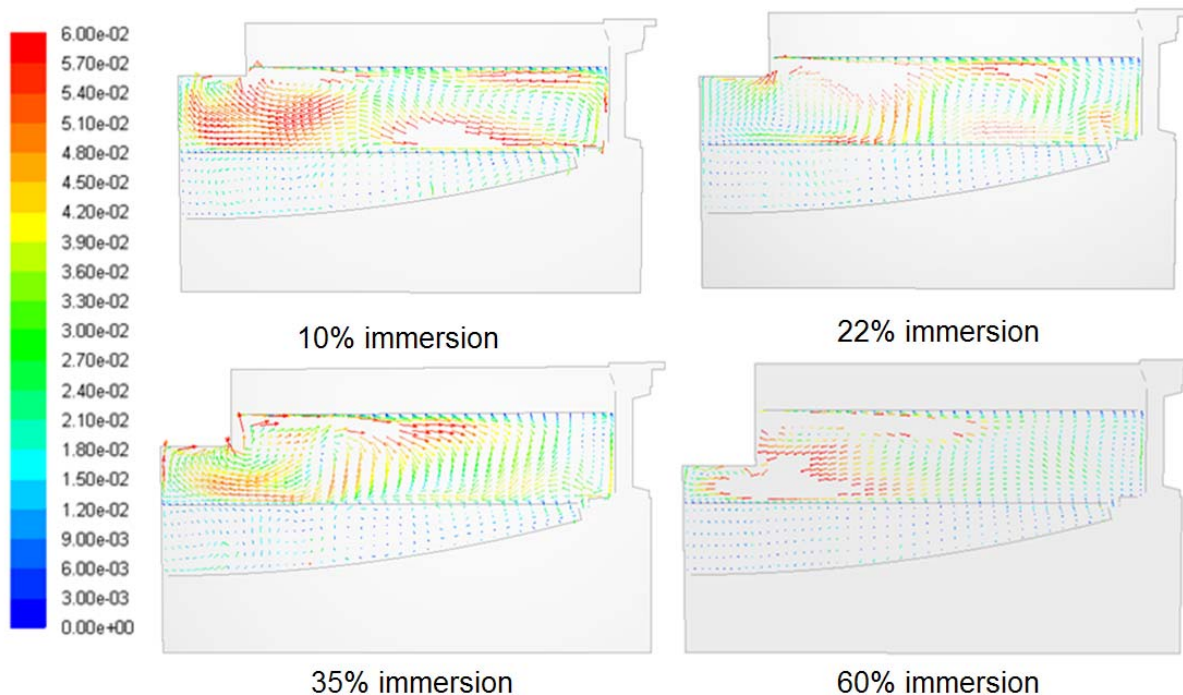


Figure 4.28: Velocity vectors indicating the vectors between 0 and 0.06 m/s. The areas with no vectors present are at velocities higher than 0.06 m/s.

From Figure 4.28, the indication is that the vectors around and underneath the electrodes in the slag seem to increase with electrode immersion, except for 10% immersion. The vectors close to the middle of the slag area and closer towards the sidewall seem to decrease in size. Even though 10% electrode immersion shows a higher velocity around the electrode than the 22% and 35% immersion cases, higher velocities towards the middle of the slag are still seen in the 10% immersion case. The 60% immersion case is just the opposite, with higher velocities around the electrode and lower velocities towards the sidewall.

To confirm this observation, the area around the copper sidewall was enlarged and compared for the different immersion cases and is shown in Figure 4.29. Here it is clearly seen that as the immersion depths increase, the velocity vectors at the copper sidewall decrease.

It is, however, important to note that in these immersion cases, the electrical current was kept constant in each of these cases which resulted in less energy and lower temperatures as the immersion increases. The lower velocities towards the middle of the slag and at the copper sidewall are therefore not contributing to the deeper immersion, but rather to the

lower temperatures that occur in the slag due to the way the model parameters were chosen in these specific cases.

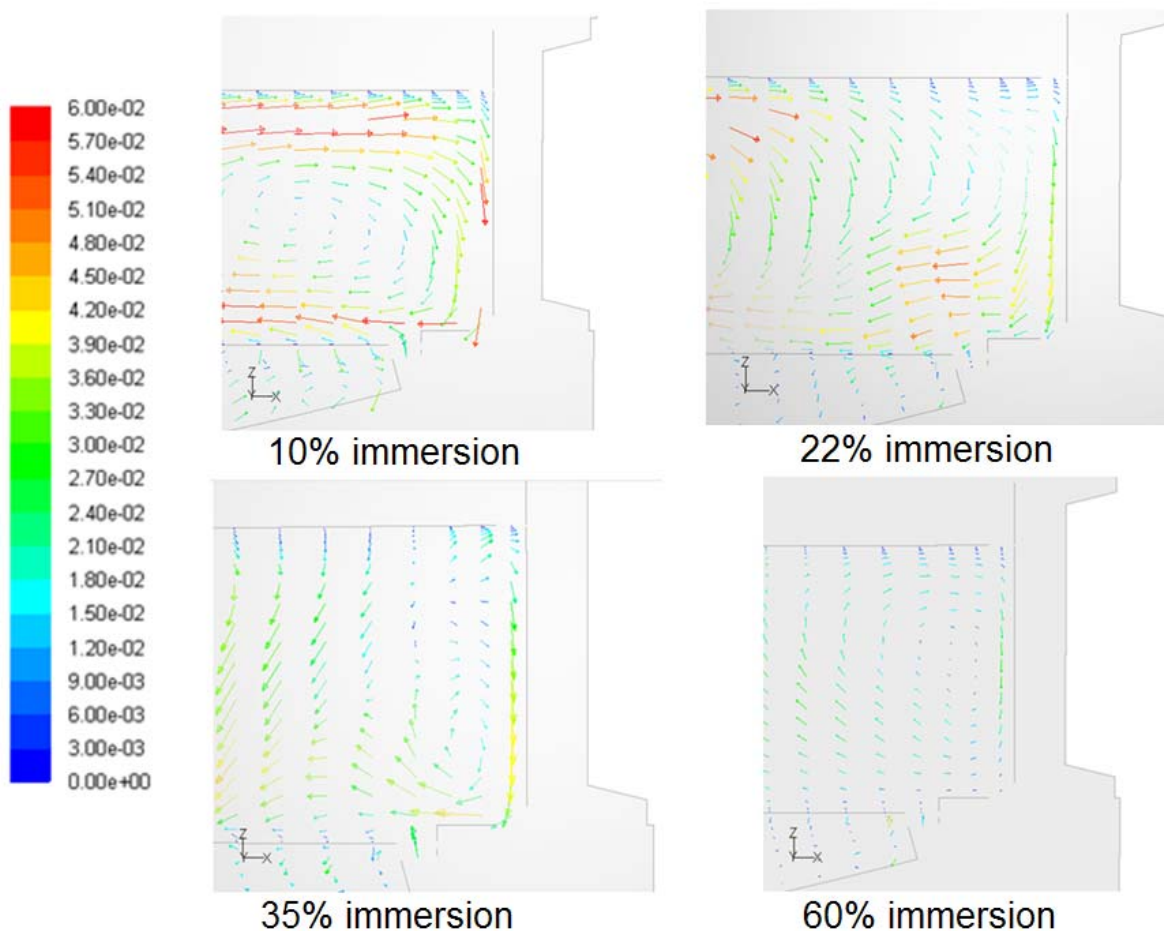


Figure 4.29: Velocity vectors at different immersion depths at the copper sidewall. The velocity vectors decrease in size as the electrode immersion increases.

Based on these observations the conclusion is therefore drawn that the electrode immersion depth greatly affects the stirring of the slag in the immediate vicinity of the electrode, but temperature (which determines the natural buoyancy) has a bigger influence on the stirring of the slag towards the middle and sidewall of the slag bath.

4.9.2 Electrode tip shape and current distribution at the tip

This model, as well as the model developed by Sheng *et al.* (1998b), assumes the electrodes to be cylinders with flat ends at the bottom. Although it is known from practical experience that this assumption is valid at shallow immersion depths, it is not the case at

deeper immersions where the electrode tip will resemble a pencil tip. It is further assumed that the electrode current density is distributed evenly around the area of the electrode immersed in the slag. This section, therefore, researches the sensitivity of the model towards these two assumptions.

The shape of the electrode tip has been modified for the 60% immersion model. The assumption is also made here that 80% of the current flow through the bottom section of the electrode and only 20% of the current flow through the sides of the electrode immersed in the slag. The true distribution of the current density on the tip of the electrode is, however, unknown and further research into the current flow through the electrode is therefore required if it does have a significant impact on the model results. The current boundary conditions are specified according to Figure 4.30.

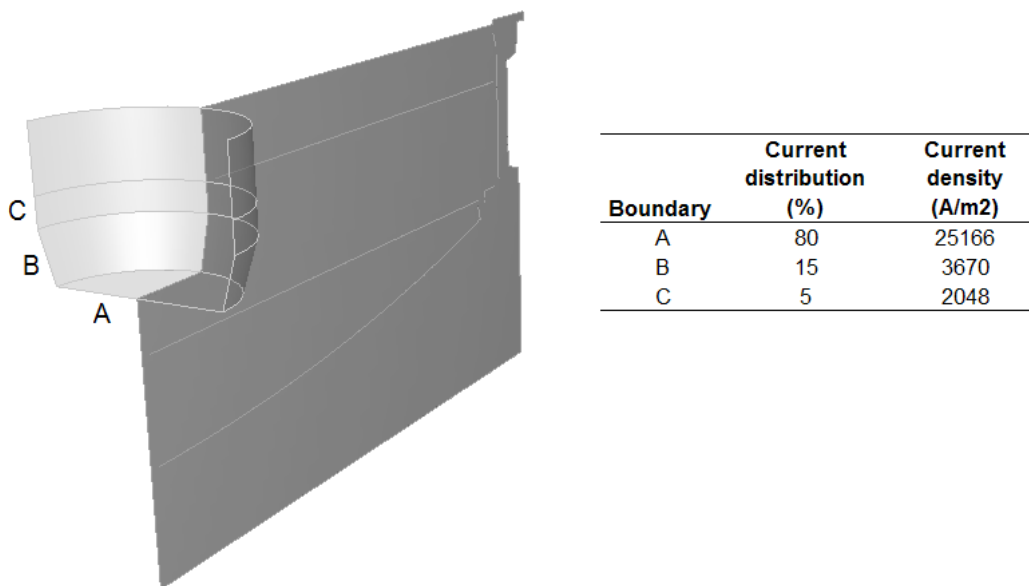


Figure 4.30: Pencil shaped electrode tip with 80% of the current flowing through the tip of the electrode and not evenly distributed as per the original assumption.

The sensitivity of the model to the shape of the electrode and the current density at the tip of the electrode are determined by comparing schematically the results for the current density and voltage profiles and the power distribution. Figure 4.31 shows the current density profiles for the original 60% electrode immersion compared to the adapted 60% electrode immersion model.

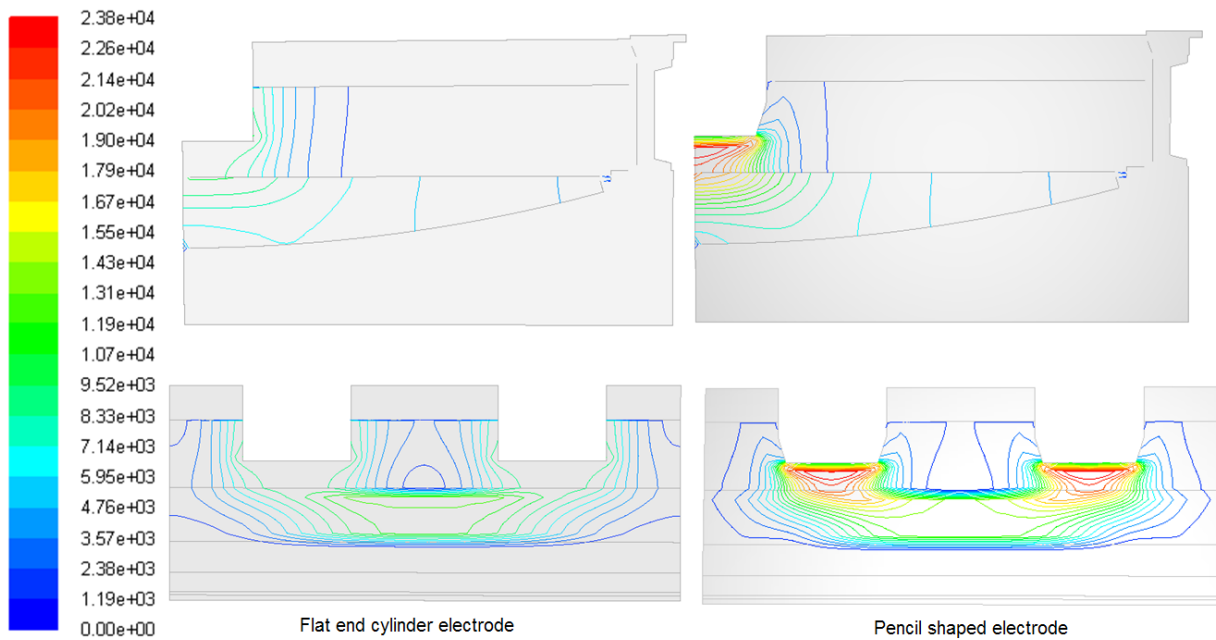


Figure 4.31: Comparison of the current density profiles between the flat end cylinder type electrode and the pencil shaped electrode with current flowing through the tip. The current density is significantly higher around the tip of the electrodes in the second case.

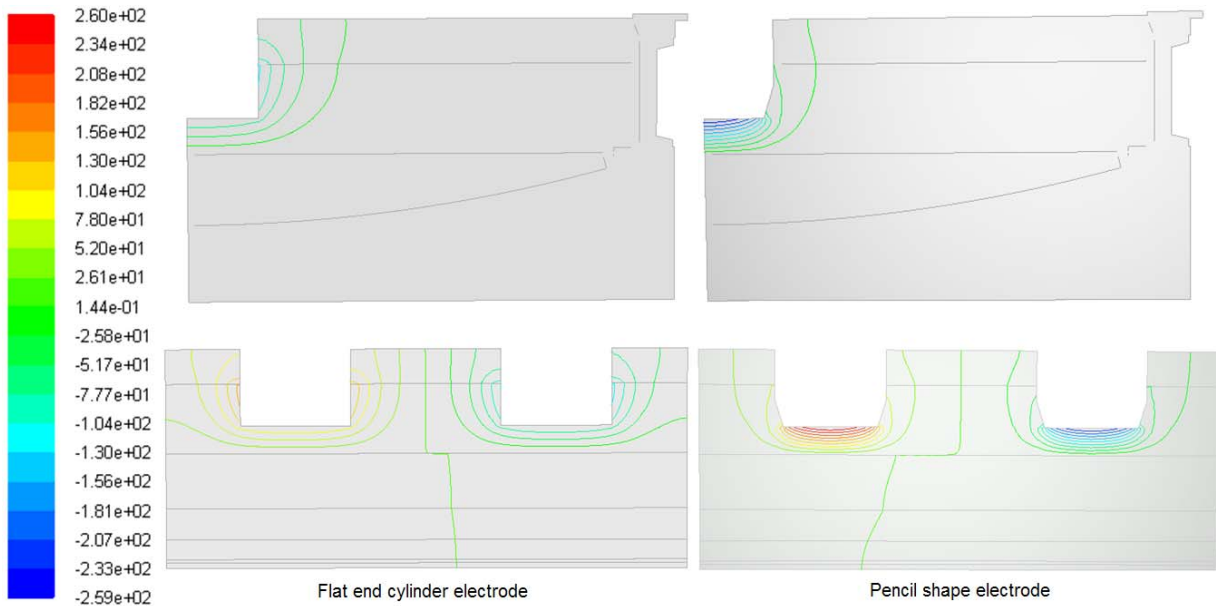


Figure 4.32: Comparison of the voltage profiles between the flat end cylinder type electrode and the pencil shaped electrode with current flowing mainly through the tip. The electrode tip voltage is significantly higher at the tip of the electrode for the second case.

The profiles for the voltage distribution and the joule heating are also compared and shown in Figure 4.32 and 4.33.

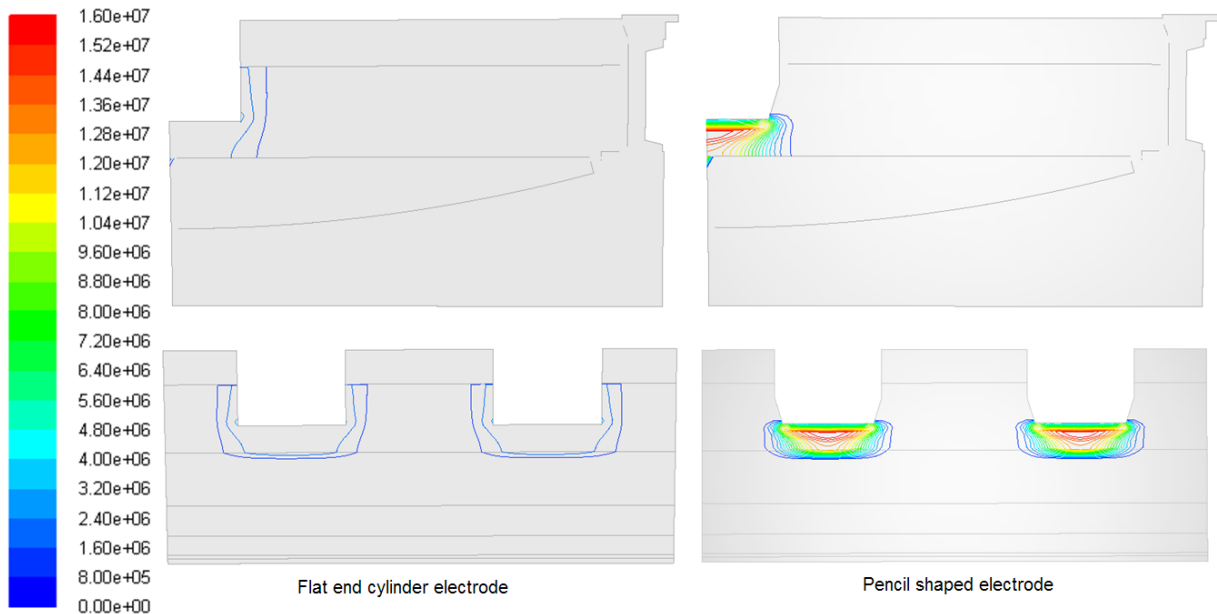


Figure 4.33: Comparison of the joule heating profiles between the flat end cylinder type electrode and the pencil shaped electrode with current flowing mainly through the tip. The second case shows significantly larger joule heating occurring at the tip of the electrodes.

From Figure 4.31 to 4.33 it can be clearly seen that the higher current density at the tip of the pencil shaped electrode affects the current, voltage and joule heating profiles dramatically.

Table 4.3 shows the difference in the total power distribution in the bath and the resulting average matte and slag temperature for the two cases. The higher current density of the second at the tip of the pencil shaped electrode causes the total power distribution to be higher in the matte and the slag, but lower in the concentrate with the more important figure of these three being the power distribution in the slag. The higher power in the slag and the matte now results in significantly higher temperatures of about 200 ° C in the matte and the slag.

Table 4.3: Comparison between the total power distribution in the bath and the resulting average temperatures for the two types of electrode cases.

	Flat end cylinder electrode	Pencil shaped electrode
Power distribution (MW)		
Slag	5.26	7.42
Matte	0.0084	0.0105
Concentrate	0.033	0.0056
Total	5.30	7.44
Average temperatures (°C)		
Slag	1463	1670
Matte	1411	1621

From these results it can therefore be concluded that the model is very sensitive to the shape of the electrode and boundary condition of the current density on the tip of the electrode. It is therefore recommended that a study be done in order to determine the accurate boundary conditions for the current density on the tip of the electrode or the preferred path of current through the electrode when immersed into a slag-like material.

Chapter 5

CONCLUSION

5.1 Model conclusion

A CFD model for a six-in-line matte melting furnace was developed in which the energy distribution, electrical and flow profiles are simulated. Attention has been given only to a slice of the six-in-line immersed electrode furnace containing two half electrodes or one half of a pair to simulate the current flow between the electrodes.

Specific attention was given to the energy balance in the slice to ensure that the model energy input, heat sinks and shell losses can be compared to furnace data. A user sub-model was developed for the heat-up and melting of concentrate, as well as for the heat required to heat the particles from the melting temperature up to the bath temperature. Intermediate results show that model energy input to be slightly less than what furnace data suggest, which then result in slightly lower calculated average temperatures for the slag and the matte. The shell losses show a good agreement between computed values and furnace data. To ensure that the energy generation stays at a constant value at a desired value determined by the modeller, a constant value for the electrical conductivity needs to be used. The correct energy generation is therefore determined on a trial and error basis and for more accurate results; proper validation of the voltage profiles of the Polokwane furnace should take place. For comparative results between different furnace scenarios, this method will already be valuable, even without detailed validation.

Three dimensional results for the current, voltage and energy distributions have been developed. These results compare very well with the profiles developed by Sheng, Irons and Tisdale in 1998 in their CFD modelling of a six-in-line furnace. It was found the current flow mainly takes place through the matte, even with an electrode depth of only 20% immersion in the slag, but the voltage drop and energy distribution still only takes place in the slag.

Temperature profiles through-out the entire modelling domain were established. The vertical temperature profile similar to Sheng *et al.* (1998b) was obtained, which shows a specifically good comparison to the measured temperature data from the Falconbridge operated six-in-line furnace. The temperature in the matte and the slag was found to be uniform, especially in the vertical direction.

The energy balance for the model was compared to plant operating data and found to be slightly lower than the actual data. This can easily be adjusted in the model, but it is recommended that proper validation and furnace measurements should commence first to establish the more accurate boundary conditions. An initial heat distribution shows that 99% of the energy generated through joule heating, is generated in the slag and 67% of this energy is consumed through the heat-up and melting of the concentrate. 18% is to heat-up the slag with 14% shell losses.

It has been found that similar results with Sheng *et al.* (1998b) are obtained for the slag and matte velocity vectors. It is also interesting to note that very similar results for the velocity vectors are obtained with Jardy *et al.* in his calculation of the velocity vectors in a circular furnace. Boiling has been observed around the electrodes which can hardly be conducive to downward flow directions around the electrode, but as two different independent researches, using different methods, calculated similar results, it may be worthwhile investigating further.

The impact of the bubble formation on the slag flow was investigated and found to be a significant contributor to the flow. With the bubble formation, it is shown that possible 'dead zones' in the flow with a distinctive V-shape can develop at the sidewalls of the furnace with the V pointing towards the centre of the electrode. This behaviour can have a significant impact on the point of feed to the furnace and indirectly affect the feed rate as well as the settling of the slag and matte. This might also be the explanation as to why the bath temperatures dropped significantly when the furnace concentrate feed ports were moved closer to the electrodes. These results were however obtained when the matte was modelled as a solid layer and might therefore change when the matte flow starts impacting on the slag flow. This effect is not as clearly visible when the matte modelled as a liquid layer. Validation of these results is therefore important.

Different electrode immersions were modelled with a constant electrical current input to the different models and it was found that the electrode immersion depth greatly affects the stirring of the slag in the immediate vicinity of the electrode, but temperature (which determine the natural buoyancy) has a bigger influence on the stirring of the slag towards the middle and sidewall of the slag bath.

The sensitivity of the model to a different electrode tip shape with current flow concentrated at the tip of the electrode was also modelled and it was found that the electrode shape and electrical current boundary conditions are very important factors, which greatly affect the voltage, current density and temperature profiles through the matte and the slag.

The CFD simulation with the commercial PC – based package, Fluent has proved to be a useful tool in modelling the electrical, flow and temperature profiles in the six-in-line furnace. Even with results that don't reflect the reality 100%, this type of simulations can be used to test different furnace scenarios easily in a safe and cost effective way and the results used for comparative purposes for example in terms of whether flow rates increase or not, how the energy distribution change with electrode movements as well as heat transfer from the matte to the slag with different slag and matte levels. A large amount of information can be generated in this way and the understanding of the process will be enhanced.

5.2 Conclusion on MSc Objectives

The following objectives have been achieved:

- A CFD model for the Polokwane matte tapping channel was developed which included a complex geometry and mesh solution with basic fluid flow and heat transfer calculations. A paper was published and presented on this topic for the 5th International CFD conference in Melbourne Australia 2006¹. Paper in appendix (pp 118 -123)
- A prototype CFD model for a six-in-line matte melting furnace was developed in which the energy distribution, electrical and flow profiles were simulated.
- A user sub-model was developed for the heat-up and melting of concentrate, as well as for the heat required for heating the particles from the melting temperature up to the bath temperature. These user sub-models can still, however, be refined to improve in accuracy.
- The current results for the voltage, vertical temperature profile through the matte and slag and velocity profiles in the matte and slag show a good agreement with the information found in literature. The total shell losses calculated show a good agreement with the data obtained from furnace operation.

¹ Snyders, C.A., Eksteen, J.J. and Moshokwa, A., Matte Tap Channel Model, 5th International Conference on CFD in the Process Industries, CSIRO, Melbourne, 13-15 December 2006

It can be concluded that objectives set out for the MSc (Eng) level were reached and completed, and have been presented². During the study a number of key assumptions were made, each of which requires further study at a more advanced level in order to increase understanding make a significant contribution to knowledge in the field.

Although modelling different electrode immersions was not part of the M.Sc objectives, a significant start has been made by modelling at four different electrode immersions with constant current through each of the models. The temperature, power and velocity outputs were compared and conclusions made. The sensitivity of the results to the electrode tip shape at deep electrode immersions was also researched and found to be significant. This also was completed as an addition to the M.Sc objectives.

² Snyders, C.A. and Eksteen, J.J., Development of a CFD Model for Six in Line Furnaces, Mineral Processing 2007, SAIMM Mineral Processing Conference, Cape Town, 2-3 August, 2007

Chapter 6

RECOMMENDATIONS

Several recommendations arose from this modelling work carried out in this investigation. Time constraints, however, did not allow for the additional work to be carried out and although valuable results were obtained, it is deemed to be a necessity if more in-depth understanding of furnace behaviour is to be obtained.

- Validation of the results. Although the results obtained so far are in agreement with literature data, as well as measured data from other plants, a validation campaign is recommended to ensure that the results obtained can be compared to the actual data from the Polokwane furnace. Validation is also required for the voltage profiles. A trial and error method was used to determine the energy generation for the model, which result in a certain voltage profile around the electrode. These voltages should be validated to ensure that the energy input assumed for the model is indeed correct.
- Magneto hydrodynamic effects. It has been generally accepted that the contribution of the MHD effects to the flow in the slag is negligible compared to the buoyancy forces. While this may be true for the slag, no literature suggests that the MHD effects in the matte is also negligible or give any indication as to what it may be. It has clearly been shown in section 4.1 that the majority of the current flows through the matte and not the slag and may therefore impact directly on the matte flow and indirectly on the slag flow. To establish these forces in the matte, the assumed equivalent DC current for the model needs to be changed to AC current and the magnetic field generated by these currents needs to be entered as boundary conditions to enable the calculations of the Lorentz forces in the matte.
- Following the modelling at different electrode immersions with constant current flow through the bath, which resulted in lower power outputs with increasing electrode depths, these models should be adapted according the PVI diagram of

the furnace to achieve model results at different electrode immersions but with a constant power output.

- A detailed investigation to determine the electrode tip shape at different immersions, as well as the boundary conditions of the current density on the tip of the electrode, is necessary as it proven that the model is quite sensitive to these conditions.

Chapter 7

PAPERS WRITTEN

MATTE TAP CHANNEL MODEL

CA. Snyders¹, JJ Eksteen², A. Moshokwa

Fifth International Conference on CFD in the Process Industries

CSIRO, Melbourne, Australia

13-15 December 2006

This paper includes the CFD model of the Polokwane furnace tap channel showing the temperature profiles as well as the factors determining the matte tap rates.

DEVELOPMENT OF A CFD MODEL FOR SIX IN LINE FURNACES

CA. Snyders¹, JJ Eksteen²

South African Institute of Mining and Metallurgy Mineral Processing 2007-08-29

Cape town South Africa

2-3 Aug 2007

Describes the development and the assumptions made for the CFD model of the Polokwane six-in-line furnace

Chapter 8

REFERENCES

Adema A.T, *Development of a CFD model for a phosphorous producing submerged arc furnace*, December 2005, T.U Delft

Anderson J.D, *Computational Fluid Dynamics, The basics with applications*, McGraw-Hill Inc. 1995

Barth O, *Electric smelting of Sulfide Ores*, Extractive Metallurgy (based on A.I.M.E. Symposium, Feb. 1960), Interscience , New York 1961, pp 241 – 262.

Berryman R.A, Ham F.E, *Challenges in electric furnace smelting of nickel*. The Brimacombe Memorial Symposium, Oct 2000, pp 381 - 396

Boulet B, Vaculik V, Wong G, *Control of Non-Ferrous electric arc furnaces*, IEEE Canadian review, 1997

Channon. W.P, Urquhart R.C, Howat D.D, *The mode of current transfer between electrode and slag in the submerged arc-furnace*, Journal of the South African Institute of Mining and Metallurgy, August 1974, pp 4 – 7

Cloete S, *Computational Fluid Dynamics Simulation of gas induced flow patterns in an argon oxygen decarburization vessel*, Final year project, 2006

Davidson P.A, *An Introduction to Magnetohydrodynamics*

Dosa G, Kepes A, Ma T, *Computer Control of high power electric furnaces*, Hatch report

Eric R.H, *Slag properties and design issues pertinent to smelting electric furnaces*. The journal of the South African Institute of Mining and Metallurgy. October 2004, pp 499 - 510

Eric R.H, Hejja A.A, *Dimensioning, scale-up and operating considerations for six electrode electric furnaces part 1: Current and heat flow in the slag*. EPD Congress 1995, The Minerals, Metals & Materials Society, 1995, pp223 – 238

Eric R.H, Hejja A.A, *Dimensioning, scale-up and operating considerations for six electrode electric furnaces part 2: Design and scale-up considerations for furnaces treating PGM-containing copper-nickel concentrates*. EPD Congress 1995, The Minerals, Metals & Materials Society, 1995, pp238 - 257

Fluent 6.2, *User's Guide January 2005*

Gunnawiek L.H, Tullis S, *Prediction of Heat and fluid flow in the slag phase of an electric arc reduction furnace*, Computational fluid dynamics and heat/mass transfer modelling in the metallurgical industry, The metallurgical society of the Canadian institute of mining, metallurgy and petroleum, 1996, pp 250 - 264

Gunnawiek L.H, Oshinowo L, Plikas T, Haywood R, *The application of numerical modeling to the design of electric furnaces*, Tenth International Ferroalloys Congress; INFACON X: Transformation through Technology. Cape Town, South Africa, February 2004, pp 555 - 564

Hadley T.D, Kritzinger H.P, McDougall I, Prinsloo E, Van Vuuren D.S, *Assessment of Polokwane Furnace cooler failure*, CSIR South Africa, April 2006

Hejja A.A, Eric R.H, *Flow and settling phenomena in matte smelting electric furnaces*, EPD Congress 1996, The Minerals, Metals & Materials Society, 1995, pp 27 – 41.

Hundermark R, *The Electrical Conductivity of Melter Type Slags*. Masters of Science thesis, University of Capetown, 2003

Hundermark R, De Villiers L.P.S, Ndlovu J, *Process Description and short history of Polokwane Smelter*, South African Pyrometallurgy 2006, Johannesburg, March 2006, pp.35-41

Incropera F.P, DeWitt D.P, *Fundamentals of Heat and Mass transfer, Fourth Edition*, 1996, Chapter 7, pp 345 - 418

Ma T, Bendzsak G.J, Perkins M, *Power system design for high-power electric smelting and melting furnaces*, Hatch report

Matyas A.G, Francki R.C, Donaldson K.M, Wasmund B, *Application of new technology in the design of high-power electric smelting furnaces*, Metallurgy, CIM bulletin volume 86 No 972, Jul – Au 1993, pp 92 -99

Mostert J.C, Roberts P.N, *Electric Smelting at Rustenburg Platinum Mines Limited of nickel-copper concentrates containing platinum-group metals*, Journal of the South African institute of Mining and Metallurgy, April 1973, pp 290 - 299

Nelson L.R, Stober F, Ndlovu J, De Villiers L.P.S, Wanblad D, *Role of technical innovation on production delivery at Polokwane Smelter*, Nickel and Cobalt 2005: Challenges in Extraction and Production, 44th Annual Conference of Metallurgists, Calgary, Alberta, Canada, Aug 2005, pp.91-116

Rennie M.S, Howat D.D, Jochens P.R, *The effects of Chromium oxide, iron oxide and calcium oxide on the liquids temperatures, viscosities and electrical conductivities of slags in the system MgO-Al₂O₃-SiO₂*, Journal of South African Mining and Metallurgy, August 1972, pp 1-9

Reuter M.A, Yang Y, *Modelling and Control of Metallurgical Reactors*. Delft University of Technology, April 2000

Scheepers. E, Yang. Y, Reuter. M.A, Adema A.T, *The development of process model of a submerged arc furnace for phosphorus production*, Fifth International Conference on CFD in the Process Industries, CSIRO, Melbourne, Australia, December 2006, CD-ROM

Sheng Y.Y, Irons G.A, D, Tisdale D.G, *Transport Phenomena in Electric Smelting of Nickel Matte Part 1: Electric Potential*, Metallurgical and Materials Transactions B Volume 29B, February 1998, pp 77 - 83

Sheng Y.Y, Irons G.A, D, Tisdale D.G, *Transport Phenomena in Electric Smelting of Nickel Matte Part 2: Mathematical Modeling*, Metallurgical and Materials Transactions B Volume 29B, February 1998, pp 85 - 94

Utigard T.A, *Heat and mass transfer in non-ferrous smelting furnaces*, The Brimacombe Memorial Symposium, October 2000, pp 519 - 534

Vaisburd. S, Brandon D.G, *A combined unit for viscosity, surface tension and density measurements in oxide melts*. Measurement science and technology, vol 8 nr 7, 1997, pp 822 – 826

Vereeninging refractories (Pty) Limited, *D60/100 HD*, F1645/12/2005

Vereeninging refractories (Pty) Limited, *VR 99 C*, F1607/7/2005

Vereeninging refractories (Pty) Limited, *A5*, F1557/6/2005

Vereeninging refractories (Pty) Limited, *Verotar 95*, F1634/11/2005

Vereeninging refractories (Pty) Limited, *MAG B2 HR*, F1635/11/2005

Yang. Y, *Computer simulation of gas flow and heat transfer in waste heat boilers of the Outokumpu copper flash smelting process*, Doctoral thesis, Acta Polytechnica Scandinavica, Chemical Technology Series No. 242, Helsinki 1996, 135 pp

Yesilata. B, *Viscous heating effects in viscoelastic flow between rotating parallel-disks*, Department of Mechanical Engineering, Harran University, Saliurfa-Turkey, Turkish J. Eng. Env. Sci. 26 (2002), pp 503 - 511

APPENDIX

Material Properties

Furnace refractories

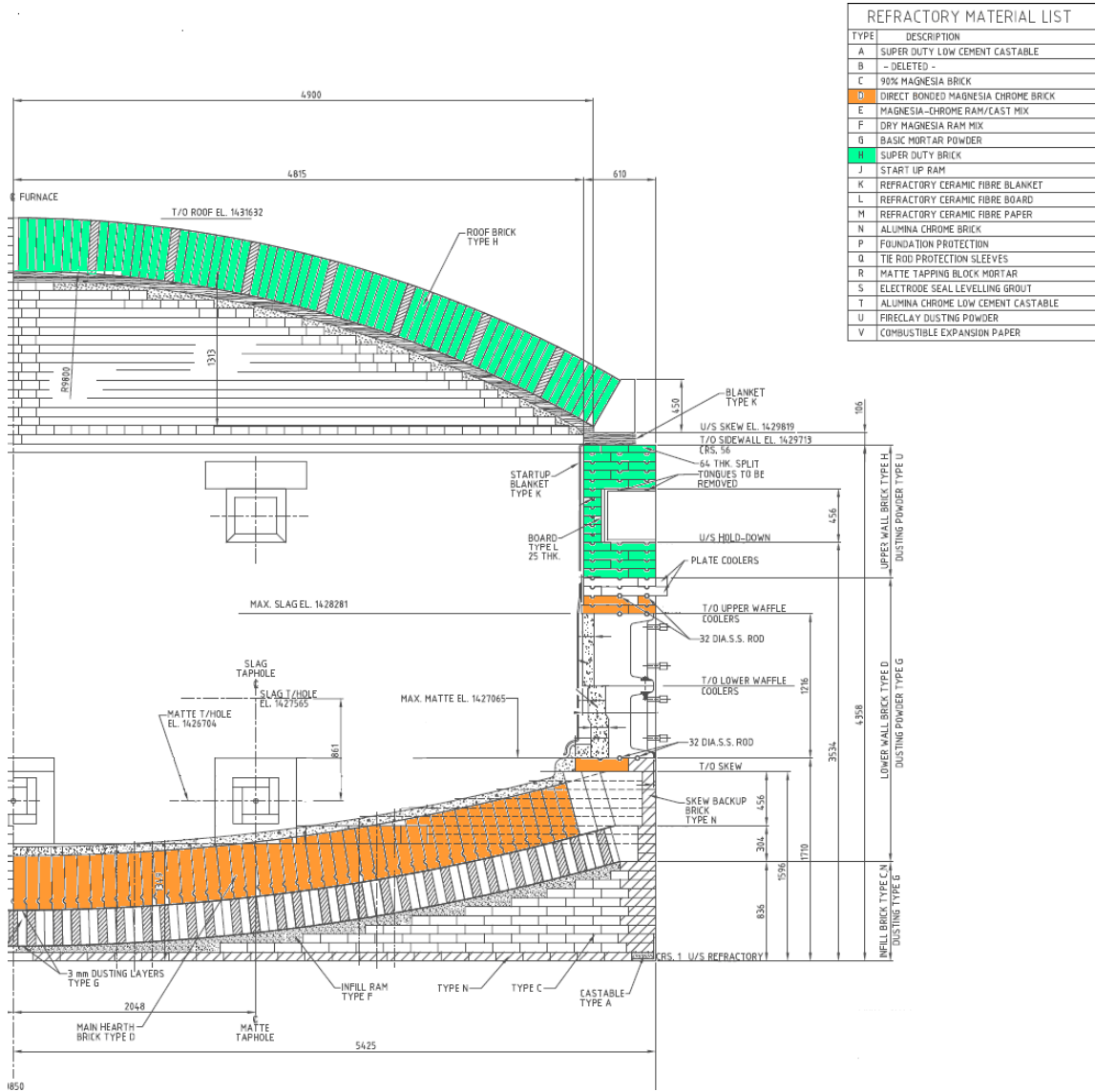


Figure a: Furnace materials detail showing the refractory used for all the different sections of the furnace.

Refractory composition (%)

	Type				
	C	D	F	H	N
SiO ₂	2,8	1,6	0,8	52,2	0,4
Al ₂ O ₃	1,0	7,2	0,3	44,0	90,0
Fe ₂ O ₃	1,0	10,2	0,8	1,3	0,1
CaO	1,7	1,0	2,4		0,1
MgO	93,0	59,3	95,5		0,1
CaO + MgO				0,4	
Cr ₂ O ₃		20,5			9,0
TiO ₂				1,6	0,1
Alks				0,5	0,2

Physical properties of refractories

	Units	Type				
		C	D	F	H	N
PCE Orton Cone		36	36		32	40
Temperature Equivalent	°C	1810	1810			
Apparent Porosity	%	15	14		15	19
Bulk Density	kg/m ³	2940	3280	2860	2350	3100
Apparent Specific Gravity		3.46	3.83		2.76	3.83
Cold Crushing Strength	MPa	50	50	30	45	80
Modulus of Rupture	MPa					
@ room temperature		15	7		7	20
@ 1260°C		7				
@ 1400°C			6		4	8.5
Permanent Linear Change	%					
2 hrs @ 1400°C					-0.651	
2 hrs @ 1600°C						0
2 hrs @ 1700°C		-0.2	0.1			
Fired to 1000°C				4.1		
Fired to 1600°C				2.3		
Thermal Conductivity	W/mK					
@ 500°C		7	2.3			
@ 1000°C		4.1	2.6	1.8	1.2	2.7
@ 1500°C		2.3	2.9			
Specific Heat	kJ/kgK	0.96	0.88	1.31		
Thermal Expansion	%					
20-1000°C		1.3-1.4	1		0.6	0.7
@ 1400°C						1
Spalling Resistance (BS1902)		Excellent	Excellent		Good	Excellent
Iron Oxide Bursting (BS1902)	%	Nil	0.5			
Maximum Service Temperature	°C			1800		
Maximum Particle Size	mm			4		
Mass Required	kg/m ³			2910		
Resistance to CO attack (ASTM C288-87)					Excellent	
Permeability (cgs)						0.02

Type C – Mag B2 HR

A hydration resistant fired magnesia brick

For use in the sidewalls of large reverberatory furnaces and submerged-arc furnaces. This brick has excellent hydration resistance.

Type D – D60/100HD

A re-constituted fused grain magchrome brick

This brick is prepared from fused mixtures of high purity magnesia and low silica washed chromites, giving maximum direct bonding within the grain. For use in EAF hot spots, AOD vessels, vacuum degasser linings and CLU converters.

Type F – Verotar95

Tar bonded magnesia ramming material

A tar bonded ramming material based on high quality magnesia. For use in electric arc furnace hearths, ladle backing ramming, patching of basic ladles etc

Type H – A5

A 44% alumina dry pressed firebrick.

Dense CO-resistant firebrick designed for use in blast furnace stacks. Other applications include Cu, Ni, Pt electric reverb side walls.

Type N - VR 99 C

Chrome enriched alumina brick

A direct bonded high purity brick. The Cr_2O_3 content makes it suitable for places where high abrasion occurs. It is used in the chemical industry carbon black and cyanide reactors.

Copper properties

Physical Properties of Copper

Physical Property	Unit	Value
Density	kg/m ³	8978
Cp	J/kgK	381
Thermal		
Conductivity	W/mK	387.6
Electrical		
Conductivity	1/ohmm	5.80E+07
Magnetic		
Permeability	h/m	1.26E-06

*Data from the Fluent database

Carbon monoxide properties

CO gas properties

Physical Property	Unit	Value
Density	kg/m ³	1.1233
Cp	J/kgK	1043
Thermal Conductivity	W/mK	0.025
Viscosity	kg/ms	1.75E-05
Molecular Weight	kg/kgmol	28.01055
Standard State		-
Enthalpy	J/kgmol	1.10E+08
Standard State Entropy	J/kgmolK	1.98E+05
Reference Temperature	K	289.15
Adsorption Coefficient	1/m	0.17

*Data from the Fluent database

Concentrate

Thermal conductivity: 1.2 W/Mk

Electrical conductivity: 1.2 S/m

*Data from Hadley et al.

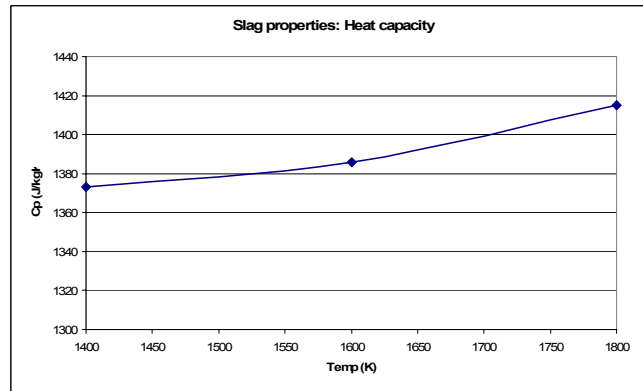
Heat Capacity: 1726 J/kgK (as calculated from Figure 3.13)

Density: 1450 kg/m³

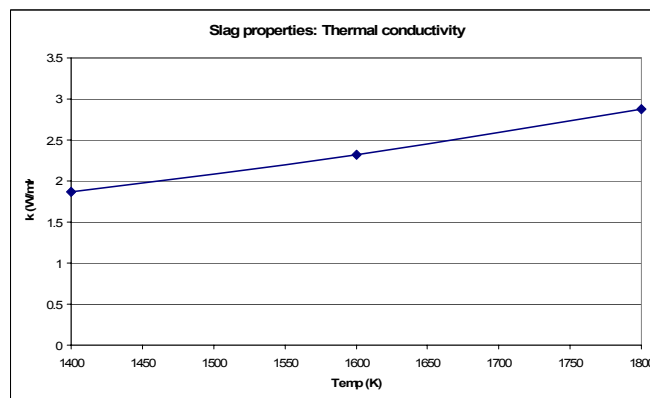
Slag

The data shown in the tables are for all the data available and the data shown in the Figures are the data from the table that were used in the simulations.

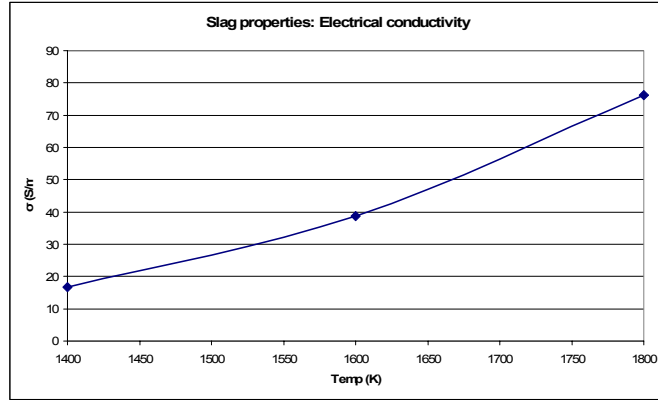
Slag	
Temp	Cp
deg C	J/kgK
400	1063
600	1117
800	1167
1000	1211
1200	1250
1400	1373
1600	1386
1800	1415



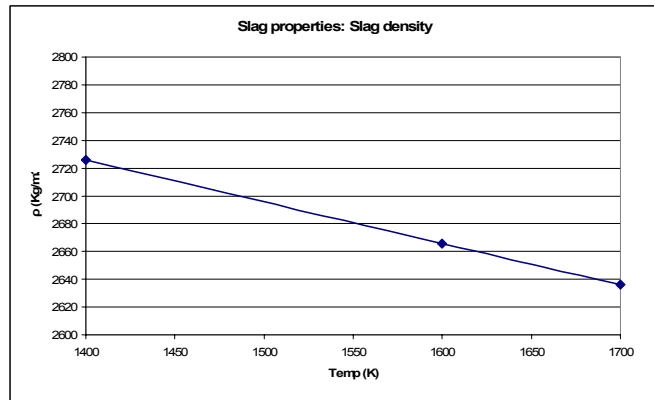
Slag	
Temp	k
deg C	W/mK
400	0.813
600	0.9
800	1.037
1000	1.235
1200	1.507
1400	1.864
1600	2.317
1800	2.878



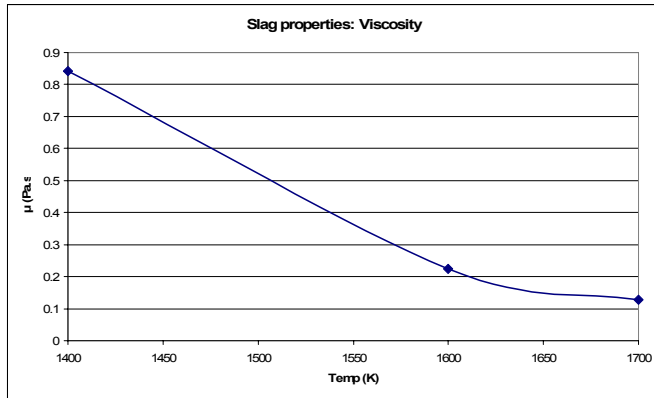
Slag	
Temp	σ
deg C	S/m
400	0.001
600	0.01
800	0.21
1000	1.42
1200	5.77
1400	16.75
1600	38.75
1800	76.24



Slag	
Temp	ρ
deg C	Kg/m ³
300	3056
500	2996
900	2876
1000	2846
1200	2786
1400	2726
1600	2666
1700	2636



Slag	
Temp	μ
deg C	Pa.s
300	
500	
900	
1000	41.57
1200	4.54
1400	0.842
1600	0.224
1700	0.128

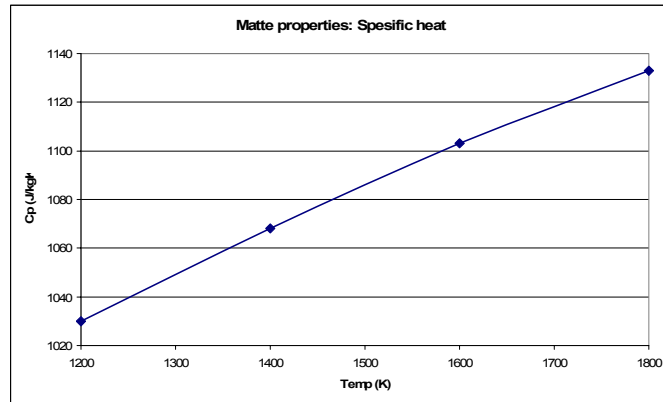


Matte

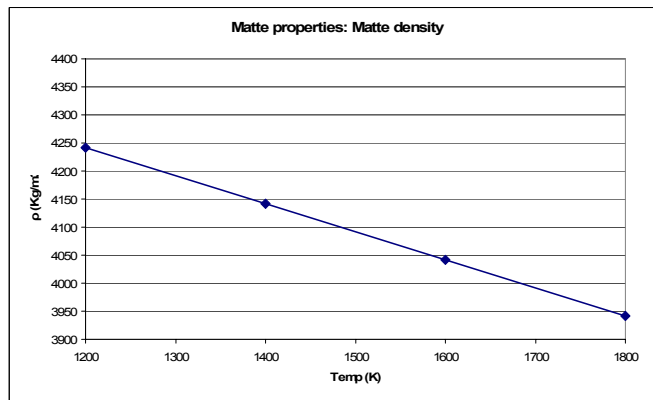
Thermal conductivity: 17 W/Mk

Electrical conductivity: 9.3e4 S/m

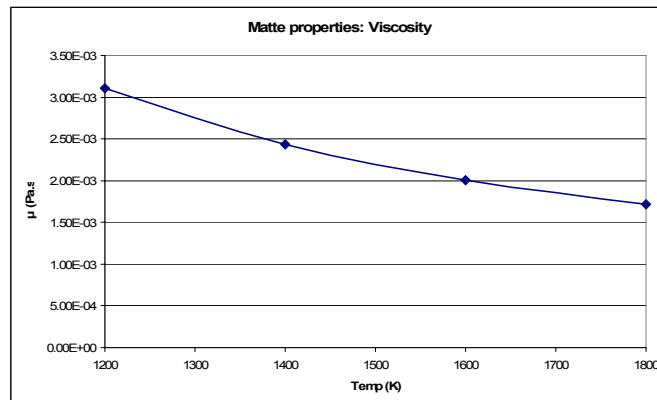
Matte	
Temp	Cp
deg C	J/kgK
500	837
600	886
800	938
1000	986
1200	1030
1400	1068
1600	1103
1800	1133



Matte	
Temp	ρ
deg C	Kg/m ³
400	
600	
800	
1000	4342
1200	4242
1400	4142
1600	4042
1800	3942



Matte	
Temp	μ
deg C	Pa.s
400	
600	
800	
1000	
1200	3.11E-03
1400	2.43E-03
1600	2.01E-03
1800	1.72E-03



User defined code

```

/*****
/* UDF FOR THE POLOKWANE FURNACE -TAKE 2 */
*****/

#include"udf.h"          /*header file describing macro*/
#define W -6.05e-5      /*velocity of concentrate moving down*/
#define DENSITY 1100   /*density of concentrate*/
#define m_slag 3        /*mass flowrate of new slag*/
#define BATH_ID 12     /*ID of the fluid zone as in the boundary condition*/

real tavg;

/* Calcualte average temperature */

DEFINE_ADJUST(average_temp,d)
{
  Thread *t;
  cell_t c;
  real volume, temp, vol_tot;

  t = Lookup_Thread(d, BATH_ID);
  tavg = 0;
  begin_c_loop(c,t)
  {
    volume = C_VOLUME(c,t); /* get cell volume */
    temp = C_T(c,t);        /* get cell temperature */
    vol_tot += volume;
    tavg += temp*volume;
  }
  end_c_loop(c,t)

  tavg /= vol_tot;

  Message("\n Tavg = %g\n",tavg);
}

/* Energy sink in the concentrate*/

DEFINE_SOURCE(concentrate_sink,c,t,dS,eqn)
{
  real heat_sink,cp_conc,h; /*Declaration of varaibles*/
  real temp = C_T(c,t);    /*Declaration of temperature*/
  real x[ND_ND];           /*matrix to be used*/

  C_CENTROID(x,c,t);

```

```

h=x[2];          /*z coordinate defined as h for height*/

if (temp<1073)
{
    cp_conc=1068;
}
else
{
    cp_conc=1133;
}

if (C_T_RG(c,t)[2]<=0)          /*if the temperature gradient is negative statement*/

{
    heat_sink=-((cp_conc)*DENSITY*C_T_RG(c,t)[2]*W);  /*calculation of heat sink*/
}
else
{
    heat_sink=0;      /*if the gradient is positive then there is no heat sink*/
}

C_UDMI(c,t,42)=cp_conc;
C_UDMI(c,t,43)=heat_sink;
C_UDMI(c,t,44)=C_T_RG(c,t)[2];

return heat_sink;

}

/*Energy sink for heating of the slag to operating temperature*/

DEFINE_SOURCE(slag_sink,c,t,dS,eqn)
{
    real energy_sink,cp_slag;      /*Declaration of variables*/
    real temp = C_T(c,t);          /*Declaration of temperature*/

    cp_slag=1373;                  /*cp of slag used in calculation*/

    if (temp>1573)                  /*Assume above 1300degC everything is in the slag zone*/
    {
        energy_sink=-((m_slag)*cp_slag*(tavg-1573))/37.16331;  /*calculation for
                                                                    heating up incoming slag*/
    }

}

else
{

```

```
    energy_sink=0;      /*under 1300degC is heated up in the conc*/  
}  
C_UDMI(c,t,45)=energy_sink;  
return energy_sink;  
}
```

THE POLOKWANE SMELTER MATTE TAP CHANNEL MODEL

CA. Snyders¹, JJ Eksteen², A. Moshokwa¹

1. Polokwane Metallurgical Complex, Anglo Platinum, Polokwane, South Africa,

E-mail: NSnyders@Angloplat.com

2. Department of Process Engineering, University of Stellenbosch, Private Bag X1, Matieland, 7602, South Africa,

E-mail: jeksteen@sun.ac.za

ABSTRACT

Key words: Tap channel, tap rate, heat transfer, platinum, furnace, refractory, matte

The 68 MW Anglo Platinum smelter has been designed with adequate transformer capacity and copper waffle coolers to allow for deep electrode immersion and higher heat fluxes to be able to treat concentrates with a chrome content of 4%. Nelson *et al.* 2005

With this high furnace intensity, matte temperatures of 1500°C and higher with the degree of superheat of about 650°C, can often be experienced due to various furnace conditions like uneven concentrate feeding and electrode immersion for example. These high matte temperatures cause severe erosion of the tapping modules (bricks) and can also be a critical safety factor if not properly managed.

The original tap block design consisted of the copper block with two water circuits for the cooling and 5 (230 x 230 x 114) mag-chrome tapping modules with magnesia surround bricks. After testing different materials, this design was then changed to a tap block with 3 water circuits and alumina-chrome tapping modules.

A 'bull nose' consisting of an extra water cooled copper block which extends outside the furnace wall was added and the complete tap channel now contains a total of 8 tapping modules. A CFD model for this complete unit has therefore been developed showing the thermal profiles in each section of the copper and refractory as well as the heating of the water. This model is used in conjunction with the 'Safeway' system currently being tested in the tapping channel and works like a thermocouple except it will measure the highest temperature over an area in the block and not just at one point.

These two measures provide excellent monitoring and management of the tapping channel and can assist in decision making around brick replacements and testing of different materials as well as a training tool to operators showing the impact of the different tapping conditions on the tap block.

BACKGROUND

The six-in-line furnace of Hatch design at Polokwane smelter is the largest capacity furnace in the platinum industry and as is rated at 68 MW (168 MVA). The electrical supply to the furnace is via six Soderberg 1.6m diameter electrodes and three single-phase 56 MVA transformers. Electrode currents are in the region of 35-45 KA, and operating resistances of 8-12 mΩ with the

electrode immersion depths between 20% and 40%. Hundermark *et al.* 2006

These operating conditions result in high operating temperatures with slag normally between 1600 and 1700°C and matte between 1450 and 1550°C. Matte is tapped from the furnace through the brick-lined, water-cooled copper tap block. Due to these operating temperatures and often experienced high tap rates, the corrosive/erosive factor is high and greatly affects the availability of the tap holes due to replacements of the very costly tapping bricks.

The original tap block design only consisted of one copper block and a copper faceplate at the front with two water circuits and 6 tapping bricks. A third water circuit was later added. This design was then changed and the 'bull nose' which is an extra copper block with a top that can be taken off was added and the faceplate was split into two units, a faceplate and a copper insert.

Figure 1 show the tap channel.

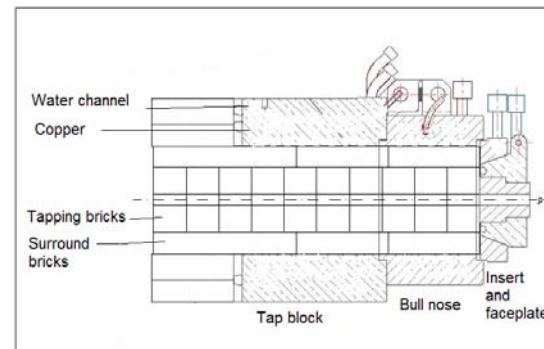


Figure 1: The tap block design

The CFD model using Fluent as CFD package was then used to evaluate the efficiency of the new design and determine the effect of the tap block on the matte flow as well as the effect of the matte flow on the refractory and copper units of the tap block. The tap rate is also of critical importance as it becomes difficult to close the tap hole at high tap rates, and the factors affecting the tap rate was therefore studied.

TAPPING BRICKS

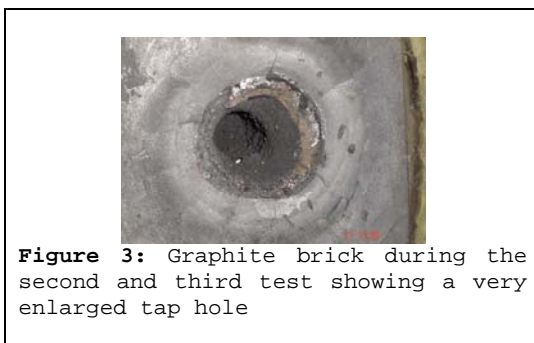
As the repair and maintenance of the tapping bricks are the major cause for the unavailability on the tap channel as well as a major cost contributor, various tapping bricks were tested to find the optimum tapping brick.

Two types of bricks, Alumina-Chrome and Mag-chrome bricks were tested from two different suppliers. It was found that the Alumina-Chrome refractory performed better than the Mag-chrome refractory and comparing the bricks from the first supplier with the second supplier bricks, the second supplier bricks lasted on average for 210 taps before a full repair compared to 150 taps. The reason can mainly be contributed to the star cracking shape occurring in the bricks from the first supplier where matte could penetrate. The bricks from the second supplier contain zirconium which prevents the cracking. However, the Mag-chrome bricks from the first supplier out-performed the Mag-chrome bricks from the second supplier.

Silicone-carbide bricks were also tested but found to be inferior. The quality of the silicon-carbide bricks was questionable and the mode of failure was again thermal cracking.

GRAPHITE TAPPING BRICKS

Three tests were done using a graphite brick. In the first test, only one graphite brick was used as first brick in the tap channel. The first brick was replaced after 29 taps and only had one crack but with the tap hole still in good condition. (Figure 2). For the second test, the first and second bricks were graphite bricks but after twenty taps the tap hole was very much enlarged and was replaced immediately. The third test showed the same results after only one day's tapping. However no matte penetration was visible. (Figure 3)



Two lumps of the brick (sample 1 and 2) were submitted for chemical analysis. Estimated matte penetration, from these results, for sample 1 is 54 mass %, and for sample 2 it is 15 mass %. The apparent values are raised due to the large differences in the relative densities of carbon,

refractories, and matte – by volume, matte penetration is 38 % (sample 1) and 7 % (sample 2). The analysis showed that a refractory phase was also present which puts a question mark at the sampling method of the brick as the original brick consisted only of carbon. Andrews 2005

BULL NOSE

The main reason for the installation of the bull nose was to reduce the rate of erosion on tapping modules closer to the furnace and to extend the period prior to the eight block repair. See Figure 1.

The previous design only consisted of one copper tap block and a faceplate and contained only 6 (the sixth brick is halfway in the furnace) bricks. The schedule for replacing bricks was as follows:

- At 40 taps, the first two bricks were replaced,
- At 80 taps the first 4 bricks were replaced
- At 160 taps, six bricks were replaced.

After the installation of the bull nose, the schedule changed as follows:

- At 45 taps, the first three modules are replaced
- At 90 taps, the first six bricks are replaced
- At 190 taps, all 8 bricks are replaced

The amount of bricks changed during the previous design was 13 bricks compared to the 20 bricks with the bull nose. An extra 30 taps of 33 ton/tap or 990 ton more matte are tapped with the added bull nose before a major repair. This schedule is still in the process of optimization and can be extended.

CFD MODEL

The CFD model assumes that the heat generation in the model are only from the matte flowing through the channel at steady state.

It was assumed in this model that the water inlet conditions are the same and a general matte flow rate and temperature for the matte inlet was assumed as shown in Table 1 and 2. The k-ε turbulence model was used to model the matte and water. The Fluent user's guide was used as reference for the turbulence model.

Table 1: Inlet conditions for the tap block model

Boundary	Temperature (K)	Flow rate (m ³ /hr)	Flow Rate (ton/min)
Water inlet	313	6	0.1
Matte inlet	1743	14	1

Table 2: Boundary Conditions for the tap block model

	Boundary Condition	Reynolds number	Condition
Water flow	No-slip	83419	Turbulent
Matte flow	No-slip	235105	Turbulent
Outer walls	Adiabatic		

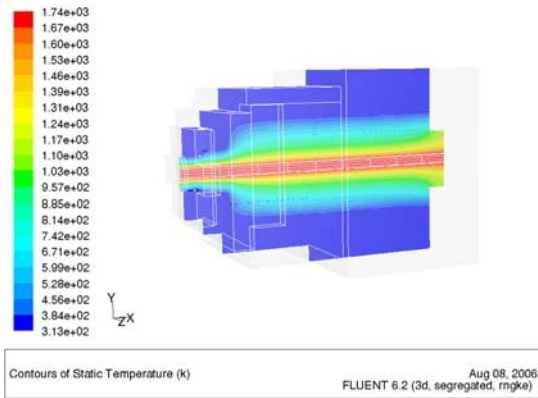


Figure 4: A cross section of the tap block showing the thermal profile in the block while tapping

Figure 4 show the thermal cross cut through the model. The main temperature drop occurs in the refractory. The reason for the decrease in the temperature rate change from the front of the tap channel towards the back is due to the copper being closer to the matte channel and the refractory at the front part are therefore less than at the back.

From Figure 5, it can also be seen that the heat fluxes in this front section of the block is higher than at the back.

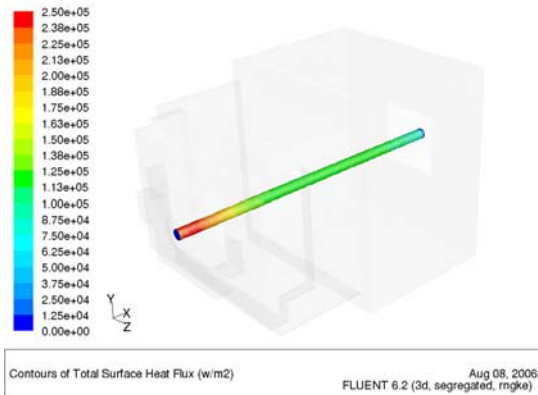


Figure 5: Heat flux distribution from the matte. Largest heat fluxes occurring around the front of the tap channel where the copper is closer to the matte.

It is therefore expected that the copper insert will show the highest copper temperatures of the tap block as it is the closest to the matte channel with the highest heat fluxes occurring in this region.

The water cooling of the copper is still very effective though as can be seen from the temperature profiles through the copper insert. The copper stays below 77°C as is shown in Figure 6.

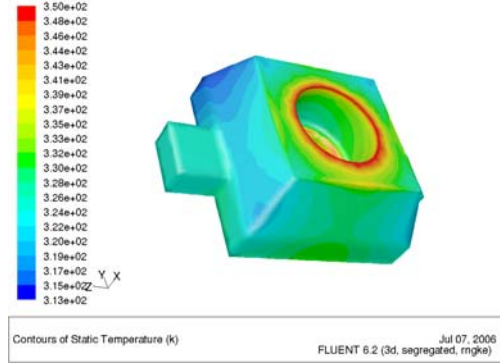
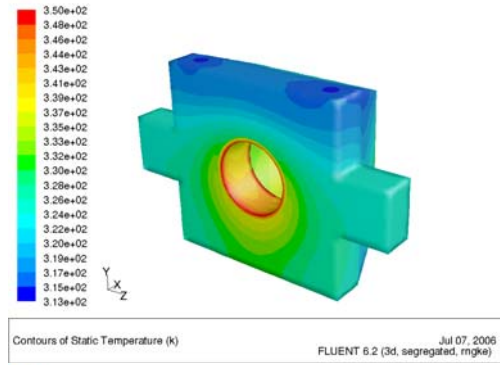


Figure 6: Thermal profile through the copper insert. Maximum temperature 77°C.

The difference in temperature between the first and the seventh tapping brick are shown in Figure 7.

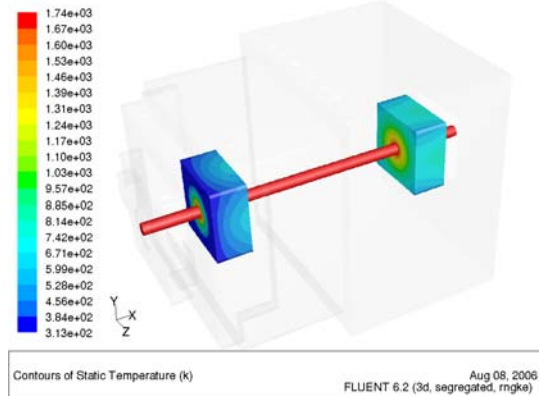


Figure 7: The first (left) and seventh tapping bricks thermal profiles showing the seventh tapping module at a much higher overall temperature.

The cooling of the matte as it flows through the channel can be seen in Figure 8. It is however seen that the cooling effect on the matte is very little and the average drop in temperature is only 2°C. Figure 8 show the temperature profile of the matte at the outlet with the temperature being at 1739K at the surface but still at 1743K at the centre. The matte inlet temperature was specified 1743K.

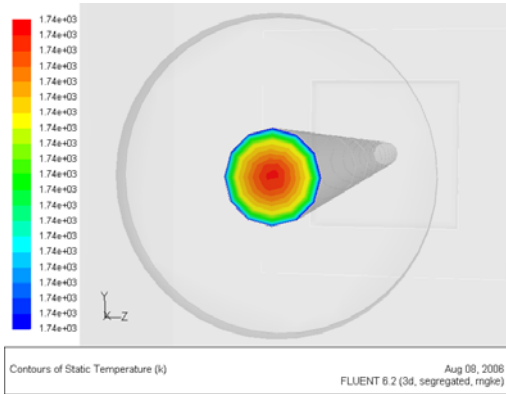


Figure 8: Temperature profiles of matte in the tap channel at the outlet.

TAPPING RATES

High matte flow rates are often the reason why brick replacements are done as high tap rates are often caused by the bricks being in a poor condition such as an increased tap hole diameter. It is therefore important to understand all the factors affecting the matte flow rate such as bath temperature, tap hole diameter and the hydrostatic head. The perception also exists at Polokwane Smelter that high matte temperatures are a reason for high tapping rates due to the changes in viscosity and density with temperature.

Based on the results from the previous CFD model, a simplified CFD model was used to simulate the flow through the tap channel to determine the effect of furnace bath levels (pressure) and the temperature of the matte on the tapping rate. The slight decrease in temperature shown in Figure 8 was assumed to be insignificant and the matte temperature was modelled as constant in the determination of the tapping rates.

The CFD model was specifically used instead of Torricelli's law, which states that the speed, v , of a liquid flowing under the force of gravity out of an opening in a tank is proportional jointly to the square root of the vertical distance, h , between the liquid surface and the centre of the opening and to the square root of twice the acceleration caused by gravity.

$$v = (2gh)^{1/2} \quad (1)$$

This doesn't take the viscosity and density differences of the fluid into account, whereas the CFD model does.

The data for viscosity and density for matte were taken from reference 4, who compiled these properties from various literature sources to ensure it reflects the Polokwane smelter matte properties. See figure 15 and 16 in the appendix. Hadley *et al.* 2006

Figure 9 show that there is no significant relationship between the tap rate (ton/min) and matte temperature. The matte viscosity does decrease with temperature which makes the matte more fluid and the speed of the matte therefore does increase with temperature but as the density also decreases with temperature, the pressure at the inlet decreases as well and the mass flow rate in ton/min therefore remain constant. The hole diameter does have an

significant impact on the matte flow rate however. However there is no relationship between slag temperature and tapping rates as per Figure 10.

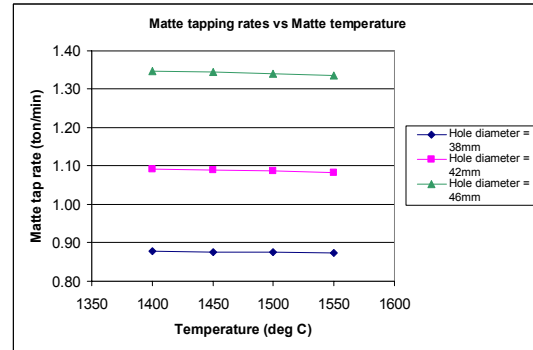


Figure 9: Matte tapping rate vs Matte temperature. Matte level - 60cm, Slag level - 110cm, slag temperature - 1650°C

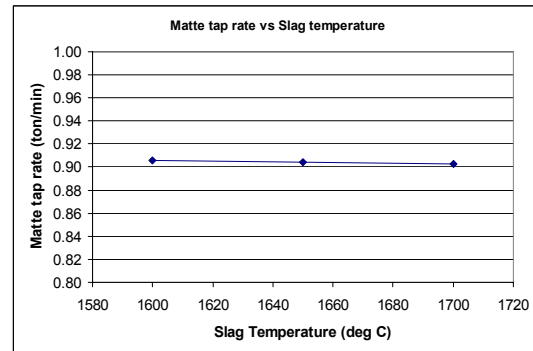


Figure 10: Matte tapping rate vs Slag temperature. Matte level - 65cm, Slag level - 110cm, Matte temperature - 1450°C

The effect of the matte and slag levels can be seen in Figure 11 and 12. Because of the increase in pressure, the matte tapping rate increases with increasing bath levels.

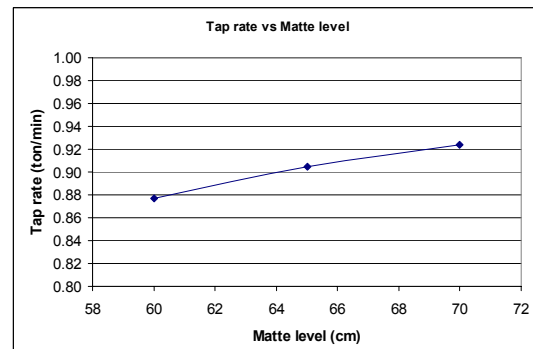


Figure 11: Matte tapping rate vs matte levels. Slag level -110cm, Matte temperature - 1450°C, Slag temperature - 1650°C.

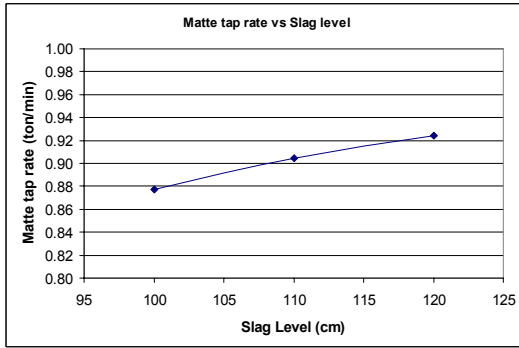


Figure 12: Matte tapping rate vs Slag level. Matte level -65cm, Matte temperature - 1450°C, Slag temperature - 1650°C.

To verify these numbers, data from the plant was taken to see if a correlation between matte temperature and tap rate exists. The data are for a constant bath level reading between 180 and 182 cm. The data are for the same tap hole and the bath level reading are from the sounding bar closest to the tap hole. However, the data does not take the tap hole diameter into consideration which as we have seen from Figure 9 is a major contributor. No correlation could be found.

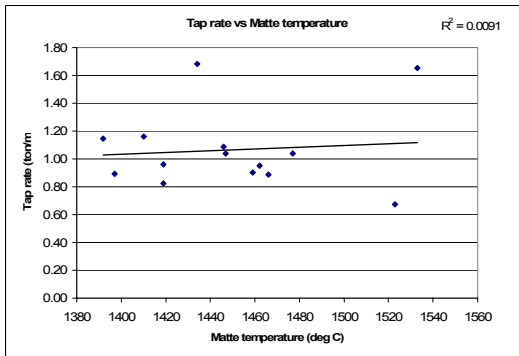


Figure 13: Tap rate vs matte temperature determined from plant data. Bath levels are constant between 180cm and 182 cm. No significant correlation exists.

CONCLUSION

High matte temperatures in the region of 1500°C are often experienced at Polokwane Smelter (improvements have been made). This causes severe corrosion/erosion on the matte tap bricks in the tapping channel. In order to optimize the life of the bricks several tests were done to determine the brick which will be able to withstand these conditions. It was found that the alumina chrome with zirconium brick is giving the best results and the longest life. The tap block was extended and a bull nose was added to the front of the tap block which caused the erosion of the tapping bricks closer to furnace to be less and the time between brick replacements were increased. The CFD model shows the thermal profiles in the copper and refractories as well as the heat fluxes at the different sections of the tap channel due to the matte flow. It shows that virtually no cooling of the

matte takes place in the in the tap channel and it can therefore be concluded that the matte significantly influences the tap block by significantly increasing the temperature of the various parts, but that the tap block has no effect on the matte flow.

ACKNOWLEDGEMENTS

I would like to thank Danie de Kok and Thomas Kinsley, Qfinsoft South Africa, distributors of Fluent, for their support and help in setting up of the CFD model as well as Hatch and Anglo Platinum for allowing this publication.

REFERENCES

- ANDERSON, J.D, (1995), "Computational Fluid Dynamics, The basics with applications", *McGraw-Hill, Inc.*
- ANDREWS, L., (Aug 2005), "Graphite launder bricks from Polokwane Smelter", *Anglo Platinum Research Centre Germiston South Africa, Anglo Platinum Internal report.*
- FLUENT 6.2, "User's Guide January 2005"
- HADLEY, T.D. KRITZINGER, H.P, McDOUGALL, I. PRINSLOO, and VAN VUUREN, D.S., (2006) "Assessment of Polokwane Furnace cooler failure", *CSIR South Africa, 06 April 2006*
- HUNDERMARK, R. DE VILLIERS, L.P.S. NDLOVU, J. "Process Description and short history of Polokwane Smelter", *South African Pyrometallurgy 2006, Johannesburg, 5-8 March 2006, pp.35-41*
- NELSON, L.R. STOBER, F. NDLOVU, J. DE VILLIERS, L.P.S. WANBLAD, D., "Role of technical innovation on production delivery at Polokwane Smelter", *Nickel and Cobalt 2005: Challenges in Extraction and Production, 44th Annual Conference of Metallurgists, Calgary, Alberta, Canada, 21-24 Aug 2005, pp.91-116*

APPENDIX

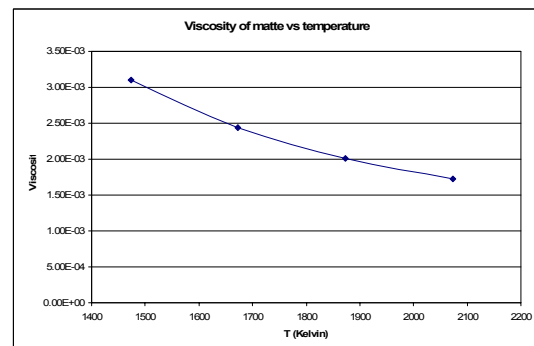


Figure 14: Viscosity vs temperature for matte. (Hadley et al. 2006)

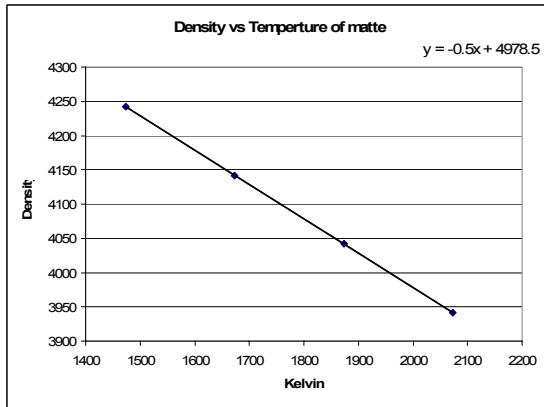


Figure 15: Density vs temperature for matte (Hadley et al. 2006)

Table 3: Refractory properties

	Density (kg/m ³)	Cp (J/kgK)	Thermal Conductivity (W/mK)
Tapping bricks	2900	1090	4
Surround bricks	2900	1090	2.8